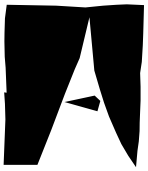

Universitat Autònoma de Barcelona

Geometric Differential Operators for Shape Modelling

A dissertation submitted by **Debora Gil Resina** at Universitat Autònoma de Barcelona to fulfil the degree of **Doctor en Matemàticas**.

Bellaterra, April 22, 2004

Director: **Dr. Petia Radeva Ivanova**
Universitat Autònoma de Barcelona
Dept. Informàtica & Computer Vision Center
Co-director: **Dr. Jordi Saludes**
Universitat Politècnica de Catalunya
Dept. Matemàtica Aplicada 2 (ETSEIT)

Centre de Visió per Computador

This document was typeset by the author using LaTeX 2_ε.

The research described in this book was carried out at the Computer Vision Center, Universitat Autònoma de Barcelona.

ISBN 84-933652-0-3

Printed by Ediciones Gráficas Rey, S.L.

Medical imaging feeds research in many computer vision and image processing fields: image filtering, segmentation, shape recovery, registration, retrieval and pattern matching. Because of their low contrast changes and large variety of artifacts and noise, medical imaging processing techniques relying on an analysis of the geometry of image level sets rather than on intensity values result in more robust treatment. From the starting point of treatment of intravascular images, this PhD thesis addresses the design of differential image operators based on geometric principles for a robust shape modelling and restoration. Among all fields applying shape recovery, we approach filtering and segmentation of image objects.
For a successful use in real images, the segmentation process should go through three stages: noise removing, shape modelling and shape recovery. This PhD addresses all three topics, but for the sake of algorithms as automated as possible, techniques for image processing will be designed to satisfy three main principles: a) convergence of the iterative schemes to non-trivial states avoiding image degeneration to a constant image and representing smooth models of the originals; b) smooth asymptotic behavior ensuring stabilization of the iterative process; c) fixed parameter values ensuring equal (domain free) performance of the algorithms whatever initial images/shapes. Our geometric approach to the generic equations that model the different processes approached enables defining techniques satisfying all the former requirements. First, we introduce a new curvature-based geometric flow for image filtering achieving a good compromise between noise removing and resemblance to original images. Second, we describe a new family of diffusion operators that restrict their scope to image level curves and serve to restore smooth closed models from unconnected sets of points. Finally, we design a regularization of snake (distance) maps that ensures its smooth convergence towards any closed shape. Experiments show that performance of the techniques proposed overpasses that of state-of-the-art algorithms.

Contents

List of Figures

Introduction

The Goal of this Work

A main topic in image processing is the obtention of smooth accurate representations of image objects. There are two main steps related to the former image segmentation problem, extraction of points lying on the objects of interest and computation of a smooth model of such (possibly unconnected) set of points. This PhD focus on the following three points involved in a robust shape modelling:

1. **Image Smoothing.**

   Image feature extraction algorithms [6], [28] mainly use the mechanisms of human perception that base on the detection of abrupt changes. Therefore some sort of image filtering is a compulsory step to remove noise and artifacts that hinder performance of the extractors in real images.

2. **Contour Closing.**

   After image filtering the set of points conforming to the characteristics (edges, ridges) defining image objects are prone to be uncompleted. Line continuation is a possible approach [50], [55] in order to restore a closed model of the shape.

3. **Shape Recovery and Distance Maps.**

   The final step in object segmentation is shape recovery, that is, the computation of a representation of the shape boundary as compact as possible. Because B-spline snakes are the ideal tools for such shape encoding, the definition of a map ensuring their convergence is crucial.

The Approach

The novelty of our work is that the operators performing any of the above tasks are designed to achieve an applicability to real automated procedures as efficient and reliable as possible. To such purpose, we consider that the algorithms should satisfy the following principles:

1. **Meaningful Convergence**

   The above tasks imply the evolution of an initial function in time (either the image to be filtered or the snake modelling objects), which is computed using

an iterative scheme. The first requirement is that any operator converges to an image/shape yielding smooth accurate representations of the original images and objects.

2. **Smooth Asymptotic Behavior**

   In real applications stabilization of the numeric scheme by means of the characteristics of the evolving function should be as important as its theoretic convergence. As if stopping of the iterative algorithm was dependent on the number of iterations, its applicability to real automated procedures would be very limited. A smooth asymptotic behavior ensures such process stabilization.

3. **Robust Parameter Setting**

   The ideal automated-oriented algorithm should be parameter free. Because this is an utopian situation difficult to achieve, we will use the following relaxation. We require that the parameter values making the technique fulfill the first two points is invariant whatever the nature and degree of noise and the geometry of shapes.

The Tools

The mathematical tools to handle deformation/evolution processes lie in the framework of Partial Differential Equations (PDE's for short). Although any phenomena formulated in PDE terms is of analytic nature, the geometry of the underlying space where it takes place completely determines and characterizes it. In this work, we will see that an analysis of the PDE's related to image processing techniques from a geometric point of view, provides with the necessary tools to design operators satisfying the former requirements.

State-of-the-Art Overview

Image Filtering and Shape Restoration

Noise removal for an improving of image quality is an issue that has been addressed since the early years of image processing. The most common approach [1], [64] consists in filtering the initial image by means of a parabolic (time dependant) PDE. From this point of view, current image filtering operators can be split into two distinct families: the ones arising from heat diffusion processes and the ones based on geometric flows.

The first group filters an image by means of a PDE that describes the physical process of heat diffusion and admit a divergence-like formulation. Linear filtering by convolution with a Gaussian kernel is the classic low-pass image smoothing. Although, it enjoys from an efficient image regularization, it must, by its own design, tackle with blurring of the image descriptive features such as edges or ridges. This need of a selective image filtering has been frequently addressed in the last few years and leads to designing equations able to remove noise and preserve, as much as possible, image contrast changes.

A usual way of achieving this compromise in the filtering technique consists in including a term preventing diffusion across edges. Treating edges as insulators was first introduced in the Perona-Malik model [60] that adds an edge enhancing factor inside the image gradient divergence that describes the classic heat diffusion. In an ideal continuous setting, such factor would evolve images towards a piece-wise constant representation of regions of uniform gray-level separated by the original image edges. In practice, the scheme depends upon the choice of a threshold value determining what magnitude of the image gradient is to be considered an edge and constitutes a main problem when dealing with highly noisy images [53], [74], [81]. Since noise affects image contrast changes, it punches the theoretic closed edges, letting the heat out. This phenomena, known as the Pinhole Effect [53], blurs edge and yields constant final images. The other drawback comes from the backwards edge-enhancement diffusion of the model that might amplify noise and produces false step edges (the Stair-Casing Effects, [80], [81]). Anisotropic diffusion [72] provides with an efficient robust-to-noise model by using a regularized version of the gradient in the Perona-Malik equation, so that the heat diffusion is described by means of a diffusion tensor with the eigenvector of minimum eigenvalue oriented along the direction of the image features to be preserved. The well-posedness of the former formulation has been exploited hereinafter by other authors [8], [9].

Another approach to image feature preservation relies on adding a reaction term to the diffusion equation, the close-to-data constrain [62], forcing similarity to original images [43], [2], [7]. The trade-off between smoothing and similarity is controlled with an extra parameter that needs to be determined for every image as it strongly depends on the amount of noise.

Geometric flows base on shape/curve regularization ruled by deformations that depend exclusively on the geometry of the evolving curve. By their independence from the curve parameter, they admit an implicit formulation, which serves to apply them to image filtering through a level sets [57], [48] approach. As the latter smoothing bases on the image level curves geometry rather than on its intensity values, it does not produce any edge blurring [1], [64] as it alters edges shapes but not the contrast change defining them.

Current geometric flows derive from the mean curvature flow ([32], [33], [34] or [40]), which is considered the geometric equivalent to the heat equation [1] as in the curve arc length parameter the curvature corresponds to the curve second derivative. Curves evolving under their mean curvature reduce their number of oscillations, so that the flow enjoys from the same regularizing properties than heat diffusion. Unfortunately, as in the case of heat-based filtering, smoothing is indiscriminate and shapes converge to circles [32] [33] before collapsing to a point. Up to our knowledge there are two different solutions to prevent curve collapsing [49], [79].

The min-Max flow of [49] exploits that evolution under negative curvature stops as soon as the curve becomes convex. Assuming that the curve is embedded in the plane as a level set of a given image, the average gray level in a window centered at each point serves as a switch between positive and negative curvature. The target curve evolves until this average equals its own gray level, which it is satisfied for polygonal shapes of a side length depending on the window size. It follows that the stencil size used to compute averages must reach a compromise between resemblance to the original

curve and shape simplification (noise removing). The stochastic based geometric flow introduced in [79] suggests adding a stopping factor to the mean curvature equation. Such term penalizes given orientations of the curve unit tangent, so that the initial shape converges to a pre-given polygon.

A common drawback of most of current image filtering techniques is that their steady-state is trivial, that is a constant image for diffusion processes [72] and either a point or a straight line for curvature based ones [32], [33], [40]. This property, although desirable for a scale-space analysis of images/shapes [1], [41], is a main nuisance when using these techniques for segmenting purposes, as they require a stopping time to recover shapes of interest. The simplest way to avoid this feature-damaging effect is to rely on a given (image-dependant) number of iterations to stop the evolution ([60], [72], [32]). Another solution ([46], [9], [2], [43]) is to add a new term, the close-to-data constraint [62], that controls resemblance to the original data. A third option consists in including some previous knowledge about the geometry of the shape to be smoothed [79].

We conclude that current filtering techniques converge to trivial images (which, usually, achieve the minimum of a particular energy) unless we either admit an irregular image close to the original one ([2], [7], [43], [49]), rely on an image-dependant number of iterations ([60], [72], [32]), or prefer a (previously given) model of shapes [79]. In any case, some sort of user intervention is essential in order to stabilize the iterative process at images useful for a latter recognition or segmenting task.

Our Contribution

The first method we propose is a curvature based shape evolution with a factor preventing the flow from converging to a trivial curve. Selective smoothing by means of a stopping factor is not original, as other techniques such as the edge enhancement of [60] or the geometric flow of [79] also exploit this idea. The novelty of our work lies on the fact that the stopping factor relies on a roughness function, that measures the local irregularity of a curve in terms of the smoothness of its tangent direction along the curve, instead of basing on a threshold value [60] or a pre-given model of the shape [79]. Such roughness measure does not penalize the curve curvature magnitude but high variation and cancels on infinitely smooth curves. As a consequence, by adding it to the mean curvature flow, we obtain a regularized curvature flow (RCF) that converges to smooth curves preserving significant enough features as to identify the original noisy shape. The associated image filtering admits integration with a finite difference Euler scheme presenting a smooth enough asymptotic behavior as to stabilize by means of standard numeric criteria.

Another contribution is to handle the study of geometric flows by means of the curve unit tangent angle and curvature in the arc-length parameterization of the curve, which brings our work closer to [32], [33], [34] than to the viscosity solutions implicit parameterization approach of [15], [20], [57]. The new formulations developed turn into an ideal tool to detect the source of pathologies in curve evolution and distance maps.

Shape Restoration

Smooth line connection arises in so different image processing areas as segmentation, image in-painting, splines interpolation or object disocclusion. Most techniques [4], [12], [50] base on variational principles that lead to a diffusion-like equation that serves to smoothly evolve an image/curve until the completion is achieved.

Object disocclusion and image in-painting focus on filling in gaps in an image in such a way that level lines arriving at gaps boundaries are smoothly prolonged inside. Following the Gestalt principle of good continuation, recent techniques ([4], [13], [50], [55]) base on the way humans join unconnected curves to reconstruct the underlying shape. According to psychophysicist studies [37], the curves that reconstruct objects should minimize an energy functional involving length and curvature (Euler's elastica [54]). In the case of (the one dimensional) line continuation for object disocclusion ([55], [50]), curve gaps are interpolated (joint) by line segments minimizing the functional, for image in-painting ([4],[13]) one seeks for the function, which corresponds to the reconstructed image, that achieves a simultaneous minimum for all its level sets. The fact that the curvature term is of second order, introduces a non-linear fourth order term in the associated variational problem that troubles the numeric implementation. Although there are some numeric approaches to a weak formulation of the curvature term [14], the most common solution is either implementing a simplified version of the functional or introducing of an extra function to be minimized. Dropping the curvature term in the elastica functional ([50], [13]) in disocclusion algorithms results in a linear interpolation of curve gaps. This geodesic approach is easy to handle, but the reconstructed contours are prone to present corners at joint points, thus, violating the Gestalt principle. The image restoration of [4] bases on the computation of a vector field that smoothly extents the image unit gradient at gaps boundary to the whole gap to be filled-in. The restored image is the function of minimum variation which level sets are given by the vector extension. In analytic terms, the functional uses the angle of the vector to compute the curvature term in the Euler elastica, so that, a system of second order PDE's replaces the forth order original equation.

A completely different approach to contour closing comes from mathematical morphology [1] [64], which basing on set operators achieves contour completion by a dilation at a suitable scale. Although the complexity of the computational algorithm is minimum compared to the iterative schemes of variational techniques, morphological closings might not achieve so high quality in restorations. First, as there is not any explicit control on curve smoothness, restorations do not need to satisfy the Gestalt principle. Second, the fact that the associated structural elements (typically, lineal or circular) are constant is a main drawback, since it may imply that the closed shapes differ significantly from the incomplete contours.

Our Contribution

Our second contribution consists in embedding contour closing into the framework of functional extension described by means of a diffusion tensor that prevents (degenerates) any diffusion in the normal space to the uncomplete contours. This natural requirement for operators designed to extend image level sets implies loosing the strong

ellipticity of the differential operator that ensures [22], [23] existence of a unique solution. We propose approaching diffusion processes from the point of Riemmanian geometry by means of the diffusion tensor that describes the mechanism. In this context, degeneracy implies restricting diffusion to the manifolds generated by the vector fields of positive eigenvalues, provided that they exist. A classic result (Frobenius theorem [67]) on differential geometry yields sufficient conditions on the vector fields for the unique existence of solutions to a restricted anisotropic extension/diffusion process.

The restricted diffusion applied to extending the characteristic function of the open curve results in our Anisotropic Contour Completion (ACC for short). The fact that a smooth vector field automatically satisfies the Frobenius conditions reduces contour completion to the definition of a vector field representing the tangent space of the contours to be closed. Instead of using a, computational expensive, iterative extension ([75], [4]) of vector fields we suggest using the Structure Tensor [36]. This matrix, commonly used for analyzing the direction of maximum contrast change [74] and texture orientation [5], [36], yields smooth extensions/regularizations of the image gradient direction. It follows that applied to images having the uncomplete contour as level set, the Structure Tensor produces smooth vector field representing a reliable model of the open curve. This strategy gives rise to Linear Vector Fields, if a mask of the open contour is used, and Distance Vector Fields in the case of using its distance map.

Shape Recovery

The preferred tool to detect and smoothly model image objects are active contours or snakes ([11], [12], [38], [47], [58]). Snakes are evolving curves that deform under the gradient descent of an energy that characterizes a smooth approach of the target contour as a minimal curve. Resemblance to the curve is guaranteed by means of an external potential, while internal constraints involving the norm of the snake first derivatives control its continuity and smoothness and determine the snake at parts where no information is available.

There are two different frameworks in current snakes formulations: the parametric [38] and the geometric [11], [12], depending on the way the energy is formulated. In classic snakes [38], the external energy splits from an internal constrains given in terms of minimum variation of the snake first and second derivatives. Minimization of the first derivative variation makes the snake linearly interpolate contours, meanwhile the second derivative term forces it to smoothly approach them. The former internal constrains are not intrinsic to the geometry of the curve and their values depend upon an explicit parameterization of the curve, which limits parametric snakes to segmentation of a single object. Geodesic snakes [11], [12], fuse both energies into a geometrically intrinsic potential that seeks for the curve of minimal length in a Riemmanian manifold with the external energy as metric. Since their formulation does not depend on the snake parameter, they admit a level set approach [48] able to detect more than one object. However as they only take into account the snake first derivatives (length) they are limited to contour linear interpolation.

In any case, poor convergence to concave shapes is a main limitation of snakes as a

standard segmentation and shape modelling technique. The external energy is crucial in order to ensure the snake convergence because it is the only force that pushes the snake into concave regions, as its internal energy increases when new inflexion points are created. The usual external potentials used in snake formulations are (Euclidean) distance and gradient maps for the parametric case and just gradient maps for the geodesic one. Curves of level zero correspond to the contour of interest and the snake moves in the direction opposite to the gradient of the distance/gradient map. Unfortunately, the geometry of the curve of level zero may produce maps with null gradients along some curves. Because the snake gets caught in these local minima and produces a wrong model of the shape, several ways of addressing this problem have been developed in the last years. The first naif solution is initializing the snake close to the final shape so that we make sure that it is far away from these local minima, which is certainly not a very elegant approach for automated procedures. Some authors [17], [68] suggest searching for the global minimum of the energy, but global minimums of real images are hard to find in an efficient way without manual intervention.

The most efficient solutions are given by the gradient vector flow technique [75], in the case of a parametric formulation, or [16] area minimizing balloon forces, in the case of a geodesic approach. Gradient vector flow techniques ([75], [77], [59]) use a vector value heat equation to compute a regularized version of the gradient of the external energy. By means of a reaction term weighted by the external potential gradient they yield a smooth approximation that only admits isolated zeros. The technique succeeds in producing smooth gradients in the whole image that guide the snake to the final contour for a large variety of geometries. However the vector field obtained with GVF may have saddle points which also trap the snake. Balloon-like forces [16] are added to the geodesic formulation in the form of a constant shrinking force that pushes the snake into concavities and helps the snake adapting to any geometry. However, in order to ensure that the scheme will stop at the boundary of interest, an equilibrium between the constant shrinking velocity and the static vector field given by the image object must be achieved. It follows that, should this condition be satisfied, incorporating the curvature term into the convergence scheme constitutes a significant drawback. For the balloon force must overpass the magnitude of the curvature to enter into concave regions but, at the same time, it must be kept under the minimum of magnitude of the external force gradient to guarantee non trivial steady states. This dichotomy, makes geodesic snake convergence to depend on parameters which values are case sensitive.

Our Contribution

Our last contribution concerns the development of a new external energy based on the geometry of the curve to be modelled that ensures a robust snake convergence whatever the concavity of the curve is. The first important novelty of our contribution is a geometric characterization of convex functionals in terms of smoothness of their level sets. Convexity of the external energy guarantees [23] the existence of a unique minimum that can be reached following the functional gradient descent. Unfortunately, the analytic formulation of convexity in terms of the functional second

derivatives is not robust to noise and irregularities and leads to ambiguities in real images. Our geometric criterion is a simple and robust way of detecting what makes current external energies fail to attract the snake. The usual external potentials used in parametric snake formulations may be regarded as a propagation of either the target curve (Euclidean) or a function defined on it (GVF). In any case their main source of error is due to shock formation during the evolution process that introduces singular level curves and inflexion points. Our second proposal is to use a smooth curve deformation to propagate the initial shape. By tracking back the deformation of a curve that evolves by minimum curvature flow, we construct a distance map that encapsulates the natural way of adapting to non convex shapes. The gradient of this map, which we call curvature vector flow (CVF), is a smooth external force that guides the snake towards any contour, whatever its geometry.

Chapter 1

Partial Differential Equations in Image Processing

All techniques discussed in this work handle evolution and transformation of images and curves. Because images and curves are represented by functions defined on a given domain, Ω of $\mathbb{R}$ or $\mathbb{R}^2$ with values in either $\mathbb{R}^2$ (curves) or $\mathbb{R}$ (images), in this first chapter we briefly introduce the general equation that describes evolution of a given initial function in time. We will discuss the different processes that such equation models as well as the special cases that arise in image processing techniques. We will give intuitive interpretations of each of the formulations, a suitable classification according to the issues we will address and examples of techniques fitting into the latter categories. An overview on general theory on PDE's may be found in [22], [23] or [71].

The general model for the evolution of an initial function $u_0(x)$, $x \in \mathbb{R}^n$, in time is formulated with a PDE of parabolic type:

$$u_t(x,t) = Lu \quad \text{with} \quad u(x,0) = u_0(x) \tag{1.1}$$

The nature of the particular process that is modelled is determined by the values that the function u takes on the boundary, $\partial\Omega$, of the domain Ω holding the evolution process. The right-hand side of the equation, L, denotes a partial differential operator and it represents/describes the mechanisms that rule the transformation of the function. Let us classify the different phenomena governed by (1.1) and describe the mechanism itself.

Let u_{x_I} be the partial derivative with respect to the coordinates specified by the index set $I = (i_1, \ldots, i_k)$ and define the order of the derivative to be the cardinal of the index set $|I| = k$. An operator of order N is given by:

$$Lu = \sum_{k=0}^{k=N} \sum_{|I|=k} a_I u_I$$

where the coefficients a_I are smooth functions depending on x and, eventually, on the function u and its derivatives. In this general setting, PDE's can be classified

according to either the nature of the differential operator or the domain of definition of the function:

OPERATOR TYPES

1. **Domain Types.** Depending on the dimensions of the spaces the function takes its values we can differentiate two cases:

   (a) **Image Evolutions.** This is the usual case where $u : \mathbb{R}^n \to \mathbb{R}$ represents mass density, heat, a chemical concentration or an image.

   (b) **Curve Deformations.** In the case that the function u is a curve parameterization $\gamma : [0, 1] \to \mathbb{R}^n$, equation (1.1) represents its deformation. Snakes and geometric flows are some of the examples found in image processing.

2. **Operator Types.** The differential operator, L, can be:

   (a) **Linear.** If for any two functions, u_1, u_2, it satisfies additivity:

   $$L(u_1 + u_2) = Lu_1 + Lu_2$$

   This is a desirable property, both, in practical applications (signal processing) and from a theoretic (mathematical) point of view. On one hand, it implies that given the response for two different signals the response for their addition is the sum of responses. On the other one, the operator can be computed by means of convolution with a kernel (a filter in Fourier domain) [22] which is fast computational operation. Finally, from a mathematical point of view, linearity simplifies the study of the solution to (1.1) as there are some general rules to design operators yielding uniquely solvable problems [23].

   It is not difficult to check that the condition is satisfied only if the coefficients in (1.2) depend exclusively on x. Furthermore, one can talk of **homogeneous** operators if they are constant and **inhomogeneous** otherwise. One way of understanding this last case is by thinking that the domain/space where the process takes place is not an Euclidean $\mathbb{R}^n$ but a manifold/surface [21].

   However, most of the techniques used in image processing depend upon operators whose nature is:

   (b) **Non-Linear.** In many cases the mechanisms of the deformation/evolution (1.1) depend on the values of the function u and its derivatives. We may interpret that the deformation process is not always taking place in the same manifold/space but on a space that also changes/transforms in time. Anisotropic diffusions and curvature flows fit into this category.

Any of the above operators describes 2 main phenomena depending on the boundary conditions used in equation (1.1):

PROCESSES MODELLED

1. **Extension Processes.** Dirichlet boundary conditions:
$$u(x,t)|_{\partial\Omega} = f(x)$$
mean that the solution $u(x,t)$ converges to a function (the equilibrium point of (1.1) given by $Lu \equiv 0$) that extends the boundary function f.

   Periodic boundary conditions can also be included, as, in this case, the function u represents a surface/curve and equation (1.1) its deformation. In some sense, we may regard such deformation as a propagation of the original shape in the space $\mathbb{R}^n$.

2. **Diffusion Processes.** Neumman boundary conditions are given in terms of the scalar product of the function gradient, ∇u, and the unit normal, $\overrightarrow{n}$, to the boundary domain:
$$\langle \nabla u(x,t), \overrightarrow{n} \rangle|_{\partial\Omega} = 0$$
   Since the above condition means that the flow of mass/heat across the boundary $\partial\Omega$ is zero, it implies that the values of the original function u_0 are re-distributed (diffused) in Ω.

We will give a more precise description of the former processes in the next Sections, which restrict to PDE's given by second order operators:

$$Lu = \underbrace{\sum a_{ij} u_{x_i x_j}}_{Second\ Order} + \underbrace{\sum b_i u_{x_i}}_{First\ Order} + \underbrace{cu}_{Zero\ Order} \tag{1.2}$$

A second order operator is called **elliptic** if for any vector $\xi = (\xi_1, \ldots, \xi_n)$ the quadratic form given by $\sum a_{ij}\xi_i\xi_j$ is positive-definite. Under this condition it is guaranteed ([23]) that a unique solution to (1.1) exists. Besides, evolution equations governed by such operators enjoy from convenient properties for image processing purposes:

PROPERTIES OF ELLIPTIC OPERATORS

1. **Smoothness.** Solutions to (1.1) are infinitely smooth functions, so that the equation is a good noise removing tool. We remit the reader to Example 1.1.1 for an illustrative case where solutions fail to be smooth.

2. **Maximum Principle.** The extrema values are attained at time zero, which ensures simplification of shapes and images.

In the particular framework of Image Processing, we have split the general PDE (1.1) into heat-like equations and those ones that minimize an energy functional.

1.1 Heat Equations

In this context a heat equation will be any second order PDE (1.2) with its second order term given in divergence form:

$$u_t = \underbrace{\operatorname{div}(J\nabla u)}_{Diffusion} + \underbrace{F_1(u_x, u_y)}_{Transport} + \underbrace{F_0(u)}_{Reaction} \tag{1.3}$$

where J is a symmetric semi positive definite tensor (i.e. for each point, (x, y), $J = J(x, y)$ is a 2×2 matrix), F_1, F_0 are the first and zero order terms and the divergence of a vector $j = (j_1, \ldots, j_n)$ is given by $\operatorname{div}(j) = \partial_{x_1}(j_1) + \cdots + \partial_{x_n}(j_n)$.

In this case we can provide with a more accurate description of the mechanisms that govern the evolution of the initial function, as each of the summands in (1.3) has a specific role:

1. **Diffusion Term**

   The second order term, $\operatorname{div}(J\nabla u)$, is the main descriptor as it determines the way information/mass distributes (diffuses). For a better understanding, let us consider our function u to be a mass distribution and let us represent it as mass particles which density/concentration depends on the values of u, the higher they are the more mass density. Under this model, we have that the vector field $j = J\nabla u$ locally describes the direction towards the initial mass particles move, as the scheme drawn in fig.1.1(a) represents. The amount of mass that a given enclosed area, Ω, looses or gains only depends on how much mass escapes through its boundary. If j was tangent to the area boundary, $\partial\Omega$, the effect of the diffusion would be redistributing the mass particles along it (fig.1.1 (b)). This intuitive reasoning is mathematically formulated by means of the generalized version of integration by parts given by the divergence formula:

   Divergence Formula

   $$\int_\Omega v \operatorname{div}(j) = -\int_\Omega \langle \nabla v, j\rangle + \int_{\partial\Omega} v\langle j, \overrightarrow{n}\rangle \tag{1.4}$$

   for $\overrightarrow{n}$ the outward normal vector to $\partial\Omega$. If we apply the latter equality to $v = 1$ we obtain that, in the absence of other terms, the evolution (1.3) fulfils:

   $$\int_\Omega u_t = \int_\Omega \operatorname{div}(j) = \int_{\partial\Omega} \langle j, \overrightarrow{n}\rangle$$

   It follows that only the normal component of the flow affects the total amount of mass enclosed by the area Ω. The fact that tangent components do not change the shape of the boundary of the area enclosing mass will be especially relevant in the analysis of geometric flows.

   Apart from the above physical interpretation, the diffusion term has a geometric meaning that will be useful at some parts of the foregoing discussion. The mass flow, $\overrightarrow{j}$, is univocally determined by the diffusion tensor, J. The scalar product that it defines corresponds to the metric of the (Riemmanian) surface where the diffusion process takes place. Geometrically, a metric is described by means of an ellipse with principal axes of lengths equal to the eigenvalues of J (λ_1, λ_2) oriented by its corresponding eigenvectors ξ and η. The ellipse associated to this metric locally describes the way mass distributes in the plane: an amount λ_1 of mass travels along ξ and an amount λ_2, in the direction η. In the context of metrics, diffusion processes are classified into **isotropic**, when the eigenvalues of J are equal and **anisotropic**, in the case of different eigenvalues.

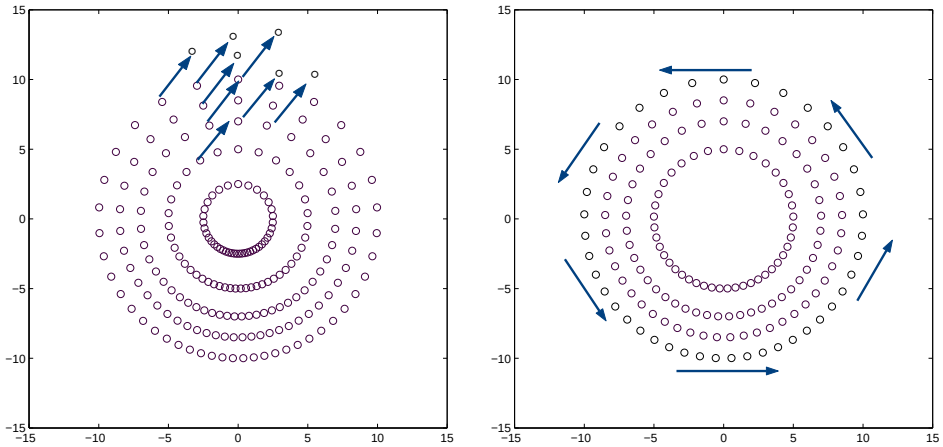

Figure 1.1: Mass diffusion across (a) and along (b) boundary domain

2. **Transport Term**

   The transport first order term:

$$F_1(u_x, u_y) = A(x, y, u)u_x + B(x, y, u)u_y$$

   dues its name to the way solutions to a pure first order PDE:

$$u_t = A(x, y, u)u_x + B(x, y, u)u_y$$

   are computed. The classic way of solving the above equation is by finding the level curves (characteristic curves) of the solution, $u(t, x, y)$, in the space-time domain. Since the values of the initial function $u_0(x, y)$ travel along such curves, the whole process may we interpret as moving/transporting the initial quantities. This way of propagating the initial function may lead to ambiguous (i.e. discontinuous solutions) situations each time two characteristic lines of different levels cross, since at such points the function takes more than one value. This pathology arises in the non-linear case:

   Example 1.1.1 *Example of a discontinuous solution*

   Consider the transport equation given by:

$$u_t = uu_x \quad \text{with} \quad u(x, 0) = x^2$$

   The level curves, $\gamma(s) = (x(s), t(s))$, of the solution satisfy:

$$0 = \frac{d}{ds}(u(\gamma(s))) = u_x x_s + u_t t_s = u_x x_s + u t_s u_x = (x_s + t_s x_0^2)u_x$$

It follows that:

$$\left.\begin{array}{rr} x_s = & -x_0^2 \\ t_s = & 1 \end{array}\right\}$$

and that the solution is constant and equal to x_0^2 along the straight lines $x = -x_0^2 t + x_0$. Since non-parallel lines always cross, the potential solution, $u(x,t)$, is discontinuous for all times. This does not contradict the properties given at the beginning of the chapter as the equation lacks of the second order term. The effect of adding such a diffusion term is that the solution is not constant along characteristic lines, but follows a differential equation. In other words the level curves are not straight lines as diffusion bends them. The drawing in fig.1.2 (b) represents the jump discontinuity of the solution to the transport equation at a point where two characteristic curves (red lines in the x-t plane) meet. The regularizing effect of a diffusion term is illustrated in the surface mesh of fig.1.2 (a) representing the solution to $u_t = uu_x + u_{xx}$. Note that its level curves (lines on the surface and on the x-t plane) are not straight lines.

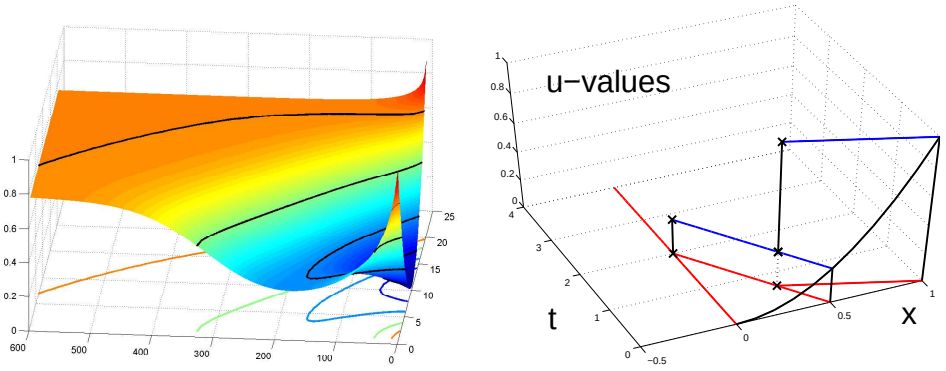

(a) (b)

Figure 1.2: Regularizing effect of diffusion (a) in a transport equation (b)

3. **Reaction Term**

   One of its usual roles is to include Dirichlet boundary conditions into the model, instead of imposing them at each step of the evolution. The name Reaction Term comes from the early days of diffusion theory, when as such processes were approach from a point of view of Newton mechanics, Dirichlet conditions were interpreted in terms of a reaction (response/force) of the boundary domain to diffusion.

1.1.1 Image Diffusions

Diffusion is the natural physical way of distributing information. The dynamic process of the evolution of an initial heat distribution, u_0, in time is governed by a heat

equation in pure divergence form:

$$u_t(x,y,t) = \operatorname{div}(J\nabla u) \quad \text{with} \quad u(x,y,0) = u_0(x,y) \tag{1.5}$$

with Neumman conditions in the boundary domain. The solution represents the heat or mass distribution in the plane at each time t. Concerning the final heat distribution, steady states of (1.5) can be described by means of their level sets. If we denote by Ω the region enclosed by a level curve γ then, the Divergence formula yields that final states must satisfy the following integral equation:

$$0 = \int_\Omega u_t = \int_\Omega \operatorname{div}(J\nabla u) = \int_\gamma \frac{\nabla u^t J \nabla u}{|\nabla u|} \tag{1.6}$$

Therefore the final heat distribution will be constant unless the metric given by J degenerates (i.e. cancels) on some closed curves. In this case, the final heat distribution will consist of closed regions of uniformly distributed heat separated by these curves. In thermodynamic terms we may think that these curves behave like insulators.

This property is commonly used in image processing. The original image is set to be the initial heat distribution and the metric is chosen in such a way that it degenerates on points that satisfy some conditions. In this manner the final state that we achieve is an image so that features of interest in the original image are easier to identify. Some filtering techniques conforming to equation (1.5) are the following:

Example 1.1.2 *Gaussian Filtering*

The heat equation in Euclidean space:

$$u_t = \operatorname{div}(\nabla u) = u_{xx} + u_{yy} = \Delta u$$

is the classic low-pass filter image smoothing. It is the only technique with an explicit solution given by convolution of the initial function with a Gaussian kernel G_t:

$$u(x,y,t) = G_t * u_0 = \frac{1}{2\pi t} \int e^{-(\tilde{x}^2+\tilde{y}^2)/(2t)} u_0(\tilde{x}-x, \tilde{y}-y) d\tilde{x} d\tilde{y}$$

Its indiscriminate smoothing (blurring) of edges constitutes one of its main drawbacks.

Example 1.1.3 *Edge Enhancement Diffusion of Perona-Malik*

This method, introduced by Perona and Malik [60], was designed to avoid edge blurring and profit the smoothing effects of the Gaussian filtering at image areas where contrast changes are not significant enough. It is defined as:

$$u_t = \operatorname{div}(g(|\nabla u|)\nabla u) \tag{1.7}$$

with the edge enhancing function defined as $g(s) = \frac{\lambda^2}{\lambda^2+s^2}$, for a constant λ.

In physical terms, one can interpret the function g as a stopping diffusion factor that prevents diffusion across edges, as by (1.6), steady states are characterized by:

$$\int_{\{u\geq\alpha\}} u_t = \int_{\{u\equiv\alpha\}} g(|\nabla u|)|\nabla u| ds = \int_{\{u\equiv\alpha\}} \frac{\lambda^2 |\nabla u|}{\lambda^2 + |\nabla u|^2} ds$$

It follows that there is not any diffusion across those curves where $|\nabla u| \to \infty$, that is, at ideal edges. For a different interpretation in image processing, let us develop the divergence term and write equation (1.7) in the form:

$$u_t = g u_{\xi\xi} + (g + g'|\nabla u|) u_{\eta\eta}$$

where $u_{\xi\xi}$ and $u_{\eta\eta}$ denote, respectively, the second derivatives in the tangent , ($\xi = \frac{\nabla u^{\perp}}{|\nabla u|}$), and normal, ($\eta = \frac{\nabla u}{|\nabla u|}$), directions. At those points, where $g + g'|\nabla u| < 0$ not only edges are preserved but even enhanced. This gives an interpretation to the parameter λ as a threshold value for $|\nabla u|$ since for $|\nabla u| < \lambda$, the edge is blurred and enhanced, otherwise.

However, the above properties constitute the main drawbacks of the technique. On one hand, as edges in real images are prone to be incomplete, some diffusion occurs at these places, producing the so known Pinhole Effect [53]. On the other one, backwards diffusion at significant edges makes the method potentially ill-posed [74],[81], [56] and prone to yield step images (Staircasing Effects, [80], [81]).

Example 1.1.4 *Anisotropic Diffusion of Weickert*

One solution to the problem consists in using a regularized version of the gradient in the formulation of the Perona-Malik method:

$$u_t = \operatorname{div}\left(J(St_\rho(\nabla u_\sigma))\nabla u\right) \tag{1.8}$$

where the diffusion tensor $J(St_\rho(\nabla u_\sigma))$ has the same eigenvectors as the Structure Tensor [36], St_ρ, with eigenvalues depending on the structures to be enhanced. In [72], [74] two different models are proposed to enhance edges and linear structures. Let λ_1, λ_2 denote the biggest and the smallest eigenvalues of J_ρ and v_1, v_2 the corresponding eigenvectors, then the formulations are:

1. **Edge Enhancement**

   For edge enhancing the eigenvalues of the diffusion tensor are set to:

   $$\mu_1 := g(\lambda_1), \quad \mu_2 := 1$$

   with stopping diffusion function, g, defined as follows:

   $$g(s) := \begin{cases} 1 & (s \le 0) \\ 1 - \exp\frac{-C}{(s/\lambda)^4} & (s \ge 0) \end{cases}$$

   where C and λ are constants. Like the case of the Perona Malik model, the magnitude of λ determines which edges are to be smoothed. Weickert determines [72] the optimal values for C and λ to be: $C = 3.31488$ and $\lambda = 3$. The Structure Tensor is over a regularized version of the gradient $\nabla u_\sigma := G_\sigma * \nabla u$, with $\sigma = 3$ and integration scale $\rho = 0$.

2. **Line Enhancement**

   The variant for enhancement of linear structures profits that the eigenvector v_1 is oriented in the direction of maximum contrast change and that the difference

of the eigenvalues $(\lambda_1 - \lambda_2)^2$ (coherence) measures the reliability of the potential edge, being minimum in the isotropic case. Taking into account all these facts a diffusion tensor with eigenvalues:

$$\mu_1 := \alpha, \;\; \mu_2 := \alpha + (1-\alpha) * \exp \frac{-C}{(\lambda_1 - \lambda_2)^2};$$

will preferably diffuse along linear structures, so that their gray level uniformizes.

General arguments on non-linear parabolic PDE's [7], [72] yield that, as the diffusivity tensor is positive defined, the initial boundary problem has a unique smooth solution which continuously depends, in L^2, on the initial data [74]. Besides, the existence of Lyapunov functionals provided a description of the asymptotic behavior as a constant function equal to the integral of the initial image. This is, indeed, the main drawback of the method, since it implies the need of a stopping time if one is to use it either to segment images or for shape recognition.

Still the generic good properties of the model (1.8) have inspired other methods [8], [9] aimed at enhancing other image structures:

Example 1.1.5 *Adaptive Smoothing*

In [9], the authors propose a variant formulation of divergence-like equations better suited for selective smoothing of image structures. If $\eta = \frac{\nabla u}{|\nabla u|}$ denotes the unit gradient and $\xi = \frac{\nabla u^{\perp}}{|\nabla u|}$ the tangent to the image level curves, then the general evolution equation:

$$u_t = c(|\nabla u|)(a u_{\eta\eta} + b u_{\xi\xi}) \quad \text{with} \quad a, b \in [0,1] \tag{1.9}$$

comprises the Perona-Malik and the anisotropic models and allows smoothing along other preferred directions different from edges. In particular, they suggest using directional derivatives in the principal directions of the function Hessian:

$$\begin{pmatrix} u_{xx} & u_{xy} \\ u_{xy} & u_{yy} \end{pmatrix}$$

in order to enhance ridges and valleys.

1.1.2 Information Extension

Heat diffusion has another mathematical and physical use hardly exploited in image analysis. Heat diffusion (second order elliptic operators, in general) has the property of smoothly extending a function defined on a curve in the plane. If L denotes an elliptic operator, then the function that solves the PDE:

$$Lu = 0 \quad \text{with} \quad u_{|\gamma} = f \tag{1.10}$$

is the unique smooth extension [23] of the function f which was defined only on the curve γ. The equation is solved by seeking the steady states of the associated parabolic PDE:

$$\begin{aligned} u_t &= Lu \\ u_{|\gamma} &= f \end{aligned} \tag{1.11}$$

From the point of view of thermodynamics, we may think that the heat distribution on γ given by f never puts out. Boundary conditions can either be imposed at each iteration or added to the model as a reaction term by means of the characteristic function, χ_γ:

$$u_t = Lu + \chi_\gamma(u - f)$$

where:

$$\chi_{|\gamma} = \begin{cases} 1 & \text{if } x \in \gamma \\ 0 & \text{otherwise} \end{cases}$$

We will restrict to elliptic operators admitting a divergence form given in equation (1.5). The ellipse describing the metric given by J corresponds to the structural element of the associated dilation, so that isotropy leads to circular structural element and anisotropy to elliptic ones. In the case of classic mathematical morphology, the extension is based on the Laplacian operator and the function to be extended is the characteristic function of a set of points. The scale or radius of the dilation corresponds to time in equation (1.11). Some of the image processing fields and techniques handling functional extension are:

Example 1.1.6 *Image In-Painting and Contour Completion*

Image gap filling and curve completion can be viewed as particular cases of a functional extension process. In the case of multiple level sets completion (image gap filling shown in fig.1.3 (a),(c)), γ corresponds to the gap boundary and f to the image to be restored. For contour completion (fig.1.3(b)), γ is the unconnected curve to be closed and f its characteristic function. As example we have the image in-painting developed in [4] that uses high order extension to compute a vector field interpolating the image gradient at gap boundaries. In Chapter 4 we will also address contour closing and gap filling.

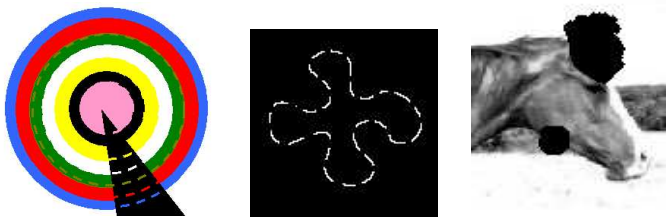

(a) (b) (c)

Figure 1.3: Examples of Extension Processes: level lines continuation or gap filling (a), single contour completion (b) and image in-painting (c)

Example 1.1.7 *Gradient Vector Flow*

These techniques [75], [77] serve to smoothly extend a vector field, (f_x, f_y), defined on a curve of interest. The vector extensions, (u, v) are the steady-points of the

following diffusion-reaction equations:

$$u_t = \Delta u - (f_x^2 + f_y^2)(u - f_x)$$
$$v_t = \Delta v - (f_x^2 + f_y^2)(v - f_y)$$

As GVF arises from energy minimization principles, we will describe it in detail in next Section.

1.1.3 Geometric Flows

Geometric flows encode shape evolutions, that is, those curve deformations that are independent of the parameterization. If $\gamma(v,0) := \gamma_0(v) = (x(v), y(v))$ is the initial curve, then its evolution in time is given by:

$$\gamma_t(v,t) = \alpha(v,t)\overrightarrow{t}(v,t) + \beta(v,t)\overrightarrow{n}(v,t)$$

with $\overrightarrow{t}$, $\overrightarrow{n}$ the curve tangent and normal vectors, respectively, and α, β smooth functions depending on the local geometry of the curve. This last requirement limits both functions to depend on the curve unit tangent, θ, and the curve curvature, κ.

Since a change of parameter in a curve does not alter its shape but only the speed we are travelling on the curve, we have infinitely many formulations representing the same curve evolution (although the function of the embedding, γ, may change). In fact, since tangent motion just redistributes (mass) points along the curve, we have that [29], up to a change of parameter, any geometric flow is given by:

$$\gamma_t(u,t) = \beta\overrightarrow{n}$$

Thanks to their independence upon the curve parameter, geometric flows can be applied to image filtering through an implicit level-set formulation [48], [65]:

$$u_t = |\nabla u|\beta(\theta,\kappa) = |\nabla u|\beta\left(\frac{\nabla u}{|\nabla u|}, \operatorname{div}\left(\frac{\nabla u}{|\nabla u|}\right)\right)$$

Although in their implicit formulation they are highly non-linear equations, geometric flows adjust to the heat-like model in a proper curve parameter. In [24] it is proved that, in the arc-length parameter, the angle of the curve unit tangent, θ, and the curve curvature, κ, follow PDE's:

$$\theta_t(s,t) = \partial_s(\beta) + \left(\int_0^s \beta\theta_s ds\right)\theta_s$$

$$\kappa_t(s,t) = \beta\kappa^2 + \beta_{ss} + (\int_0^s \beta\kappa ds)\kappa_s$$

which are of heat diffusion type as $\beta = \beta(\theta,\kappa)$.

In order to guarantee that the original shape γ_0 will be smoothed, the total Gaussian curvature, $\overline{\kappa}(t) = \int_0^1 |\kappa|\sqrt{\dot{x}^2 + \dot{y}^2}du$, and the number of inflexion points must decrease in time. A main advantage of curvature based image filtering techniques over diffusion processes [48], [39] is that, as they are contrast preserving [1], they modify the shapes of edges without blurring. The most popular curvature based techniques are:

Example 1.1.8 *Mean Curvature Flow*

This flow, also known as Geometric Heat Equation, is one of the most widely studied geometric flows ([32], [33], [34] or [40]). Its formulation for curves is given by:

$$\gamma_t(u,t) = \kappa \overrightarrow{n} \tag{1.12}$$

The word Geometric Heat Equation applies because in arc length parameter, we have that the diffusion term of the PDE that the angle follows is the Laplacian:

$$\theta_t(s,t) = \partial_s(\theta_s) + \left(\int_0^s \theta_s^2 ds\right)\theta_s = \theta_{ss} + \left(\int_0^s \theta_s^2 ds\right)\theta_s$$

General arguments on non-linear PDE's [32] yield that, as far as the curvature (θ_s) remains bounded, a unique solution fulfilling the necessary conditions to smooth irregularities exists. Besides, we have a complete description of the asymptotic behavior of the mean curvature flow:

Proposition 1.1.1 [32] [33] *Let $\gamma(t,u)$ be the solution to the geometric heat equation:*

$$\gamma_t = \kappa \overrightarrow{n}$$

with initial condition a closed simple smooth curve. Then, $\gamma(t,u)$ becomes a circle and finally collapses to a point.

This Proposition supplies images and curves evolving under the curvature flow with a desirable property for a scale-space analysis [1], [41], which studies images/shapes at different level of detail by means of a progressive simplification of their shapes and features. However, as in the case of diffusion processes, this property represents a main drawback if one is to use such equation just to smooth irregularities, as it requires a stopping time in order to preserve enough features as to recognize the original shapes in the image. Up to this moment, techniques developed to cope with trivial final curves focus on converging to a particular geometric model of shapes:

Example 1.1.9 *Stochastic Geometric Flows*

Basing on the stochastic process that models evolution of a pixel, this geometric flow [79] adds a factor to the mean curvature flow that cancels on polygons of N-vertices:

$$\cos^2(N\theta)\kappa\overrightarrow{n} \quad \text{or} \quad \sin^2(N\theta)\kappa\overrightarrow{n}$$

The resulting image filtering drives all level sets to a polygon given a priori, which limits the technique applicability to images presenting different geometric designs.

Although, strictly speaking, it can not be considered a geometric flow (it depends on the embedding image), the next curvature based evolution achieves more accurate shape models:

Example 1.1.10 *Min/Max Flow*

In [49] Malladi and Sethian introduced the following curvature-based image evolution:

$$u_t = \begin{cases} min(\kappa, 0) & \text{if } \Phi(x,y) < \upsilon \\ max(\kappa, 0) & \text{if } \Phi(x,y) \geq \upsilon \end{cases}$$

where $\Phi(x,y)$ is the average of all pixel values in a window centered at (x,y) and υ is the mean value in the window on the level curve to be smoothed. In the case of real images, the authors suggest using the image gradient to switch between evolution under positive and negative curvature:

$$u_t = \begin{cases} min(\kappa, 0) & \text{if } \Phi(|\nabla u|) < \upsilon \\ max(\kappa, 0) & \text{if } \Phi(|\nabla u|) \geq \upsilon \end{cases}$$

for $\Phi(|\nabla u|)$ an average of the norm $|\nabla u|$ and υ a threshold value determining whether the curve is considered an edge or not.

In any case, the steady state of the equation is a polygonal curve that approaches the original shape.

Selective shape smoothing based on the curve regularity rather than on its geometry will be addressed in Chapter 2

1.2 Minimization Processes

Most of the former techniques minimize an energy functional and its formulation derives from the gradient descent of such energy. In fact, energy minimization flows are the main sources of PDE's that do not conform to the model of a heat-like equation.

Let us review the variational principles that rule functional minimization. For any function/curve, v, a functional, E, is defined as the integral:

$$E(v) = \int_0^1 L(v(x), \nabla u(x), x)dx = \int L(z, p, x)dx$$

where L is commonly known as *Lagrangian*.

As in the case of functions in $\mathbb{R}^n$, cancellation of E first derivative characterizes its minima/maxima. The functional first derivative or *first variation* is obtained as follows. For any function ν and any real number δ, we will call a perturbation of u any function of the form $\tilde{u} = u + \delta\nu$. It should be clear that the derivative with respect to δ evaluated at $\delta = 0$ yields the functional first variation at a point u provided that L is smooth in all its arguments (z, p, x). Hence, if we denote:

$$E(\delta) = \int L(ua + \delta\nu, \nabla u + \delta\nabla\nu, x)$$

Then the first variation of E at a point u is given by:

$$E'(0) := \partial_\delta \left(\int L(u(x) + \delta\nu(x), \nabla u(x) + \delta\nabla\nu(x), x)dx \right) =$$
$$\int (\langle L_z(u, \nabla u, x), \nu\rangle + \langle L_p(u, \nabla u, x), \nabla\nu\rangle)dx \tag{1.13}$$

The functional E has a critical point if the above integral cancels for any ν. Assuming the usual boundary conditions (Dirichlet, Neumman or periodic), integration by parts yields:

$$E'(0) = \int \langle L_z - (L_p)_x, \nu \rangle dx = \int \langle L_z - \mathrm{div}(L_p), \nu \rangle dx = 0 \tag{1.14}$$

which implies that extremal curves of E solve:
Euler-Lagrange equations

$$0 = L_z - (L_p)_x \tag{1.15}$$

or equivalently, that they correspond to the stationary points of the dynamical system, which is analogous to the gradient descent [30], given by:

$$u_t(x,t) = -L_z + (L_p)_x \tag{1.16}$$

Unfortunately, the converse does not always hold, that is, not all points cancelling (1.16) are extreme points of the functional. As in the case of functions in $\mathbb{R}^n$, an analysis of the functional second variation determines the false minima. This second derivative, $E^{''}(0)$, is found by means of differentiating once again the expression (1.13) with respect to δ and evaluating at $\delta = 0$:

$$E^{''}(0) := \int (\nu^t L_{zz}(u, \nabla u, x)\nu + (\nabla \nu)^t L_{pp}(u, \nabla u, x)\nabla \nu + 2\nu^t L_{zp}(u, \nabla u, x)\nabla \nu) du$$

where second derivatives should be understood in the context of symmetric 2-forms. In this framework we will use the notation $E^{''}(\nu_1, \nu_2)$ to denote the former symmetric form applied to the functions ν_1 and ν_2. If the second variation is (strictly) positive definite, the functional is called (strictly) convex. In this case, we can ensure [23] that any function cancelling (1.13) is a stable stationary point (if convexity is strict) and, further, a minima of E. In fact, convexity of the functional is equivalent to the ellipticity condition for second order operators:

Example 1.2.1 *Convexity and Ellipticity for Minimizing Diffusions*

Let $J(x)$ be an $n \times n$ symmetric matrix and, for each integrable smooth function $u : \Omega \subset \mathbb{R}^n \to \mathbb{R}$ consider the energy functional given by:

$$E(u) := \int_\Omega |\nabla u|_J dx = \int_\Omega \nabla u^t J \nabla u dx = \int L(\nabla u, x) dx = \int L(p, x) dx$$

On one hand, the gradient descent of the former functional is:

$$u_t = \mathrm{div}(J \nabla u) = \mathrm{div}(L_p)$$

On the other hand, the ellipticity condition that guarantees uniqueness of a weak solution reads:

$$\int (\nabla v)^t J \nabla v \geq C \int |\nabla v|^2$$

which is exactly the condition that E is uniformly convex:

$$E^{''}(v,v) = \int (\nabla v)^t L_{pp} \nabla v = \int (\nabla v)^t J \nabla v \geq C \int |\nabla v|^2$$

Apart from the Gaussian filtering, image in-painting and mean curvature flow described in the previous Section, there are some other techniques developed from variational principles:

1.2.1 Close-to-Data Constrains

This family of operators arise as a solution to avoid the convergence to trivial steady states that mares efficiency of diffusion processes. The idea is to constrain the solutions to a diffusion equation (1.5) to take equal values than the original function at the function descriptive curves (edges, ridges). Such (Dirichlet-like) restrictions easily are easily modelled in terms of energy minimization and result in adding a reaction term to the diffusion equation.

1. **Half-Quadratic minimization**

   These approaches ([2], [43]) base on the minimization of the functional:

   $$E(u) = \int \int \frac{\alpha}{2}(u - u_0)^2 + \Phi(|\nabla u|) dx dy$$

   where u_0 is the image to be filtered. The corresponding Euler-Lagrange equations correspond to a gradient descent flow:

   $$u_t = \text{div}(g(|\nabla u|^2)\nabla u) + 2\alpha(u_0 - u) \quad \text{for} \quad g = \frac{\Phi'(|\nabla u|)}{|\nabla u|} \tag{1.17}$$

   that is a diffusion equation with a reaction term weighted by α. Since this parameter weights the influence of the close-to-data constrain [62], it determines the similarity between the original noisy image, u_0, and its filtered version. Although it prevents the flow from having a trivial (i.e. constant image) steady state, an inappropriate (high) value for α troubles the denoising process.

2. **Gradient Vector Flow**

   As already mentioned in Section 1.11 these methods ([75], [76], [77]) regularize and extend vector fields. The smoothing diffusion term and the value constrain extension term arise from the minimization of the energy functional:

   $$\begin{aligned} E(u(x,y), v(x,y)) = E(V) &= \int |V|^2 + \int |f|^2 |V - f|^2 = \\ &= \int (u_x^2 + u_y^2 + v_x^2 + v_y^2) + \int (f_x^2 + f_y^2)((u - f_x)^2 + (v - f_y)^2) \end{aligned} \tag{1.18}$$

   for $f = (f_x, f_y)$ the vector field to be extended and regularized. Using calculus of variations, it follows that GVF is the steady state of:

   $$\begin{aligned} u_t &= \Delta u - (f_x^2 + f_y^2)(u - f_x) \\ v_t &= \Delta v - (f_x^2 + f_y^2)(v - f_y) \end{aligned}$$

The functional version (1.18) provides a simple interpretation of each of the terms. Because each diffusion Δu, Δv corresponds to minimizing the total variation, $\int(u_x^2 + u_y^2)$, $\int(v_x^2 + v_y^2)$ of the functions, it yields regularity to the solution. Meanwhile the reaction terms $(f_x^2 + f_y^2)(u - f_x)$, $(f_x^2 + f_y^2)(v - f_y)$ impose a restriction on GVF values, as at those points where the norm of the original vector field is large, GVF must minimize $\int(f_x^2+f_y^2)((u-f_x)^2+(v-f_y)^2)$, which is minimum when (u, v) coincides with the original vector field.

In most cases, the vector field to be extended/regularized is the gradient of an external potential that serves to guide a deformable curve to a given image curve:

1.2.2 Snakes

Snakes constitute another important family of techniques based on calculus of variations principles. Snakes are curves that serve to segment image objects whose boundaries are characterized by a lack of differentiability of the image (edges, ridges). A measure of such irregularity serves as an attractor external energy, E_{ext}, that it is minimum at the target object. The snake is, then, the curve that achieves a compromise between minimizing this energy and conforming to a given degree of regularity. Different ways of imposing the latter internal energy give rise to two main snake models:

1. **Parametric Snakes**

   Parametric deformable models [38], [47] use Newton mechanics laws to define their internal constrains, which are given in terms of elasticity and stretching of the curve. In mathematical terms, the snake is the curve $\gamma(u) = (x(u), y(u))$ that minimizes the energy functional:

   $$E(\gamma) = \int_\gamma (E_{int} + E_{ext})du = \int_\gamma (\alpha||\dot{\gamma}||^2 + \beta||\ddot{\gamma}||^2 + E_{ext})du \ ,$$

   where α, $\beta \in [0, 1]$ determine the trade-off between length and curvature minimization. The usual external potentials, E_{ext}, are either the gradient map, $g = \frac{1}{1+|\nabla u|^2}$, or the distance map to image edges. In the general case, the curves minimizing such potentials are unconnected, so that the snake uses its internal energy to obtain a close model. The α-term (elasticity) linearly interpolates object contours producing a piece wise linear model of the curve. A higher regularity is achieve thanks to the β-curvature minimizing term (rigidity) because it penalizes curves corners and undulations. This makes the snake smoothly approach the unconnected set of points and allows it swallowing isolated set of points (outliers) product of image noise.

   A main inconvenience of physics-based snakes is that they handle an explicit curve parameterization (sampling), which difficulties modelling more than one object and requires dynamic updating during the snake evolution.

2. **Geodesic Deformable Models**

Geodesic snakes [11], [12] are an alternative to physics-based snakes based on the theory of curve evolution and level sets methods [57]. In particular, the solution to the problem is the curve (γ) of minimum length in a Riemannian surface with a metric (g) depending on the image contrast changes. It follows that if we note by u the image to be segmented, the geodesic functional is given by:

$$E_{geod} = \int_{\Gamma} g \ ds \qquad \text{with} \qquad g = \frac{1}{1 + |\nabla u|^2} \tag{1.19}$$

The normal component of the Euler-Lagrange formulation characterizes geodesic snakes as the steady curve of

$$\frac{\partial \gamma}{\partial t} = (g \cdot \kappa - < \nabla g, \vec{n} >) \cdot \vec{n} \tag{1.20}$$

We can give the following interpretation to each of the terms involved in the above formula. The role of $< \nabla g, \vec{n} > \vec{n}$ is pretty clear: it is a vector field pointing to the region of interest that attracts the snake to its boundary. Notice that in the standard formulation (1.19) the scope of this static term reduces to a narrow environ of the boundaries of interest. The curvature term, $g \cdot \kappa \vec{n}$, influences different aspects of the snake evolution. On one hand, it defines its motion when it is located far away from the object boundaries. On the other one, it serves as a curve regularizing term, ensuring continuity of the final segmenting snake in a similar fashion [78] the α-term of parametric snakes does. Finally, it gives the process a smooth behavior and ensures continuity during the deformation, in the sense that it prevents shock formation [23]. However, incorporating the curvature term into the convergence scheme difficulties the snake convergence to concave areas. In order to increase convergence to concavities and to speed up the evolution a constant velocity term in the direction of the normal component is usually added to the evolution equation giving rise to 'balloon'-like snakes [16]. The new term corresponds to area minimization and results in a constant dynamic speed in the gradient descent:

$$\frac{\partial \gamma}{\partial t} = (g \cdot \kappa + g V_0 - < \nabla g, \vec{n} >) \cdot \vec{n} \tag{1.21}$$

The behavior of the above techniques will be discussed in deeper detail in Chapters 3 and 5.3 where we will describe a new external energy ensuring convergence of parametric snakes whatever the geometry of the set of points to be approached.

Chapter 2

Regularized Curvature Flow: The Geometric Perona-Malik Approach

A theoretical analysis of recent filtering techniques [24] points out that if an image smoothing operator is to be robust against strong noisy images, it should be independent of image intensity. Essential advantage in this context is represented by geometric flows [32], [49]. As image smoothing relies exclusively on the geometry of its level curves, geometric flows do not produce any edge blurring [1], [39], which makes these techniques more robust in very noisy images. However, the fact that they reduce high curvature values and the number of inflexion points whatever the regularity of the curve, limits their applicability to shape recovery. We argue that any filtering technique to be used within a shape recovery algorithm, should take into account differentiability of the curve. Smoothing should only be applied to those arc of the curve presenting a given degree of irregularity. This need of a selective shape filtering leads to the formulation of a function measuring lack of smoothness in a shape.

We propose a novel geometric flow that penalizes irregularity in the curvature rather than its magnitude. To this purpose we develop a simple criterion to measure the degree of local irregularity present in the curve, which is added as stopping factor in the mean curvature flow. The resulting evolution equation profits the smoothing effects of the mean curvature flow to smooth those curve arcs that have a significant irregular shape. We will call this geometric flow as Regularized Curvature Flow, denoted by RCF for short.

The first relevant property of RCF is that the evolution converges to a smooth curve that keeps high resemblance to the original noisy shape. This fact is one of RCF main advantages over other geometric flows yielding non-trivial curves. First because RCF final state is smoother than the polygonal shapes that [49], [79] produce. Second, because RCF formulation is simpler and faster than the 4th order [46] or level-sets decomposition techniques [11], [52]. Another significant improvement is that RCF parameters are independent of the geometry of the initial curve our method is applied to. In this fashion, the image operator, obtained through the level sets formulation [57], is suitable for shape recovery in non-user intervention applications. Furthermore,

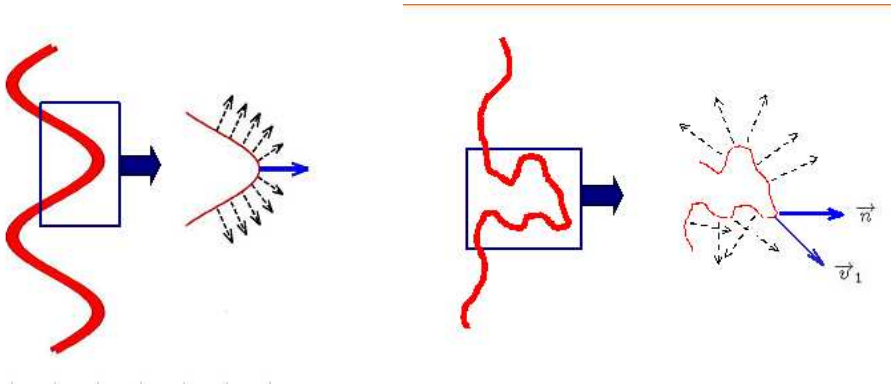

(a) (b)

Figure 2.1: Measure of shape irregularity in a regular, (a), and irregular, (b), arc .

RCF smooth evolution makes the iterative scheme used in its implementation to stop by means of standard numeric stop criteria [18], [70], [30]. This also constitutes an advantage over most PDE based techniques that either present an irregular evolution speed [49], [79] or rapidly converge to constant images [60], [72], [32]. Consequently, in practice, they must rely on a given image-dependant number of iterations to stop the evolution, meanwhile RCF admits equal stop parameters for any image. We take special care in studying the error made in RCF numeric implementation and the way this error affects the values of the parameters that rule RCF stabilization. Indeed we propose a new way of setting parametric values in terms of the maximum accuracy in the implementation.

2.1 A Selective Curvature Flow

Let us begin with introducing a roughness function that measures the degree of noise of a plane curve.

2.1.1 Definition of a Local Measure of Shape Irregularity

A plane curve is determined (up to rotations and translations) by the angular orientation, θ, of its unit tangent. Therefore, a reasonable approach for a stopping motion term is to consider a measure of θ smoothness. It should be clear that lack of differentiability in the angle θ corresponds to the variability of the normal unit vector $\overrightarrow{n}$ around each point. We argue that this rate of variability can be computed by means of the projection of $\overrightarrow{n}$ onto a robust mean of $\overrightarrow{n}$ in a neighborhood of each point. That is, it suffices to compare $\overrightarrow{n}$ to a smooth approximation, $\overrightarrow{v}_1$, of the vector. At regular/differential arcs, the former vectors should agree, meanwhile, in the presence of noise/irregularity, they will significantly differ (as the irregular shape of figure 2.1 illustrates).

We will make use of the structure tensor, J_ρ [36], computed over the unit normal in order to obtain the vector $\overrightarrow{v}_1$. We recall the reader that, given a regularization scale ρ, the structure tensor is defined as the convolution of the projection matrices onto $\overrightarrow{n} = (-\sin(\theta), \cos(\theta))$ with a gaussian G_ρ, of variance ρ and zero mean:

$$J_\rho = G_\rho * \left[\begin{pmatrix} -\sin(\theta) \\ \cos(\theta) \end{pmatrix} (-\sin(\theta), \cos(\theta)) \right] =$$
$$= \begin{pmatrix} G_\rho * \cos^2(\theta) & G_\rho * \cos(\theta)\sin(\theta) \\ G_\rho * \cos(\theta)\sin(\theta) & G_\rho * \sin^2(\theta) \end{pmatrix} = \begin{pmatrix} a_{11}(u) & a_{12}(u) \\ a_{12}(u) & a_{22}(u) \end{pmatrix}$$

We assert that the eigenvector of J_ρ of maximum eigenvalue suits our purposes. We define $v_1 = (\cos\psi, \sin\psi)$, in terms of the coefficients of J_ρ as:

$$A := \tan 2\psi = \frac{2a_{12}}{a_{11} - a_{22}} \tag{2.1}$$

The square norm of the vector product $\overrightarrow{v}_1 \times \overrightarrow{n}$ is the measure of curve irregularity we propose:

$$g(\theta) = ||\overrightarrow{v}_1 \times \overrightarrow{n}||^2 = \sin^2(\psi - \theta) \tag{2.2}$$

We will refer to the function g as **Roughness Measure**.

Remark: First notice that the discrete numeric implementation of a convolution with a gaussian is approximated by means of a windowed (squared) kernel or mask. This implies that discrete gaussians are functions of compact support. Second, even in the continuous domain, gaussian kernels are approximations of the identity for the convolution product. That is they converge to the dirac delta as the variance tends to zero. For this (among others) reason they are commonly used in the area of Fourier analysis as a tool to study the "local" behavior of functions [**?**], [**?**]. Based on the above considerations, we will refer to the Roughness Measure as local measure of irregularity, in spite of being just an approximation to the local behavior of a function in the continuous domain.

Let us intuitively explain why the function g conforms to the idea of a curve irregularity measure. The statement follows easily if one realizes that the function A is, in fact, equal to:

$$A = \frac{2a_{12}}{a_{11} - a_{22}} = \frac{2G_\rho * \cos(\theta)\sin(\theta)}{G_\rho * \cos^2(\theta) - G_\rho * \sin^2(\theta)} = \frac{G_\rho * \sin(2\theta)}{G_\rho * \cos(2\theta)}$$

That is, the factors of the quotient are the solutions to the heat equation at time $t = \rho$ with initial conditions $\sin(2\theta)$ and $\cos(2\theta)$. The function g compares, in a particular way, these quantities to the original functions $\sin(2\theta)$ and $\cos(2\theta)$. Therefore it is rather sensible to expect that those functions that cancel g will be smooth. For a rigorous mathematical justification we remit the reader to [24].

Properties of the Roughness Measure

These are the properties that make g suitable to our purposes:

1. Locally, it measures the degree of symmetry around each point, in particular it cancels on arcs of circles. This property makes our RCF stabilize finite unions of arcs of circles and straight lines.

2. Those curves that cancel g are $\mathcal{C}^\infty$ curves, i.e. they are infinitely smooth. This is convenient for a latter image processing procedure, since it ensures that higher order operators applied to the image level curves will be accurate.

The above considerations turn our roughness measure into the perfect candidate for a stopping evolution term in a mean curvature flow motion.

2.1.2 Formulation of the Regularized Curvature Flow

The **Regularized Geometric Heat Equation** we suggest is the geometric flow defined as:

$$\gamma_t(u,t) = g(\theta)\kappa\overrightarrow{n} \text{ with } \gamma(u,0) = \gamma_0(u) \tag{2.3}$$

where the function $g(\theta)$ is given by formula (2.2) and κ denotes the curvature. The numeric implementation through level sets formulation [65] is detailed in Section 2.2.1.

Properties of RCF

Let us enumerate those properties of RCF that ensure shape simplification and convergence to non trivial steady curves.

1. No new inflexion points (i.e. zeros of the curvature) are created.

2. The total Gaussian curvature, $\overline{\kappa}(t) = \int_0^1 |\kappa|\sqrt{\dot{x}^2 + \dot{y}^2}du$, decreases over the orbits of (2.3).

   These two properties guarantee that the evolution under RCF will simplify shapes. Their geometric interpretation is that the curve oscillation, i.e. its total variation, reduces in time. This fact ensures that, given an initial curve γ_0, its evolution will neither become more irregular (property 1), nor stretch (property 2): its only possible evolution is a progressive reduction of oscillations This does not constitute a great novelty, since RCF shares this behavior with the other geometric flows [40], [32], [49], [79]. The differential feature that makes RCF more suitable for shape reconstruction purposes is its different asymptotic behavior, which is described by means of the following properties:

3. Whatever initial shape, its evolution under RCF converges, in time, to the steady states of (2.3) given by $g\kappa \equiv 0$.

   First, notice that the above statement is not a triviality since the limit set of an orbit could, perfectly, be a periodic orbit. The existence of Lyapunov functionals for RCF (i.e. functions that decrease along the orbits) excludes this possibility. Second, observe that the former property guarantees that the numeric iterative implementation admits a stop criterion in terms of the magnitude of the speed $g\kappa \equiv 0$.

This final state will never be a single round point like in the evolution by mean curvature flow [32], [33]. This follows from the fact that the roughness measure cancels on circles, which prevents the evolution from collapsing to a point.

4. Steady states of (2.3) are simple closed curves.

   Finally, we have that the amount of shape irregularity, according to our roughness measure, of the final state of (2.3) is smaller than the one of the initial curve. In fact, it can be shown (Section2.3) that:

5. The roughness measure g tends to zero over the solutions to (2.3).

   Therefore, by virtue of the second property of g, solutions to RCF tend asymptotically to a $\mathcal{C}^\infty$ curve, which is the fixed point of equation (2.3) given by $g \equiv 0$. Indeed, we have empirically checked that evolution under RCF converges to a smooth curve that conserves features significant enough to identify the original noisy shape. This already constitutes an advantage over other PDE-based techniques. Firstly, it ensures a higher order smoothness of final curves than the polygonal shapes yielded by [49], [79]. Secondly, the value of RCF unique parameter (ρ) is set according to the desired degree of differentiability. Differentiability is a property which is not linked to either resemblance to the original image/shape [46], [9], [62], geometry of its level sets [79] or level of detail [11], [52]. It follows that with a fixed set of parametric values RCF converges, by its own design, to smooth curves resembling the original ones. Finally, property 5 provides the technique with a natural stop criterion in terms of the magnitude of the roughness measure.

2.2 Numerical Issues

2.2.1 Level Sets Approximation

The level sets implicit formulation of RCF is given by:

$$u_t = g\left(\frac{\nabla u}{|\nabla u|}\right)|\nabla u|\,\mathrm{div}\left(\frac{\nabla u}{|\nabla u|}\right) = g\left(\frac{\nabla u}{|\nabla u|}\right)\frac{u_{xx}u_y^2 - 2u_{xy}u_x u_y + u_{yy}u_x^2}{|\nabla u|^2}$$

The exact implementation would imply tracking, for each image pixel, its level curve in order to perform the convolution with a one dimensional gaussian kernel along the level-line. Since this is computationally unfeasible we propose an approximate algorithm, which consists in computing the roughness measure using a gaussian in two variables, $G_\rho(x,y) = \frac{1}{2\pi\rho^2}e^{-(x^2/2\rho^2)-(y^2/2\rho^2)}$. That is, the structure tensor is computed by means of the formula:

$$\tilde{J}_\rho(x,y) = \int G_\rho(\tilde{x}-x, \tilde{y}-y)\cdot\left[\left(\frac{\nabla u}{|\nabla u|}\right)\otimes\left(\frac{\nabla u}{|\nabla u|}\right)\right]d\tilde{x}d\tilde{y}$$

Notice that in the discrete implementation the above integral is computed over a window centered at each image pixel of size $2\epsilon \times 2\epsilon$.

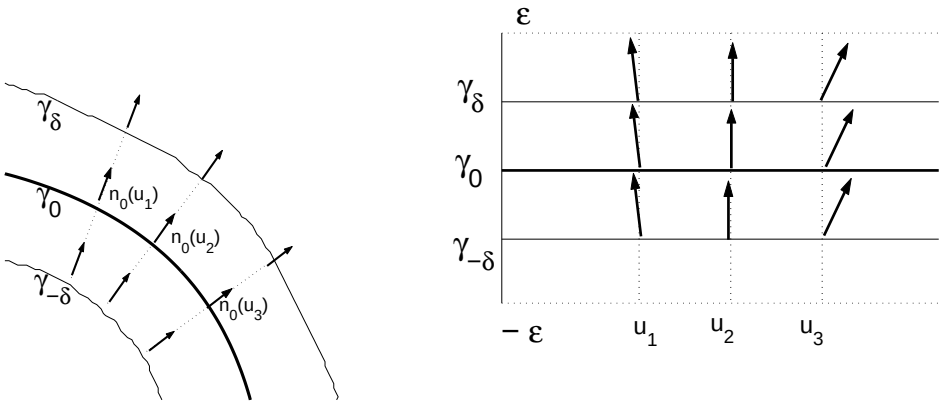

(a) (b)

Figure 2.2: Normal vectors in a tubular neighborhood (a) and tube parameter domain (b)

Let γ_0 denote the target curve and δ the distance from an image pixel (x, y) to γ_0. Then, the relation between $\tilde{J}(x, y)$ and the true structure tensor, $J(x)$, computed along γ_0 is given by:

$$\tilde{J} = J + \delta \int G(x) \cdot (\kappa_{Im} - \kappa_0 \tan(\theta))(t_0 \otimes n_0)dx + \mathcal{O}(\delta^2) \tag{2.4}$$

where κ_0 stands for the curvature of γ_0 and κ_{Im} for the flow lines curvature. It follows that the error made is bounded by:

$$\begin{aligned} Error = |J_\rho - \tilde{J}_\rho| \leq \epsilon \left(C \int |\kappa_0| + \int |\kappa_{Im}| \right) ||\overrightarrow{t}_0 \otimes \overrightarrow{n}_0|| + \\ + \mathcal{O}(\epsilon^2) = E(\gamma_0) + E(Im) + \mathcal{O}(\epsilon^2) \end{aligned} \tag{2.5}$$

We remit the reader to the Appendix for the mathematical argumentation that leads to the above formula. Let us analyze the meaning of each of the terms involved in (2.5) and the way the error affects in the numeric implementation of RCF.

Two are the main sources of error in formula (2.5). The term $E(Im)$, proportional to the rate of variation of the unit normal to γ_0 along the flow lines, comes from the initial embedding function. First notice that, in the particular ideal case of the signed distance map, this term cancels. This follows because distance maps are, locally, the embedding of a tubular neighborhood of γ_0. Hence, normal vectors to the level curves in a band around γ_0 are constant in the gradient direction as the drawing of fig.2.2(a) shows. Also notice that for images with uniform areas bounded by edges, $E(Im)$ is nearly negligible because border curves correspond to inflexion points in the image gradient direction and, hence, $\kappa_{Im} = 0$. Only images with regular level curves on a textured or noisy background may evolve in a way such that motion of level

curves differs from RCF due to an arbitrary huge $E(Im)$. In the first stages of the evolution, the roughness measure could cancel on the regular curve but not in the noisy neighborhood. However, as the image evolves, since background variation decreases, $E(Im)$ asymptotically decreases to a small positive value and the evolution tends to agree to that of the ideal signed distance map. We observe that some curvature based techniques successfully used in image processing (such as the image average based min/max flow [49]) present a similar pathology. Moreover our numerical experiments show that the dependency upon the initial embedding function does not significantly affect the final shapes achieved with RCF.

The first summand in (2.5), $E(\gamma_0)$, measures the error made in using the image cartesian coordinates, (x, y), instead of the tubular coordinates given by the curve parameter, u, and the parameter, δ, of the normal line $n_0(u)$ (fig.2.2(b)). Because it corresponds to the term $-\kappa_0 \tan(\theta)(t_0 \otimes n_0)$ of formula (2.4) it vanishes when the curve is symmetric around the point. It follows that for finite unions of circles and straight lines the only source of error is the one introduced by the embedding function. For other curves, first notice that $E(\gamma_0)$ is bounded by the total gaussian curvature of the target curve γ_0. Second that, in the case of a positive g, RCF level sets formulation agrees with the mean curvature flow. Curves evolving under the mean curvature flow [32], [33] converge to a circle of radius namely R, and then collapse to a point. Furthermore, their total gaussian curvature, before reaching the limit circle, is a decreasing function of time. The latter implies that $E(\gamma_0)$ only blows when a level curve collapses (which happens a finite number of times) and keeps bounded for the remains of the evolution:

$$2\pi R \leq E(\gamma_0) = \int |\kappa_0(u,t)| \leq \int |\kappa_0(u,0)|$$

The former analysis of the level sets formulation of RCF points the following. Evolution of distance maps perfectly matches the curve formulation of RCF in the sense that all properties given in Section 2.1 are preserved and, hence, stabilization can be detected by means of the magnitude of g. In the general case, the roughness measure does not tend to zero but to the positive value that depends on the initial embedding image. The length of the time intervals where the former behavior holds hinges upon the level sets topology. This numerical error introduced in the computation of RCF difficulties using an evolution stop criterion in terms of the magnitude of g and motivates searching for an alternate.

2.2.2 RCF Best Parametric Values

Parameters involved in any numeric implementation can be split into the ones that are inherent to the method implemented and those concerning the numeric algorithm. In the case of RCF, these two sets reduce to:

- **RCF Parameters**: ρ

  This parameter controls smoothness of the final curves and, by virtue of (2.5), it also influences in the error made in RCF implicit approximation. This fact limits, for the sake of error minimization, the magnitude of ρ to values less or equal to 1. Indeed we always use $\rho = 0.5$ in our experiments.

- **Numeric Parameters**

  1. **Stop Parameters:** $\{\epsilon, T\}$

     The value of ϵ determines the maximum amplitude of the roughness measure oscillations. Because g decreases smoothly on the orbits of RCF, ϵ can be arbitrarily small ($\epsilon = 10^{-3}, 10^{-4}$).

     In (real) images presenting a rich level set topology, the length of the time interval T influences on the level of detail of the longest level curves (we remit the reader to Section 5.1.3 for examples on the impact of this parameter). Because these curves are usually descriptive of image features we recommend using $T < 50$.

     Experiments in Sections 5.1.2 and 5.1.3 show that the set $\{\epsilon = 10^{-3}, T = 50\}$ guarantees noise removal and geometry preservation.

  2. **Gray-Level of Target Curve:** α_0

     Since geometric flows are designed for curves rather than for images, the proper way to apply them to image denoising is through a level set decomposition ([11], [52]). Because such decomposition adds an extra computational cost, we suggest filtering the image itself and computing any stop quantity over a curve (manually chosen) describing the image features. In this manner, stopping quantities are smoother in time (see Section 5.1.3) so that standard stabilization criteria work fine.

2.3 Mathematical Issues

2.3.1 Properties of the roughness measure

In this section, we will prove the local and global properties of the roughness function g (given in Section 2.1.1) which describe the curves that cancel this function. On one hand, we will show that, locally, our roughness measure g measures the degree of symmetry of the curve. And on the other, we will see that the function g really measures the amount of irregularity on the curve, as those curves that cancel g are $\mathcal{C}^\infty$ curves.

In order to analyze the local properties, we first notice that g cancels at those points such that $\psi - \theta = 0$. The latter quantity is nothing but the angle of v_1 with respect to the unit normal at each point. This fact motivates, for the sake of notational simplicity, using 'gauge' coordinates. That is, in order to determine what characterizes points $\gamma(u_0)$ such that $g(\theta(u_0), u_0) = 0$, we can take as coordinate system in $\mathbb{R}^2$ the one given by $\overrightarrow{t}(u_0)$, $\overrightarrow{n}(u_0)$. Notice that taking angles with respect the axis given by $\overrightarrow{n}(u_0)$, the roughness measure equals $\sin^2(\arctan(A))$. Thus if one is to prove that g cancels in symmetric situations it suffices to check that at a point $u = u_0$, such that $g = 0$, A computed with respect to $\overrightarrow{n}(u_0)$ cancels.

Proposition 2.3.1 *If the angle of the tangent does not turn more that $\pi/2$, the function g measures the degree of symmetry of the curve around each point.*

Proof. Using 'gauge' coordinates, it suffices to check that $A(u_0) = 0$. We assert that the latter equality is satisfied if and only if $a_{12}(u_0) = 0$. This follows because, by hypothesis, θ does not turn more that $\pi/2$ and we can assure that $a_{11} - a_{22} = \int_{-\infty}^{\infty} G_\rho(u)\cos(2\theta(u)) \neq 0$. If we further take $u_0 = 0$, the coefficient a_{12} equals:

$$a_{12}(0) = \frac{1}{2}\int_{-\infty}^{\infty} G_\rho(u)\sin(2\theta(u))du = \frac{1}{2}\int_{-\infty}^{0} G_\rho(u)\sin(2\theta(u))du + \\ + \frac{1}{2}\int_{0}^{\infty} G_\rho(u)\sin(2\theta(u))du$$

By changing the integration variable of the second integral by $-u$, we obtain:

$$a_{12}(0) = \frac{1}{2}\int_{-\infty}^{0} G_\rho(u)\sin(2\theta(u))du + \frac{1}{2}\int_{-\infty}^{0} G_\rho(-u)\sin(2\theta(-u))du$$

Now, by assumption, the curve is symmetric around zero (i.e. $\theta(-u) = -\theta(u)$), so that by symmetry of the gaussian we obtain:

$$a_{12}(0) = \frac{1}{2}\int_{-\infty}^{0} G_\rho(u)\sin(2\theta(u))du - \frac{1}{2}\int_{-\infty}^{0} G_\rho(u)\sin(2\theta(u))du = 0$$

□

In the discrete version of RCF, since gaussian kernels are of compact support, the above result implies that g measures the local degree of symmetry in a curve. That is, for a given scale ρ, it cancels at those points, $u = u_0$ where the curve is symmetric in a neighborhood of length $2\rho + 1$ centered at u_0. The former Proposition and symmetry of circles yields:

Corollary 2.3.1 *At whatever scale, ρ, the function (2.2) cancels on circles.*

Concerning those curves having null roughness measure, we have the following global result:

Theorem 2.3.1 *Let γ be a curve such that $g \equiv 0$. Then the angle of the tangent θ is a $\mathcal{C}^\infty$ function*

Proof. Notice that the roughness measure cancels if and only if:

$$0 \equiv \tan(\arctan(A) - 2\theta) = \frac{\tan(\arctan(A)) - \tan(2\theta)}{1 + \tan(\arctan(A))\tan(2\theta)} = \frac{A - \tan(\theta)}{1 + A\tan(2\theta)}$$

Hence, it cancels on those functions such that:

$$\frac{G_\rho * \sin(2\theta)}{G_\rho * \cos(2\theta)} = \frac{\sin(2\theta)}{\cos(2\theta)}$$

Or equivalently:

$$\frac{G_\rho * \sin(2\theta)}{\sin(2\theta)} = \frac{G_\rho * \cos(2\theta)}{\cos(2\theta)} = f(\rho, s)$$

That means that we have the following two equalities:

$$G_\rho * \sin(2\theta) = f(\rho, s)\sin(2\theta) \quad \text{and} \quad G_\rho * \cos(2\theta) = f(\rho, s)\cos(2\theta) \tag{2.6}$$

Now, as noticed at the beginning of the section, the functions $\tilde{S} := G_\rho * \sin(2\theta)$ and $\tilde{C} := G_\rho * \cos(2\theta)$ are solutions to the heat equation at time $t = \rho$, so they are $\mathcal{C}^\infty$. We will show that this fact makes the functions f and θ belong to the Sobolev spaces H^k for any k. General theory on Sobolev spaces [23] yields that f, $\theta \in \mathcal{C}^\infty$. We will begin with proving that they belong to H^1 and, then, proceed by induction. In order to prove the assertion it suffices to check [23] that the L^2-norm of the incremental quotients of f and θ is uniformly bounded. By definition, the incremental quotient of a function v is defined as:

$$D^h(v) := \frac{v(s) - v(s+h)}{h}$$

Taking difference quotients in equations (2.6), we obtain:

$$\left.\begin{array}{l} D^h(\tilde{S}) = D^h(f)\sin(\phi) + D^h(\phi) f\cos(\phi) \\ D^h(\tilde{C}) = D^h(f)\cos(\phi) - D^h(\phi) f\sin(\phi) \end{array}\right\}$$

Therefore we have that:

$$\int D^h(f)^2 + D^h(\phi)^2 f^2 = \int D^h(\tilde{S})^2 + D^h(\tilde{C})^2 \leq \int \tilde{S}_s^2 + \tilde{C}_s^2 < M < \infty$$

If $f^2 > \epsilon > 0$, then the above inequality yields that f, $\phi \in H^1$. Taking difference quotients over first derivatives, we get:

$$\left.\begin{array}{l} D^h(\tilde{S}_s) = D^h(f_s)\sin(\phi) + 2\phi_s f_s\cos(\phi) + D^h(\phi_s) f\cos(\phi) - \phi_s^2 f\sin(\phi) \\ D^h(\tilde{C}_s) = D^h(f_s)\cos(\phi) - 2\phi_s f_s\sin(\phi) - D^h(\phi_s) f\sin(\phi) - \phi_s^2 f\cos(\phi) \end{array}\right\}$$

Taking the sum of squares and integrating, we get that:

$$\begin{aligned} \infty > M > \int \tilde{S}_{ss}^2 + \tilde{C}_{ss}^2 \geq \int D^h(f_s)^2 - 2\phi_s^2 f D^h(f_s) + 4\phi_s^2 f_s^2 + 4D^h(\phi_s)\phi_s f f_s + \\ + D^h(\phi_s)^2 f^2 + \phi_s^4 f^2 = \int D^h(f_s)^2 + \int D^h(\phi_s^2)\partial_s(f^2) + 2\int \phi_s^2 f_s^2 + \\ + 4\int \phi_s^2 f_s^2 + \int D^h(\phi_s^2)\partial_s(f^2) + \int D^h(\phi_s)^2 f^2 + \int \phi_s^4 f^2 > \int D^h(f_s)^2 + \\ + \int D^h(\phi_s)^2 f^2 + 2\int D^h(\phi_s^2)\partial_s(f^2) = \int D^h(f_s)^2 + \int D^h(\phi_s)^2 f^2 - \\ - 2\int \phi_s^2 D^h(\partial_s(f^2)) \end{aligned} \tag{2.7}$$

Now, developing derivatives, the last integral equals:

$$\begin{aligned} -2\int \phi_s^2 D^h(\partial_s(f^2)) = -4\int \phi_s^2 D^h(f f_s) = -4\int \phi^2 f_s^2 - 4\int f\phi_s^2 D^h(f_s) \geq \\ \geq -4\int \phi^2 f_s^2 - 4\epsilon\int D^h(f_s)^2 - \frac{4}{4\epsilon}\int f^2\phi_s^4 \end{aligned}$$

Where we obtain the last inequality by applying Cauchy. Replacing this expression into (2.7) we get the following bound on the second incremental differences:

$$(1-4\epsilon)\int D^h(f_s)^2 + \int D^h(\phi_s)^2 f^2 < M + 4\int \phi^2 f_s^2 + \frac{4}{\epsilon}\int f^2\phi_s^4 < C < \infty$$

The last inequality follows from the bound on $\int f^2\phi_s^4$ obtained from:

$$M > \int (\cos(\phi)\tilde{S} - \sin(\phi)\tilde{C})^4 = \int f^4\phi_s^4 > \epsilon\int f^2\phi_s^4$$

Hence, if $f^2 > 0$, we get that f and ϕ belong to H^2. Taking higher order incremental differences, we have that:

$$\int D^h(f^{n)})^2 + \int f^2 D^h(\phi^{n)})^2 + \text{Previously bounded terms} \leq M < \infty$$

So both functions, f and ϕ belong to H^k for any k and, thus, they are smooth functions.

The last thing to prove is that $f^2 \neq 0$. But this follows from the fact that the curve γ does not have self-intersections. □

2.3.2 Existence of Solutions to RCF

First notice that since a change of parameter in a curve does not alter its shape but only the speed we are travelling on the curve, we have infinitely many formulations representing the same curve evolution (although the function of the embedding, γ, may change). Secondly, since a curve in the plane is determined by its curvature, by means of the properties of the PDE associated to the curvature we can infer properties of the family of curves solving (2.3). We will derive equations for the curvature associated to the arc-length parameter, s, and the angle θ since they will be useful to prove existence of solutions and to describe their properties.

Equivalent formulations for RCF

Proposition 2.3.2 *The curvature of the solution to (2.3) parameterized by the angle θ satisfies:*

$$\kappa_T = g\kappa + \partial_{\theta\theta}(g\kappa) \qquad \text{with} \qquad \frac{dT}{d\tau} = \kappa^2$$

Proof. The change to the angular parameter induces a coordinate change in the domain of definition of the equation, $(u,t) \mapsto (\theta(u,t), \tau(t))$, given by the partial derivatives $\partial_u = \theta_u\partial_\theta$ and $\partial_t = \theta_t\partial_\theta + \tau_t\partial_\tau$. Now, following [32] and [33], we have that the angle, θ, and the curvature satisfy:

$$\theta_t(u,t) = \partial_s(g\kappa) \quad \textit{and} \quad \kappa_t(u,t) = g\kappa^3 + \partial_{ss}(g\kappa)$$

Since, without loss of generality we can take $\tau_t = 1$, differentiating with respect to the new time variable, we have that the curvature fulfills:

$$\kappa_\tau = -\theta_t\kappa_\theta + \kappa_t = -\kappa_\theta\partial_s(g\kappa) + g\kappa^3 + \partial_{ss}(g\kappa)$$

Using the relation between partial derivatives $\partial_s = \kappa\partial_\theta$, we get that:

$$\kappa_\tau = g\kappa^3 + \kappa^2\partial_{\theta\theta}(g\kappa)$$

Finally, consider a new time derivative, dT defined by $\frac{dT}{d\tau} = \kappa^2$ to obtain:

$$\kappa_T = \partial_T(\kappa(\theta, t(T))) = \kappa_t\frac{dt}{dT} = g\kappa + \partial_{\theta\theta}(g\kappa)$$

□

Proposition 2.3.3 *Let $\theta_0(s,t)$ be the angle between the tangent to the initial curve $\gamma_0(s,t)$ and a fixed axis. Then the problem given by (2.3) is equivalent to:*

$$\theta_\tau(s,\tau) = \partial_s(g\theta_s) + (\int_0^s g\theta_s^2 ds)\theta_s \tag{2.8}$$

with initial condition $\theta(s,0) = \theta_0(s)$ and periodic boundary conditions $\theta(0,\tau) = \theta(L,\tau)$

Proof. In the case of the arc-length parameter and also taking $\tau_t = 1$, the coordinate change ([32], [33]) in the domain of definition of the solutions to (2.3) is given by $\partial_u = ||\gamma_u||\partial_s$ and $\partial_t = -(\int_0^s g\theta_s^2 ds)\partial_s + \partial_\tau$. Therefore, we have that:

$$\theta_\tau(s,\tau) = \theta_t + (\int_0^s g\theta_s^2 ds)\theta_s = \partial_s(g\theta_s) + (\int_0^s g\theta_s^2 ds)\theta_s$$

where the last equality follows from the expression of θ_t ([32], [33]). This yields that angles of solutions to (2.3) satisfy (2.8). Conversely, for any solution to (2.8) the curves:

$$\gamma(s,t) = (\int_0^s \cos(\theta)d\tilde{s}, \int_0^s \sin(\theta)d\tilde{s})$$

are closed curves that satisfy an equation that, up to a change of parameter, equals (2.3). □

We will prove existence of solutions to RCF by showing that the equivalent problem given in Proposition 2.3.3 has a weak solution provided that θ_0 is $\mathcal{C}^2$. Under this assumption on the differentiability of the initial function we will construct a sequence of weak solutions to the associated linear problem:

$$\theta_\tau(s,\tau) = \partial_s(g(\psi)\theta_s) + (\int_0^s g(\psi)\psi_s^2 ds)\theta_s \tag{2.9}$$

uniformly bounded in H^1. Then, as the space is reflexive, it exists a subsequence that weakly converges to a function $\theta \in H^1$, which is a weak solution to 2.8.

Notice that since the roughness measure can cancel at some points, the differential operator is not elliptic at every point. We recall that this condition guarantees existence of weak solutions to (2.9) in the space $\mathcal{C}([0,T), H^1)$ by means of Galerkin's method. The key point lies on having a uniform bound on the first derivative that can

be obtained if one applies the elliptic condition to the integral version of the equation. Hence the lack of ellipticity forces to consider the partial differential equation that the first derivative, $\theta_s = \kappa$, satisfies in order to obtain a uniform bound for its L^2-norm. This forces the initial function, θ_0 to belong to H^1 and $\psi \in \mathcal{C}^1$.

We will begin with proving that the linear problem (2.9) has weak solutions. Next we will deduce that, in spite of the lack of ellipticity, these solutions are at least $\mathcal{C}^2$ almost everywhere, provided that the second derivative of the roughness measure, g_{ss}, stays bounded almost everywhere. Finally we will address existence of weak solutions to the non linear problem given in Proposition 2.3.3.

Existence of Solutions to the Linear Problem

We will show that the linear problem (2.9) has weak solutions by means of its approximations in certain finite dimensional spaces (Galerkin's method). Let $\{\omega^k(s)\}_k$ be a smooth periodic basis of H^1, orthonormal in L^2. We could take, for instance, the eigenfunctions of the Laplacian operator with a time dependent period, L, given by:

$$\frac{dL}{dt} = -g(\psi)\psi_s^2 L \Rightarrow L(t,s) = L_0(s)e^{-g(\psi)\psi_s^2 t}$$

which implies that the domain of integration (s,t) is not a rectangle, $[0,L_0]\times[0,T]$, but a trapezoid of basis L_0 at time 0 and $L(T)$ at time T.

The projection of equation (2.9) onto the finite dimensional spaces, Ω_m, spanned by $\{\omega^1,\ldots,\omega^m\}$ is given by:

$$\int_0^L \theta_t^m \omega = -\int_0^L g(\psi)\theta_s^m \omega_s + \int_0^L (\int_0^s g(\psi)\psi_s^2 ds)\theta_s^m \omega \tag{2.10}$$

for $\omega \in \Omega_m$ and initial condition the projection of ψ onto Ω_m, $\psi_m = \sum(\int \psi\omega_k)\omega_k$. We assert that the former equation has a unique weak solution, θ^m, of the form:

$$\theta^m = \sum_k d_m^k(t)\omega^k(s)$$

This follows from the fact that the coefficients, d_m^k, satisfy the system of ordinary differential equations obtained by requiring that the functions θ^m satisfy (2.10) for each of the generators, ω^k, $k = 1,\ldots,m$. We claim that θ^m are uniformly bounded in $L^2([0,T),H^1)$, provided that ψ is $\mathcal{C}^1$. Because the operator is not elliptic, we need first a bound on θ_s^m:

Lemma 2.3.1 *Let $\kappa_0(s)$ be a periodic function on $\mathbb{R}$. For each $\psi \in \mathcal{C}^1(I,\mathbb{R})$, consider the initial boundary problem:*

$$\kappa_t(s,t) = g(\psi)\psi_s^2\kappa + \partial_{ss}(g(\psi)\kappa) + (\int_0^s g(\psi)\psi_s^2 ds)\kappa_s \tag{2.11}$$

with $\kappa(s,0) = \kappa_0$. If $\kappa \in H^1$ is a weak solution and g_{ss} is uniformly bounded by M, then the solution is unique and satisfies:

$$\max_{0<t<T} ||\kappa||_{L^2}^2 \leq e^{T(||\psi_s^2||_\infty + M)}||\kappa_0||_{L^2}^2$$

where $||\psi_s||_\infty = \max_s |\psi_s|^2$.

Proof. Let $\kappa \in H^1$ be a weak solution of the initial boundary problem (2.11), that is, a function satisfying the integral equation:

$$\int \kappa_t \omega = \int g(\psi)\psi_s^2 \kappa\omega + \int (\int_0^s g(\psi)\psi_s^2 ds)\kappa_s\omega - \int \partial_s(g(\psi)\kappa)\omega_s$$

for all $\omega \in H^1$. Denote by η the square of the L^2-norm of κ. If $\kappa_s \neq 0$ almost every where, then η fulfills:

$$\eta_t = \int \kappa_t\kappa = \int g(\psi)\psi_s^2\kappa^2 + \int (\int_0^s g(\psi)\psi_s^2 ds)\kappa_s\kappa - \int \partial_s(g(\psi)\kappa)\kappa_s = \int g(\psi)\psi_s^2\kappa^2 +$$
$$+ \frac{1}{2}\int (\int_0^s g(\psi)\psi_s^2 ds)\partial_s(\kappa^2) - \int g(\psi)\kappa_s^2 - \int g_s(\psi)\partial_s(\kappa^2) \leq -\int g_s(\psi)\partial_s(\kappa^2) +$$
$$= \frac{1}{2}\int \psi_s^2\kappa^2$$

The last inequality obtained through integration by parts of $\int(\int_0^s g(\psi)\psi_s^2 ds)\partial_s(\kappa^2)$. Integrating once again by parts, we get that:

$$\eta_t \leq \int (g_{ss} + \psi_s^2)\kappa^2 \leq (M + ||\psi_s^2||_\infty)\eta$$

For M a bound on g_{ss}. Finally Gronwall's Lemma yields that:

$$||\kappa||_{L^2}^2 \leq e^{t(M+||\psi_s^2||_\infty)}||\kappa_0||_{L^2}^2$$

On one hand, since the PDE is linear, this inequality implies uniqueness of the solutions. On the other hand, taking maximums over time we obtain the bound on $||\kappa||_{L^2}^2$. In the case $\kappa_s \equiv 0$, the equation for the L^2-norm yields:

$$\eta_t = \int g(\psi)\psi_s^2\kappa^2 \leq ||\psi_s^2||_\infty \eta$$

Thus, in this case we also have:

$$||\kappa||_{L^2}^2 \leq e^{t||\psi_s^2||_\infty}||\kappa_0||_{L^2}^2$$

Splitting the domain of integration into the set $\{\kappa_s \equiv 0\}$ and its complementary, we get the result in the general case. □

The above bound on the solutions to the equation associated to the first derivatives of a function solving (2.9) and standard arguments on linear PDE's gives existence to the linear problem:

Proposition 2.3.4 *Let $\psi \in \mathcal{C}^1$ be a function such that g_{ss} is uniformly bounded almost everywhere. Then it exists a unique weak solution to:*

$$\theta_\tau(s,\tau) = \partial_s(g(\psi)\theta_s) + (\int_0^s g(\psi)\psi_s^2 ds)\theta_s$$

with initial condition $\theta(s,0) = \theta_0$ a periodic function in the Sobolev space H^1 . Besides we have the following bound on the L^2 norm of the solutions:

$$max_{0\leq t<T}||\theta||_{L^2} \leq ||\theta_0||_{L^2}$$

Proof. See [24]. □

Existence of Solutions to RCF

We recall that we will prove existence by means of a suitable sequence of weak solutions to the linear problem (2.9). Since the operator is not everywhere elliptic, we need solutions to (2.9) to be, at least $\mathcal{C}^2$, in order to explicitly derive a bound on $\theta_s = \kappa$.

Proposition 2.3.5 *Let ψ, θ_0 be $\mathcal{C}^2$ functions. Then the weak solution to :*

$$\theta_t = \partial_s(g(\psi)\theta_s) + (\int_0^s g(\psi)\psi_s^2 ds)\theta_s$$

with initial condition $\theta(s,0) = \theta_0$ is $\mathcal{C}^2$ as well.

Proof.

If $g > \epsilon$ almost everywhere, we can assure that the solutions belong at least to H^4, since the coefficients of (2.9) belong to $\mathcal{C}^2$, the initial function is $\mathcal{C}^2$ and the second order operator is of elliptic type. Hence, on that set, by virtue of Morrey's inequality, we have that θ is $\mathcal{C}^3$. We may only have problems in a neighborhood of those points where g is continuous and cancels, as the equation resembles a transport one (i.e. a 1st order PDE):

$$\theta_t = g_s(\psi)\theta_s \tag{2.12}$$

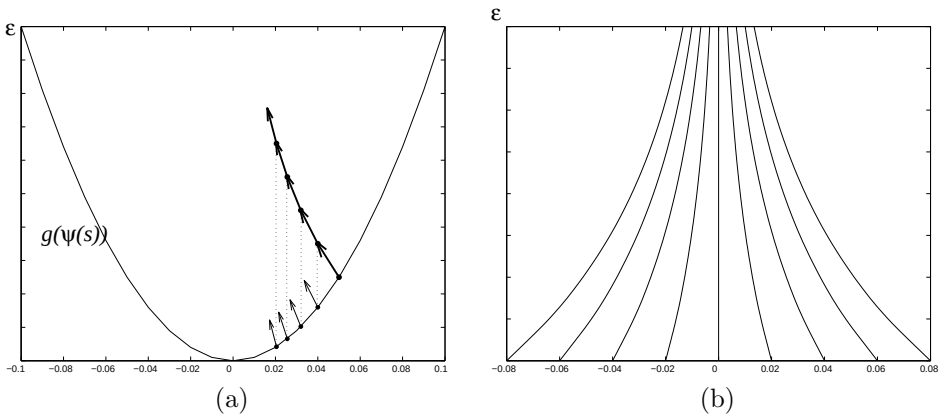

Figure 2.3: Behavior at a point of cancelling g, (a), and level lines of θ, (b)

By general theory of first order PDE's, we know that solutions, whatever the differentiability of the initial function, may develop singularities (shocks) either if

the equation is non linear or if its coefficients are not $\mathcal{C}^\infty$. Our equation fits into the second group as we can only assure that g_s is continuous. We recall that shock formation is essentially due to crossing of two characteristics, that is, when two level curves of the function solving (2.12) cross. If we show characteristics do not cross for any positive time, then we can assure that the function will be as smooth as the initial function θ_0. The key point lies on noticing that the function g is as smooth as ψ. Since $g = 0$ is a minimum and ψ is $\mathcal{C}^2$, we have that the graph of g, locally, is like the one shown in figure 2.3(a). Now, the characteristics of equation (2.12) are given by $\alpha(t) = (s(t), t)$ with $s_t = -g_s(\psi)$, that is, they correspond to the flux given by the normal vector to the graph $(s, g(\psi(s)))$, as it illustrates figure 2.3(a). Hence they correspond to the flux drawn in figure 2.3(b). The real equation can be viewed as a perturbation of (2.12), which not only does not alter the flux of figure 2.3(b) but also adds the regularizing effect of the diffusion $g\theta_{ss}$. This proves the statement. □

Differentiability of solutions to (2.9), yields that their first derivative satisfies:

Proposition 2.3.6 *Let θ be a solution to the linear problem (2.9), with initial condition a $\mathcal{C}^2$ periodic function. Then the L^2 norm of its first derivative κ is bounded by:*

$$\max_{0\leq t<T} ||\kappa(t)||_{L^2} \leq e^T ||\kappa(0)||_{L^2}$$

where $\kappa_0 = \partial(\theta_0)/\partial_s$

Proof. We remit the reader to Proposition 2.3.8 for the idea of the proof and to [24] for the details. □

Equipped with the above results, we are ready to prove the main result of this section:

Theorem 2.3.2 *For any $\mathcal{C}^2$ periodic function $\theta_0(s)$, there exists a unique periodic weak solution to:*

$$\theta_\tau(s,\tau) = \partial_s(g\theta_s) + (\int_0^s g\theta_s^2 ds)\theta_s \qquad \text{with} \qquad \theta(s,0) = \theta_0(s)$$

Proof. Let $X = \mathcal{C}([0,T], H^1(I,\mathbb{R}))$ be the space of continuous functions from $[0,T]$ to the Sobolev space of periodic real functions with first derivatives square integrable. Each function, $\psi \in X$, defines the linear parabolic PDE:

$$\theta_t(s,t) = \partial_s(a(s,t)\theta_s) + b(s,t)\theta_s \quad \text{with initial condition} \quad \theta(s,0) = \theta_0(s)$$

with $b(s,t) := (\int_0^s g(\psi)\psi_s^2 ds)$ and $a(s,t) := g(\psi)$. By Proposition 2.3.4, we know that, at least, a $\mathcal{C}^2$ solution satisfying the maximum principle exists. Furthermore, by virtue of the equation associated to its first derivative, $\theta_s = \kappa$, we have that

$$\max_{0<t<T} ||\kappa||_{L^2} \leq e^T \max ||\kappa_0|| \tag{2.13}$$

Consider the sequence in H^1 defined as:

$$\theta^1 := A(\theta_0) \;\; ; \quad \theta^k := A(\theta^{k-1}) \quad k > 1$$

We claim that the sequences θ^k and θ^k_t are bounded in $L^2([0,T], H^1(I,\mathbb{R}))$ and $L^2([0,T], H(I,\mathbb{R})^{-1})$, respectively, where $H(I,\mathbb{R})^{-1}$ denotes the topological dual space of $H^1(I,\mathbb{R})$. Then, since the spaces are reflexive, there exists subsequences, θ^{k_m} and $\theta^{k_m}_t$ and a function $\theta \in L^2([0,T], H^1(I,\mathbb{R}))$, with $\theta_t \in L^2([0,T], H(I,\mathbb{R})^{-1})$ such that:

$$\theta^{k_m} \rightharpoonup \theta \text{ weakly } L^2([0,T], H^1(I,\mathbb{R})) \text{ and } \theta^{k_m}_t \rightharpoonup \theta_t \text{ weakly } L^2([0,T], H^1(I,\mathbb{R})^*)$$

This function θ is a weak solution [23] (by virtue of Lipschitzity of g) to the initial boundary problem of Proposition 2.3.3 and produces a piece wise smooth curve that solves equation (2.3).

The maximum principle for solutions to (2.8) and the inequality (2.13), gives a bound for $||\theta^k||^2_{L^2([0,T],H^1(I,\mathbb{R}))}$. For a bound on θ^k_t in H^{-1}, consider, for each $\omega \in H^1$, the following:

$$\begin{aligned} |\int \theta^k_t \omega| = |-\int a(s,t)\theta_s\omega_s + \int b(s,t)\theta_s\omega| \leq ||\theta_s||_{L^2}||\omega_s||_{L^2} + C||\theta_s||_{L^2}||\omega||_{L^2} \leq \\ \leq (e^T||\kappa_0||_{L^2} + C||\kappa_0||_{L^2})||\omega||_{H^1} \end{aligned}$$

Where we have applied Holder to obtain the first inequality. It follows that $||\theta^k_t)||_{H^{-1}} \leq e^T||\kappa_0||_{L^2} + C||\kappa_0||_{L^2}$. Weakly convergence for bounded sequences in reflexive spaces yields existence of weak solutions for finite time. □

2.3.3 Differentiability and Uniqueness

Differentiability

Let us see that the weak solutions to (2.8) are as smooth as the initial function θ_0. This fact will ensure uniqueness of solutions if θ_0 is $\mathcal{C}^2$. Notice how lack of ellipticity forces a certain degree of differentiability in the initial condition in order to guarantee existence and uniqueness of weak solutions.

Proposition 2.3.7 *Consider the initial boundary problem:*

$$\theta_t = \partial_s(g(\theta)\theta_s) + \left(\int g(\theta)\theta_s^2\right)\theta_s$$

with initial condition a periodic $\mathcal{C}^k$ function θ_0 and periodic boundary conditions. Then any weak solution $\theta \in H^1$ is $\mathcal{C}^k$ as well.

Proof. As in the case of differentiability of the solutions to the linear problem (Proposition 2.3.5), we must only bother in a neighborhood of those points that cancel g. In the open set where $g > \epsilon$, as the operator is elliptic, we have that the solutions are $\mathcal{C}^n$ for $t > t_n$, thus improving the differentiability of the original function.

We will follow the arguments given in Proposition 2.3.5 and show that the characteristic lines of the non-linear transport equation:

$$\theta_t = g_s(\theta)\theta_s$$

are smooth and well defined (that is, curves of different levels do not cross). The level lines, $\alpha(t)$, are given by the normal vector to the graph of g: $(-g_s(\theta(s,t)),1)$. The only difference with respect to the linear case is that the roughness measure depends on time. We will see that for small times, $t < \delta$, the flux is well defined. For larger times just apply the same argument to the problem with initial condition $\theta(s, t-\delta)$.

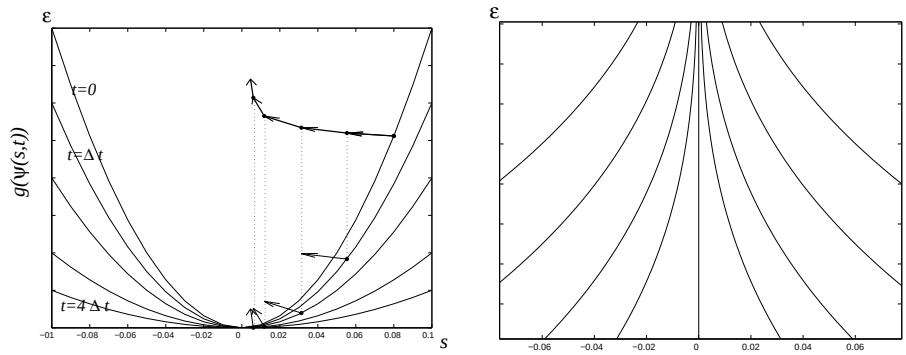

Figure 2.4: Flux given by the normal vector when g decreases and level lines when g

Since by assumption the initial function is $\mathcal{C}^2$, in a small enough neighborhood of a point cancelling the roughness measure, the graph of g at time zero is like a parabola. Now, by continuity of g with respect to time, for times $t < \delta$, g either increases or decreases uniformly in a neighborhood of the zero of $g(s,0)$. If g increases uniformly, we are in the situation of figure 2.4 and the level curves (shown in figure **??**) are as in Proposition 2.3.5. In the case of an increasing g, the second order term of the equation increases its weight with time. Since it is bounded by its value for time zero, $g(s_0,0)$, we are diffusing the function along the curves given by $(-g_s(\theta(s,t)),1)$. Thus we are adding some curvature to the level curves of the solutions producing a well defined flux as well. In fact, as $g \to 0$ over the solutions to RCF (Theorem 2.3.4 in Section 2.3.4), this last situation never occurs. □

Uniqueness

In order to show uniqueness we will consider the curve in cartesian coordinates and require that points move to fix their x-coordinate, that is, locally, $\gamma = \gamma(x) = (x, y(x))$. Using this parameterization, the flow is given [32] by:

$$y_t = \frac{g y_{xx}}{1 + y_x^2}$$

where $g = g(\arctan(y_x))$. We will see that if the functions solving (2.8) are $\mathcal{C}^2$, then the solution to the above equation is unique. Since we can cover the curve with a finite number of cartesian maps, we obtain uniqueness for the RCF.

Theorem 2.3.3 *It exists a unique $\mathcal{C}^2$ solution to the PDE:*

$$y_t = \frac{g y_{xx}}{1+y_x^2} = g\partial_x(\arctan(y_x)) \tag{2.14}$$

Proof. Gronwall's Lemma applied to the L^2-norm of the difference of two solutions yields the result. We remit the reader to [24] for the computational details. □

Since the initial function must be $\mathcal{C}^2$ in order to guarantee existence and uniqueness of solutions, solutions to (2.8) are at least $\mathcal{C}^2$. This fact gives sense to the maximum principles and energy bounds for the curvature that we will derive in next section.

2.3.4 Properties of RCF

We devote this part to the analysis of the solutions to the RCF. Firstly, we will show that the RCF has the same shape simplification properties as the MCF. Secondly, we will prove the main advantage of RCF over MCF: convergence of the orbits to a non trivial $\mathcal{C}^\infty$ curve that keeps significant inflexion points of the initial curve. This facts makes our flow suitable for shape recognition analysis and image filtering. We will begin with some bounds on the solutions to RCF and, then, analyze RCF asymptotic properties.

Energy Bounds

Proposition 2.3.8 *Let $\gamma(u,t)$ be a family of curves solving (2.3), for $(u,t) \in [0,1]\times[0,T)$. Then the energy of the curvature $||\kappa(t)||_{L^2} := \int_0^1 \kappa^2\sqrt{\dot{x}^2+\ddot{y}^2}du = \int_0^1 \kappa^2 \nu du$ is a decreasing function of time,*

$$||\kappa(t)||_{L^2} \leq ||\kappa(0)||_{L^2}$$

Proof. We will see that the inequality is fulfilled between two consecutive inflexion points, θ_i, θ_{i+1}. Since κ belongs to the Sobolev space $H_0^1(\mathbb{R})$ of functions with compact supports with first derivatives in L^2, it can be expressed as $\kappa = \sum d_n(t)\omega_n$, where the functions ω_n are the eigenvectors of the Laplacian operator $-\Delta$ and we may assume they are positive. We will prove that the coefficients $d_n(t) = \int_{\theta_i}^{\theta_{i+1}} \omega_n\kappa$ decrease in time. Let η denote d_n for an arbitrary n. If we differentiate with respect to time and integrate by parts, as $\kappa = 0$ at θ_i, θ_{i+1}, by Proposition 2.3.2, we obtain:

$$\eta_t = \int_{\theta_i}^{\theta_{i+1}} \omega_n \partial_{\theta\theta}(g\kappa)d\theta + \int_{\theta_i}^{\theta_{i+1}} \omega_n g\kappa d\theta$$

If $\partial_{\theta\theta}(g\kappa) \neq 0$, integrating again by parts the first integral we get

$$\eta_t = \int_{\theta_i}^{\theta_{i+1}} \partial_{\theta\theta}(\omega_n)(g\kappa)d\theta + \int_{\theta_i}^{\theta_{i+1}} \omega_n g\kappa d\theta = (1-\lambda_n)\int_{\theta_i}^{\theta_{i+1}} \omega_n g\kappa d\theta$$

where $\lambda_n = (n\pi)^2$ are the eigenvalues of the Laplacian operator $-\Delta$. Since $(1-\lambda_n) < 0$ and $\omega_n g\kappa$ is positive, if $\kappa > 0$, and negative otherwise, we have that $\eta_t < 0$ when

$\kappa > 0$ and $\eta_t > 0$ when $\kappa < 0$. This fact implies that $|\eta(t)|$ decreases in time, which proves the result if $\partial_{\theta\theta}(g\kappa) \neq 0$.

In the case that $\partial_{\theta\theta}(g\kappa) \equiv 0$ we are going to show that either the arc remains steady or we have a circle. In any case, since circles are steady curves we have that $\eta(t) \equiv \eta(0)$. The fact that $\partial_{\theta\theta}(g\kappa) \equiv 0$ implies that $\partial_\theta(g\kappa) = f(t)$. Now, since at the boundary points, we have that $g\kappa(t, \theta_i) = g\kappa(t, \theta_{i+1}) = 0$, there exists an interior extremum, that is the first derivative $\partial_\theta(g\kappa)$ cancels at some point. This implies that, indeed, $\partial_\theta(g\kappa) \equiv 0$ on the whole arc, hence we have that is $g\kappa$ is constant and equal to zero, by virtue of the cancellation of κ at the boundary points. So let us assume that we have a convex curve and check that it necessarily must be a circle. Since in this case $\theta_i = \theta_{i+1}$ the first derivative $\partial_\theta(g\kappa)$ must cancel in the whole curve. Developing the derivative, we obtain that $\frac{-g_\theta}{g} = \frac{\kappa_\theta}{\kappa}$. Integrating this equation, we can write the curvature in the form $\kappa = F(t)e^{1/g}$. Substituting this expression in the PDE for the curvature, we get:

$$\kappa_t = F' e^{\frac{1}{g}} - F\frac{g_t}{g^2} e^{\frac{1}{g}} = gFe^{\frac{1}{g}}$$

Now, because $\theta_t = \partial_s(g\kappa) = \kappa\partial_\theta(g\kappa)$, we have that the derivative with respect to time of the factors of the function A given by (2.1) cancel:

$$\partial_t(a_{12}) = G_\rho * (2\theta_t \cos(2\theta)) \quad \text{and} \quad \partial_t(a_{11} - a_{22}) = G_\rho * (2\theta_t \sin(2\theta)))$$

It follows that $g_t \sim \sin(0.5 * \arctan(A) - \theta)(A_t/(1 + A^2) - \theta_t) = 0$ and $F' e^{\frac{1}{g}} = gFe^{\frac{1}{g}}$. Hence F satisfies the differential equation $\frac{F'}{F} = g$. Finally, since g is independent of time, this last equality implies that, indeed, $g = C_1$ is constant. Thus $\kappa = F(t)e^{1/C_1}$ and the curve is a circle. □

Remarks:

1. It can be proved that the length, $L(t)$, of a curve satisfying (2.3) decreases in time at the rate $L_t = -\int g\kappa^2 \nu du$. It follows that the total curvature also decreases in time:

$$\overline{\kappa}(t) = \int |\kappa| \sqrt{\dot{x}^2 + \dot{y}^2} du \leq L(t)||\kappa(t)||_{L^2} \leq L(0)||\kappa(t)||_{L^2}$$

   which is one of the requirements for curve simplification.

2. The above Proposition ensures existence of weak solutions of the curvature equation for all time, hence we can assure that $\mathcal{C}^\infty$ piece-wise curves exist for all time.

Besides this bound on the L^2-energy of κ, we have that κ grows at most exponentially.

Lemma 2.3.2 *Let $\kappa(\theta, t)$, $t \in [0, T)$, be the solution to (**??**) with initial condition $\kappa_0(\theta)$ and assume that $g_{\theta\theta}$ is bounded by a constant M. Then, the following inequality holds:*

$$\max_{0<t<T} |\kappa(\theta, t)| \leq e^{T(M+1)} \max |\kappa_0|$$

Proof. The function $v = e^{-(M+1)t}\kappa$ fulfills the PDE:

$$v_t = -(M+1)v + e^{-(M+1)t}\kappa_t = -(M+1)v + gv + \partial_{\theta\theta}(gv)$$

If the function v had an interior extremum at the set where κ is positive, then:

$$0 = (g - (M+1) + g_{\theta\theta})v + g\partial_{\theta\theta}(v) \leq g\partial_{\theta\theta}(v)$$

Since $g \geq 0$, we get that the extremum is, indeed, a minimum. A similar argument at points with negative κ, yields that $|v(\theta,t)| \leq \max|v(\theta,0)| = \max|\kappa_0|$. We conclude that $|\kappa| \leq e^{(M+1)t}|v|$ and, thus, $\max_{0\leq t<T}|\kappa| \leq e^{(M+1)T}\max_{0\leq t<T}|v| = e^{(M+1)T}\max|\kappa_0|$. □

This maximum principle for the curvature yields that no new inflexion points are created.

Asymptotic Behavior

Proposition 2.3.9 *The number of inflexion points (i.e. zeros of the curvature) of a family of curves, $\gamma(u,t)$, satisfying (2.3) for $t \in [0,T)$ is a non-increasing function of time.*

Proof. We will prove that between two consecutive inflexion points the curvature does not change its sign. In an arc joining two consecutive inflexion points Lemma 2.3.2 holds and, so, we have that:

$$e^{T(M+1)}\min\kappa_0 \leq \kappa \leq e^{T(M+1)}\max\kappa_0$$

It follows that κ keeps the sign of κ_0 between consecutive inflexion points. □

The former Propositions yield that, as all geometric flow, RCF ensures shape simplification. What turns RCF into a preferable tool for image filtering and shape recovery tasks is the fact that solutions tend asymptotically to a $\mathcal{C}^\infty$ curve, which is the fixed point of equation (2.3) given by $g \equiv 0$. We can summarize this asymptotic behavior in the following results:

Proposition 2.3.10 *Steady states of (2.3) are simple closed curves.*

Proof. First notice that existence of a Lyapunov functional (the length functional, for instance) ensures that RCF has not periodic orbits. It follows that the limit of any orbit $\gamma(u,t)$ must be a steady point of equation (2.3). The inclusion principle [32] and stability of circles for RCF yield the statement as follows. Let C_1 be a circle containing γ_0 and C_2 a circle included in γ_0. By the inclusion principle, we have that evolutions of these curves under RCF fulfill $C_2(u,t) \subset \gamma(u,t) \subset C_1(u,t)$. The fact that any circle is a steady point yields the result. □

Before proceeding to the proof of the main property of RCF concerning convergence to zero of the roughness measure (Theorem 2.3.4), let us begin with some notations and considerations. The norm of the first derivative of a curve solving (2.3) will be noted by $\nu = \sqrt{\dot{x}^2 + \dot{y}^2}$. Following [32], [33] it is easy to check that ν solves:

$$\nu_t = -g\kappa^2\nu \qquad \text{with initial condition} \qquad \nu(u,0) = \nu^0(u) \tag{2.15}$$

since ν is a decreasing function of time, it is bounded above by ν^0. Furthermore, non triviality of steady states of curves following RCF (Proposition 2.3.10) yield that ν is also bounded from below by the minimum, $\nu_{min} > 0$, of the norms corresponding to the limit curve. Also by Proposition 2.3.10, we know that the orbits of (2.3) converge to a curve fulfilling $g\kappa \equiv 0$. Since the latter quantity is continuous (g is Lipschitz [24]) with respect the L^2-norm, it follows that:

$$\int g\kappa^2 = \int g\kappa \cdot \kappa \leq ||g\kappa||_{L^2}||\kappa||_{L^2} \leq ||g\kappa||_{L^2}||\kappa(s,0)||_{L^2} \overset{t\to\infty}{\longrightarrow} 0$$

We will note t_0 a time such that $\int g\kappa^2 < \epsilon$. The lower bound ν_{min} and the former asymptotic behavior will be used in the proof of Theorem 2.3.4. Let us begin with a preliminary Lemma:

Lemma 2.3.3 *The norm, ν, satisfies:*

$$\max_{t\leq T} |\partial_u(\nu^2)| \leq TM\nu^2(u,0) + \nu_u^2(u,0)$$

Proof. Recall that solutions to (2.3.3) are $\mathcal{C}^2$ classic solutions that converge to a smooth function θ_{lim} by existence of Lyapunov functionals. It follows that $\partial_u(g\kappa^2) \to \partial_u(g_{lim}\kappa_{lim}^2)$ and, hence, $\partial_u(g\kappa^2)$ is uniformly bounded by a constant $M/2$. Integrating (2.15) and noting $I = \int g\kappa^2 dt$, we get that $\nu = e^{-I}\nu(u,0)$, so that the first derivative:

$$|\partial_u(\nu^2)| = |-2\nu^2 \int \partial_u(g\kappa^2)dt| + |e^{-2I}\nu_u^2(u,0)| \leq Mt\nu^2(u,0) + \nu_u^2(u,0)$$

□

Theorem 2.3.4 *The roughness measure g tends to zero over the solutions to RCF.*

Proof. We recall that one of the definitions of the roughness measure is the square norm of the vector product:

$$g(\theta) = ||\overrightarrow{v}_1 \times \overrightarrow{n}||^2$$

where the vector $\overrightarrow{v}_1 = (\cos\psi, \sin\psi)$ is given by the quantity:

$$A := \tan 2\psi = \frac{2a_{12}}{a_{11} - a_{22}} = \frac{G_\rho * \sin(2\theta)}{G_\rho * \cos(2\theta)}$$

Therefore, by the above definition of A, g is close to zero in the measure that the vectors $\overrightarrow{v_1} = \tilde{T}_\rho = (G_\rho * \sin(2\theta), G_\rho * \cos(2\theta))$ and $T = (\sin(2\theta), \cos(2\theta))$ coincide. We will check that in the limit, when t goes to infinity, T converges to $\tilde{T}_\rho$. To such purpose we will study the asymptotic behavior of the PDE's that the former vectors follow.

For a given parameter u for a curve following (2.3), we have that T solves the PDE:

$$T_t(u,t) = \partial_s(gT_s(u,t)) = \frac{1}{\nu}\partial_u(g\frac{T_u}{\nu}) \text{ with } T(s,0) = T_0 \tag{2.16}$$

where $\nu = \sqrt{\dot{x}^2 + \dot{y}^2}$. On the other hand, $\tilde{T}_\rho$ corresponds to the solution at time $t = \rho$ of:

$$\tilde{T}_t = \tilde{T}_{uu} \text{ with } \tilde{T}(u,0) = T(u,t) \tag{2.17}$$

If we change to the arc length parameter of $\gamma(u,t)$, the above PDE's convert to:

$$T_t = \partial_s(gT_s) + \left(\int g\kappa^2\right) T_s \qquad \text{with } T(s,0) = T_0 \tag{2.18}$$

$$\tilde{T}_t = \nu\partial_s(\nu\tilde{T}_s) + \left(\int g\kappa^2\right) \tilde{T}_s \qquad \text{with } \tilde{T}(s,0) = T(s,t) \tag{2.19}$$

where $\nu = 1/u_s = \nu(s)$ denotes the derivative of the inverse change from parameter u to parameter s. First, notice that in (2.19) s does not need to correspond to the arc length of $\tilde{T}$. Second, the quantity $g\kappa^2$ is computed over the solution to RCF with the function g given by the parameter u. For a better handling of (2.19), we will develop the term of the second derivative and use the formulation:

$$\tilde{T}_t = \nu^2\tilde{T}_{ss} + \frac{1}{2}\partial_s(\nu^2)\tilde{T}_s + \left(\int g\kappa^2\right)\tilde{T}_s \tag{2.20}$$

Let t_0 be a time such that $\int g\kappa^2 < \epsilon$, and consider the solutions to (2.18), (2.20) with initial condition $T(s,t_0)$. Let $(T-\tilde{T})^2$ be the square of the norm of the difference vector and define $\eta(t)$ to be:

$$\eta(t) = \int (T-\tilde{T})^2 ds \text{ for times } t > t_0 \tag{2.21}$$

If we note $I_g = \int g\kappa^2$, differentiate (2.21) with respect to time and integrate by parts we get:

$$\eta_t = \int (\partial_s(gT_s) - \nu^2\partial_s(\tilde{T}_s))(T-\tilde{T}) + \int I_g(T_s - \tilde{T}_s)(T-\tilde{T}) - \frac{1}{2}\int \partial_s(\nu^2)\tilde{T}_s(T-\tilde{T}) =$$
$$= \int \partial_s(gT_s - \tilde{T}_s)(T-\tilde{T}) + \int (1-\nu^2)\tilde{T}_{ss}(T-\tilde{T}) + \frac{1}{2}\int I_g\partial_s((T-\tilde{T})^2) -$$
$$- \frac{1}{2}\int \partial_s(\nu^2)\tilde{T}_s(T-\tilde{T}) = -\int (gT_s - \tilde{T}_s)(T_s - \tilde{T}_s) - \int \partial_s(1-\nu^2)\tilde{T}_s(T-\tilde{T}) -$$
$$- \int (1-\nu^2)\tilde{T}_s(T_s - \tilde{T}_s) - \frac{1}{2}\int g\kappa^2(T-\tilde{T})^2 - \frac{1}{2}\int \partial_s(\nu^2)\tilde{T}_s(T-\tilde{T}) \leq -\int g(T_s - \tilde{T}_s)^2 -$$
$$- \int (g-1)\tilde{T}_s(T_s - \tilde{T}_s) - \int (1-\nu^2)\tilde{T}_s(T_s - \tilde{T}_s) + \frac{1}{2}\int \partial_s(\nu^2)\tilde{T}_s(T-\tilde{T}) \leq$$
$$\leq \int (\nu^2 - g)\tilde{T}_s(T_s - \tilde{T}_s) + \frac{1}{2}\int \partial_s(\nu^2)\tilde{T}_s(T-\tilde{T}) = -\int (\nu^2-g)\tilde{T}_s^2 +$$
$$+ \int (\nu^2 - g)\tilde{T}_s T_s + \frac{1}{2}\int \partial_s(\nu^2)\tilde{T}_s(T-\tilde{T}) \leq \int |\nu^2 - g|\tilde{T}_s^2 + \int (\nu^2-g)\tilde{T}_s T_s +$$
$$+ \frac{1}{2}\int \partial_s(\nu^2)\tilde{T}_s(T-\tilde{T}) \leq \int |\nu^2 - g|\tilde{T}_s^2 + \int (\nu^2-g)\tilde{T}_s T_s + \frac{1}{4}P_2(t)\int \tilde{T}_s^2 + \frac{1}{4}\eta$$

The last inequality follows from Cauchy's inequality combined with Lemma 2.3.3, provided that $P_2(t)$ denotes the polynomial of degree 2 given by the bound on $(\partial_s(\nu^2))^2 = (\partial_u(\nu^2)/\nu)^2$. Since s is the arc length, we have that $T_s = \kappa T^{\perp}$, where κ is the curvature of the underlying solution to RCF. Thus, by Proposition 2.3.8, its L^2-norm is bounded by $||T_s||^2_{L^2} = ||\kappa||^2_{L^2} \leq ||\kappa(s,0)||^2_{L^2} = ||\kappa_0||^2_{L^2}$. Applying Cauchy-Schwarz to $\int(\nu^2 - g)\tilde{T}_s T_s$, it follows that η_t fulfills:

$$\begin{aligned}\eta_t &\leq \int |\nu^2 - g|\tilde{T}_s^2 + ||(\nu^2 - g)\tilde{T}_s||_{L^2}||T_s||_{L^2} \leq \\ &\leq K||\tilde{T}_s||^2_{L^2} + K||\kappa_0||_{L^2}||\tilde{T}_s||_{L^2} + \frac{1}{4}P_2(t)||\tilde{T}_s||^2_{L^2} + \frac{1}{4}\eta\end{aligned}$$

where K is a bound on $(g - \nu^2)^2$. Further, because equation (2.19) is of elliptic type with initial condition $T(s,t_0)$ it can be shown [23] that:

$$\nu^2_{min} \max_t ||\tilde{T}_s||^2_{L^2} \leq \max_t ||g\kappa^2||^2_{L^1} \leq \epsilon^2$$

These considerations yield that $\eta_t \leq \epsilon(C_1||\kappa_0||^2_{L^2} + C_2\epsilon + C_3\epsilon P_2(t)) + C_4\eta$ for suitable constants $C_1 \ldots C_4$. Finally, applying Gronwalls's Lemma we obtain that η is bounded by:

$$\begin{aligned}\eta(t) &\leq e^{C_4 t}\left(\eta(0) + \epsilon\int_0^t C_1||\kappa_0||^2_{L^2} + C_2\epsilon + C_3\epsilon P_2(t)dt\right) \leq \\ &\leq \epsilon T(C_1||\kappa_0||^2_{L^2} + C_2\epsilon + C_3\epsilon P_2(T))e^{C_4 T}\end{aligned}$$

That is, it exists a time t_0 ensuring that solutions to (2.18) and (2.20) with initial condition $T(s,t_0)$ differ less than ϵ in L^2, for finite times $0 \leq t \leq T$. Finally, Proposition 2.3.10 ensures that solutions to (2.16) and (2.17) computed over the parameter u also converge to each other in the latter sense since:

$$\eta(s,t) = \int (T(s,t) - \tilde{T}(s,t))^2 ds = \int (T(u,t) - \tilde{T}(u,t))^2 \nu(u,t) du \geq \nu_{min}\eta(u,t)$$

This asymptotic behavior, yields the following:

$$||\tilde{T}_\rho - T||_{L^2} = ||\tilde{T}(\rho) - T(t)||_{L^2} \leq ||\tilde{T}(\rho) - T(\rho + t)||_{L^2} + ||T(\rho + t) - T(t)||_{L^2} \overset{t\to\infty}{\longrightarrow} 0$$

The first summand converges to zero because $T(\rho + t)$ is the solution to (2.18) for initial condition $T_0 = T(s,t)$ at time $t = \rho$. Hence, $||\tilde{T}(\rho) - T(\rho + t)||_{L^2} = \eta(\rho) \leq \epsilon$, if t is large enough. The second, because solutions to equation (2.18) are Cauchy, as they converge to a curve in time. □

2.3.5 Error in RCF Level Sets Formulation

Let us deduce the formula for the error in RCF level sets formulation given in Section 2.2.1. We recall the reader that the difference between the two dimensional structure tensor , $\tilde{J}$, and the exact value, J, computed along the level line was given in terms of

the curve curvature, κ_0, and the curvature, κ_{Im}, of the image gradient integral curves by the formula:

$$|J_\rho - \tilde{J}_\rho| \leq \epsilon \left(C \int |\kappa_0| + \int |\kappa_{Im}| \right) |\overrightarrow{t}_0 \otimes \overrightarrow{n}_0| + \mathcal{O}(\epsilon^2) \tag{2.22}$$

where ϵ is the size of the window used to compute 2D-convolutions. For the sake of notational simplicity the scale ρ will be dropped, the projection matrix onto a vector v will be noted by P_v and convolutions will be evaluated at the origin. In a level sets formulation, the parameterization of a curve is the implicit one. Since this coordinate change is local, formula (2.22) only holds for bounded domains of integration. We recall that this is the case in the discrete numeric implementation, so that there is no loss of generality in assuming that the x-coordinate is the parameter and $\gamma_0(x) = (x, y_0(x))$.

For each image point (x, y), denote by $(\bar{x}, y_0(\bar{x})) = (\bar{x}, \bar{y})$ the point achieving the distance, δ, from the image pixel to γ_0. Notice that it coincides with the pixel projection onto γ_0 along the normal direction $\overrightarrow{n}_0(\bar{x})$. The Taylor development of P_n at $(\bar{x}, \bar{y})$ yields that:

$$\begin{aligned} P_n(x,y) &= P_n(\bar{x},\bar{y}) + \langle \nabla P_n, (x-\bar{x}, y-\bar{y}) \rangle + \mathcal{O}(\delta^2) = P_n(\bar{x},\bar{y}) + \delta \langle \nabla P_n, n_0(\bar{x}) \rangle + \\ &+ \mathcal{O}(\delta^2) = P_n(\bar{x},\bar{y}) + \delta(\partial_{n_0} P_n)_{|_{x=\bar{x}}} + \mathcal{O}(\delta^2) \end{aligned} \tag{2.23}$$

Trigonometric arguments (see fig.2.5 (b) for a graphical representation) yield that:

$$|\bar{x} - x| = \delta \sin(\theta(\bar{x})) \quad \Rightarrow \quad \bar{x} = x \pm \delta \sin(\theta(\bar{x}))$$

Using the Taylor development of $\sin(\theta(\bar{x}))$ and $\cos(\theta(\bar{x}))$ it follows that:

$$\bar{x} = x + \delta[\sin(\theta(x)) + \cos(\theta(x))\theta_x(x)(x - \bar{x}) + \mathcal{O}((x-\bar{x})^2]$$

Further, since $|x - \bar{x}| = \delta \sin(\theta(\bar{x})) = \mathcal{O}(\delta)$, we conclude that the change of coordinates $\bar{x}$ is given by:

$$\bar{x} = x + \delta \sin(\theta(x)) + \mathcal{O}(\delta^2) = x + \delta \sin(\theta) + \mathcal{O}(\delta^2)$$

This bounds the first summand of (2.23) as:

$$P_n(\bar{x},\bar{y}) = P_{n_0}(\bar{x}) = P_{n_0}(x + \delta \sin(\theta) + \mathcal{O}(\delta^2)) = P_{n_0}(x) + \delta \sin(\theta) \partial_x(P_{n_0}) + \mathcal{O}(\delta^2) \tag{2.24}$$

Taking into account that in an implicit parameterization the norm of the curve first derivative equals $|\gamma_0'|^2 = 1 + (y_0')^2 = 1/\cos(\theta)^2$, we have that the partial with respect to the arc length, s, is given by:

$$\partial_s = \cos(\theta)\partial_x$$

Then by the Frenet formulae, it follows that the first derivative in equation (2.24) equals:

$$\sin(\theta)\partial_x(P_{n_0}) = \tan(\theta)\partial_s(P_{n_0}) = \tan(\theta)\partial_s(\overrightarrow{n}_0 \otimes \overrightarrow{n}_0) = -\kappa_0 \tan(\theta)(\overrightarrow{t}_0 \otimes \overrightarrow{n}_0)$$

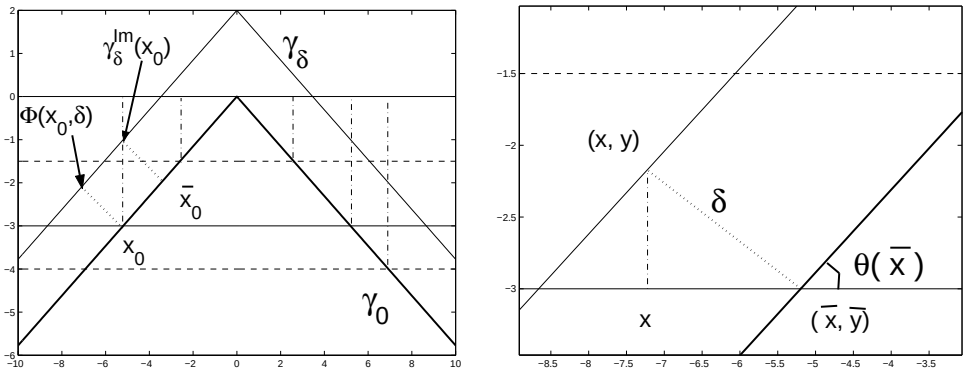

(a) (b)

Figure 2.5: Tube parameterization versus implicit (a) and coordinate change (b).

For the second term of (2.23), because ∂_n corresponds to the unit tangent of the flow lines, again the Frenet yield:

$$(\partial_{n_0} P_n)_{|_{x=\bar{x}}} = (\partial_n P_n)_{|_{x=\bar{x}}} = \partial_n (n \otimes n)_{|_{x=\bar{x}}} = \kappa_{Im}(\bar{x})(t_0 \otimes n_0) = \kappa_{Im}(x)(t_0 \otimes n_0) + \mathcal{O}(\delta) \tag{2.25}$$

where κ_{Im} stands for the flow lines curvature. Blending together (2.24) and (2.25), we conclude that the tensor $\tilde{J}$ computed with a 2-D gaussian kernel G defined in a window of size ϵ equals:

$$\begin{aligned}
\tilde{J} &= \int_{-\epsilon}^{\epsilon}\int_{-\epsilon}^{\epsilon} G(x,y) P_n(x,y) = \int\int G(x,y) P_{n_0}(x) dxdy + \\
&+ \delta \int\int G(x,y)\kappa_{Im}(x)(t_0(x) \otimes n_0(x))dxdy - \kappa_0(x)\tan(\theta(x))(t_0(x) \otimes n_0(x))dxdy + \\
&+ \mathcal{O}(\delta^2) = J + \delta \int_{-\epsilon}^{\epsilon} G(x)(\kappa_{Im} - \kappa_0 \tan(\theta))(t_0 \otimes n_0)dx + \mathcal{O}(\epsilon^2)
\end{aligned}$$

which proves the formula for the error because:

$$\begin{aligned}
|\tilde{J} - J| &\leq \epsilon \int (|\kappa_{Im}| + |\kappa_0 \tan(\theta)|)||t_0 \otimes n_0|| + \mathcal{O}(\epsilon^2) = \\
&= \epsilon ||t_0 \otimes n_0|| \left(\int |\kappa_{Im}| + C \int |\kappa_0| \right) + \mathcal{O}(\epsilon^2)
\end{aligned}$$

provided that the angle of the unit tangent, θ does not turn around more than π in a neighborhood of each point in the target curve, so that we can ensure that $|\tan(\theta)|$ is bounded by a constant C.

. . . . . .

In this chapter, we have defined a novel geometric flow which is well suited for image filtering and shape recovery tasks. The latter are the usual applications of geometric flows. Still, because they model shape propagation/deformation, geometric flows and, in particular, curvature based ones can be used in image segmentation and shape modelling. In the next section we will use the mean curvature flow to design a new external energy for snakes that ensures their convergence, independently of the particular geometric features (concavity) of the contour to be approached.

Chapter 3

Curvature Vector Flow. Heading towards an efficient Shape Modeling

Shape modelling arises in many fields of computer vision and graphics [35], [31], [82], to mention just a few. The most efficient way of producing smooth models of shapes is by means of a snake [38], [11], [12]. Snakes are curves that minimize an energy functional by means of its gradient descent. The definition of the external energy characterizing the target object is crucial for a successful model of the shape. In spite of the improvement of the external energy given by the gradient vector flow technique [75] or [16] area minimizing balloon forces, highly non convex shapes can not be obtained, yet.

A study of distance maps from a geometric point of view clearly shows the limitations of the current external forces. Standard tools of calculus of variations link convergence to the minimum of the external potential to differentiability of its level sets. A back-tracking of the evolution of the contour of level zero by minimum curvature flow [49] is the natural geometric way of converging to non-convex regions. Since the PDE associated to this evolution is of elliptic type, we can assure that propagation of non convex regions will not develop shocks during the process. In this manner we build a distance map having the contour of level zero as unique local minimum. The gradient of the map, called Curvature Vector Flow, is capable of attracting any initial interior or exterior curve towards the contour of interest, independently of its geometric features.

3.1 Snake Convergence and Smoothness of the External Energy

A common feature to all existent snake techniques is that they deform until a minimum of an energy functional is achieved. Since cancellation of the first variation of this functional (Euler-Lagrange equation) is the criterion used to characterize local minima, snakes are ruled by calculus of variations principles. In this section we will use standard results of variational techniques to establish conditions on the external

energy that prevent snakes reaching concave regions. Such conditions are in terms of the convexity/ellipticity [23] of the functional second variation. Further, we will relate, in the case of parametric snakes, the former analytical requirements to the geometry of the external energy level sets. This will provide us with a criterion in terms of existence of singular points of the level curves easier to verify than the convexity condition.

3.1.1 Convexity and Smoothness of Level Sets

Before giving the main result of the section concerning convexity, let us establish what snake functionals ensure convexity exclusively by means of the external energy term. We must treat separately the case of parametric and geodesic snakes.

We recall the reader that the functional associated to a parametric snake [38], γ, splits energy into the following two terms:

$$E(\gamma,\dot{\gamma},\ddot{\gamma}) = E_{int} + E_{ext} = E_1 + E_2 + E_{ext} = \int_\gamma \alpha||\dot{\gamma}||^2 + \int_\gamma \beta||\ddot{\gamma}||^2 + E_{ext} =$$
$$= \int_\gamma \alpha||\dot{\gamma}||^2 + \int_\gamma \beta||\ddot{\gamma}||^2 + \int_\gamma F(\gamma))du = \int L^1(\dot{\gamma})du + \int L^2(\dot{\gamma})du + \int_\gamma F(\gamma)) =$$
$$= \int L^1(p)du + \int L^2(P)du + \int F(z)du$$

where the potential $F = F(x, y)$ is positive, depends on the object to be detected and, in the ideal case, should cancel on curves segmenting the target objects. Our first remark is that convexity of this functional relies exclusively on the external energy convexity. This fact follows from the convexity of the snake internal energy:

$$E_1^{''}(q,q) = \int q^t L^1_{pp} q du = \int q^t \begin{pmatrix} 2 & 0 \\ 0 & 2 \end{pmatrix} q du$$

$$E_2^{''}(Q,Q) = \int Q^t L^2_{PP} Q du = \int Q^t \begin{pmatrix} 2 & 0 \\ 0 & 2 \end{pmatrix} Q du$$

Therefore convexity of E is ensured provided that for any curve ν the following inequality holds:

$$E^{''}_{ext}(\nu,\nu) = \int \nu^t F_{zz} \nu du \geq 0$$

That is, the snake energy is convex if and only if the Hessian of the potential F is positive defined. This situation significantly differs from the convexity conditions of the functional guiding geodesic snakes. In this case, the functional to be minimized [11], [12] fuses the external potential F and the length minimizing term, L^1:

$$E_{geod}(\gamma) = \int F(\gamma)\sqrt{\dot{x}^2 + \dot{y}^2} du = \int F(\gamma)||\dot{\gamma}||du = \int F L^1 du$$

This fact difficulties studying convexity of E_{geod} by means of the convexity of each of the factors, since its first variation is:

$$E'_{geod} = \int \langle F_z, \nu\rangle \cdot L^1 du + \int F \cdot \langle L^1_p, \dot{\nu}\rangle du$$

and, differentiating the above expression, its second equals:

$$E^{''}(\nu,\nu) = \int \left(\dot{\nu}^t F_{pp}\dot{\nu}\right) L^1 du + \int \left(\nu^t L^1_{zz}\nu\right) F du + 2\int \langle F_z,\nu\rangle\langle L^1_p,\dot{\nu}\rangle du$$

Hence even in the case that both F and L_1 were convex, this will not suffice to guarantee convexity of E_{geod} as the second variation involves F and L^1 first derivatives. This constitutes a main inconvenience and motivates using the classic parametric snakes formulation and search for a computational robust way of detecting non-convex external potentials.

Convexity is a property not easy to detect analytically in a robust way as it requires precise high (second) order derivatives. In this Section we give a simple convexity criterion in terms of the geometry of the external energy level sets. Notice that because we are interested in avoiding false minima its suffices to guarantee that F is convex at all points in the image such that $\nabla F = 0$, that is, that there are not saddle points.

Theorem 3.1.1 *A function $F(x,y)$ has no saddle points such that $\nabla F = 0$ if and only if F level sets are smooth curves.*

Proof. Let us assume that there exists a point p such that $\nabla F(p) = 0$ and the Hessian:

$$HessF(p) = \begin{pmatrix} F_{xx} & F_{xy} \\ F_{xy} & F_{yy} \end{pmatrix}_p$$

is not positive defined. We will prove that this holds if and only if the level curve through p, namely γ, is singular at the point p. Via a translation we can take $p = (0,0)$ and $F(0,0) = 0$. Under the latter assumptions, we have that any function E can be written as:

$$\begin{aligned} E(x,y) = \int_0^1 \frac{dE(tx,ty)}{dt} dt = x\int_0^1 E_x(tx,ty)dt + y\int_0^1 E_y(tx,ty)dt = \\ = xf(x,y) + yg(x,y) \end{aligned}$$

Applying the above decomposition to the external energy F, we have that:

$$\begin{aligned} F(x,y) =& x^2\int_0^1 F_{xx}(tx,ty)dt + 2xy\int_0^1 F_{xy}(tx,ty)dt + y^2\int_0^1 F_{yy}(tx,ty)dt = \\ &= a(x,y)x^2 + 2b(x,y)xy + c(x,y)y^2 \end{aligned} \tag{3.1}$$

Furthermore, by differentiating the above equality with respect to (x,y), we have that $a(0,0) = E_{xx}(0,0)$, $2b(0,0) = E_{xy}(0,0)$ and $c(0,0) = E_{yy}(0,0)$. The origin $p = (0,0)$ is a saddle point, if and only if the determinant $E_{xx}(0,0) * E_{yy}(0,0) - E^2_{xy}(0,0) = ac - 4b^2$ is negative, which implies that the curve given by:

$$0 = a(x,y)x^2 + 2b(x,y)xy + c(x,y)y^2 \tag{3.2}$$

is singular at the origin in the algebraic sense (i.e. there are more than one tangent lines). This follows because if $y = \lambda x$ is a line through the origin, then the polynomial in λ:

$$0 = a(x,y)x^2 + 2b(x,y)\lambda x + c(x,y)\lambda^2 x^2 = x^2(a(x,y) + 2b(x,y)\lambda + c(x,y)\lambda^2)$$

has real roots for $(x, y) = (0, 0)$. This values of λ correspond to the slopes of a line that cuts the curve given by (3.2) at the origin with contact order at least two. This proves the result since the curve of level zero of F is given by equation (3.2). □

In figure 3.1 we have an illustrative example of the above theorem. The level set (fig.3.1 (a)) through the saddle point inside the red square of fig.3.1 (a) presents a singularity located at the latter, meanwhile the remaining level curves are smooth.

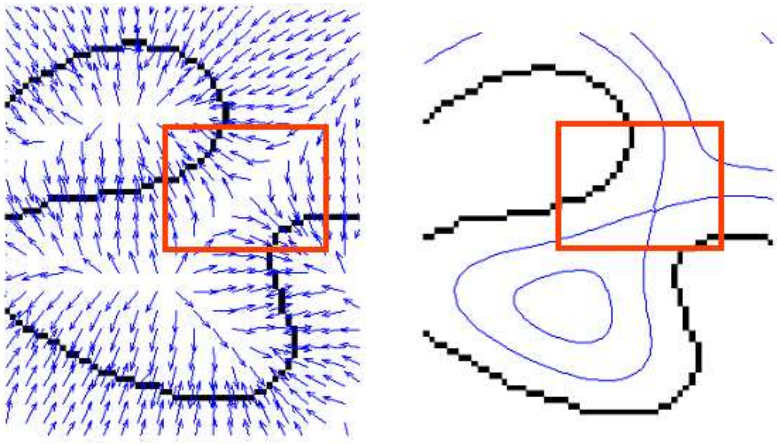

(a) (b)

Figure 3.1: Inflexion point (a) and Singular Curve (b)

The above theorem is a valuable tool to analyze whether an external force guarantees snake convergence. We will use the above theorem to characterize, for each external energy, its particular pathology and define a new external potential ensuring convergence whatever the geometry of the target curve.

3.2 Shape Propagation

Distance maps encode the evolution of the curve of level zero, γ_0, under a geometric flow defined, generically, by a parabolic PDE:

$$\gamma_t(u, t) = \beta(u, t)\overrightarrow{n} \ . \tag{3.3}$$

with initial condition $\gamma(u, 0) = \gamma_0(u)$ a closed curve and $\overrightarrow{n}$ denoting the unit inward normal. Each level curve of a given distance, d, corresponds to the solution to (3.3) at time $t = d$. This point of view, reduces the study of distance maps to the analysis of the propagation of the zero level curve governed by means of a geometric flow. We will use the machinery developed in [24] in order to study the drawbacks of the Euclidean distance map and define a more natural way of propagating shapes that will produce distance maps capable of guiding a snake to any closed curve. Since a plane curve is defined, up to rigid transformations, by its unit tangent, a pleasant way of handling geometric flows is by means of the equation of the angle of the unit

tangent, θ, in the arc length, s, parameterization. The advantage of this formulation is that we reduce the study of the properties of (3.3) to the analysis of a single equation, so that standard results on PDE's can be applied. The parabolic PDE for θ when the curve solves (3.3) is given by:

$$\theta_t(s,t) = \partial_s(\beta) + \left(\int_0^s \beta\theta_s ds\right)\theta_s \ . \tag{3.4}$$

with initial condition the angle of the unit tangent, θ_0, of the initial curve. An important remark is that the first order term arises due to the change of parameter, and, hence, it is present in any geometric flow.

3.2.1 Euclidean Distance Maps

In Euclidean distance maps, propagation of the initial curve, γ_0, is equivalent to mathematical morphology with a circle of radius 1 as structural element. Erosion corresponds to the inward propagation and dilation to the outward one. Hence the geometric flow associated [1] [64] is given by:

$$\gamma_t = \pm\overrightarrow{n} \ .$$

The minus sign corresponds to the dilation and the plus to the erosion. Since, in this case, $\beta = \pm 1$ is constant, the corresponding equation (3.4) for θ is simply:

$$\theta_t(s,t) = \pm(\int_0^s \theta_s ds)\theta_s \ . \tag{3.5}$$

This equation is a first order non-linear PDE that is solved [23] by means of the computation of the characteristic curves, that is, those curves in the s-t plane, $\alpha(u)$, such that the function solving (3.5) keeps constant, that is $\theta(\alpha(u)) \equiv const$. Assuming this last condition for $\alpha(u) = (s(u), t(u))$, we obtain that:

$$0 = \frac{d}{du}(\theta(s(u),t(u)) = t_u\theta_t + s_u\theta_s = t_u(\pm(\int_0^s \theta_s ds)\theta_s) + s_u\theta_s = (\pm t_u\theta + s_u)\theta_s \ .$$

Since the equality holds for all points in the characteristic, we have that α solves the first order PDE:

$$\pm t_u\theta + s_u = 0$$

And, consequently, its tangent vector fulfils the following system of ODE's:

$$\left.\begin{array}{rcl} t_u & = & 1 \\ s_u & = & \pm\theta \end{array}\right\}$$

Therefore, the characteristics through a point $(s_0, 0)$ are parameterized as:

$$\alpha(u) = (\pm\theta_0 u + s_0, u) \ .$$

where θ_0 equals $\theta_0(s_0, 0)$ and is constant along the characteristics.

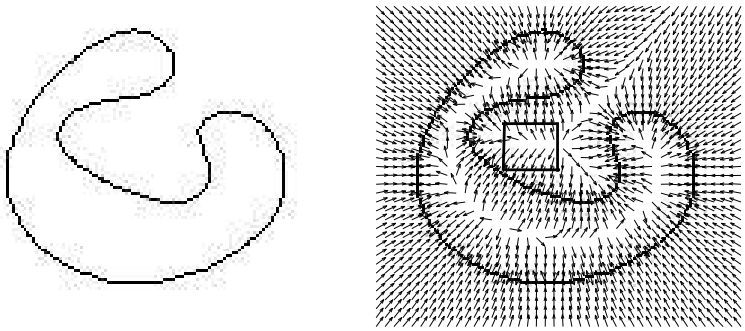

(a) (b)

Figure 3.2: Highly non-convex curve (a) and gradient of Euclidean distance map (b).

This means that we have straight lines in a plane which slopes, $\theta_0(s_0)$, do not need to be a monotonous function of the curve parameter. Variation of the characteristics slope along the initial curve is given by the derivative of the angle θ_0'. Since the initial curve is parameterized by its arc length, we have that the sign of the curvature of the initial curve determines whether the slopes increase or decrease. For convex curves, characteristics slope are either increasing (inward propagation) or decreasing (outward propagation) along the curve. Hence, two different characteristics never cross during the curve propagation and the distance map is a smooth map. However, for non-convex shapes, changes in the monotonicity of the slopes induced by the curve inflexion points make characteristics meet each other in finite positive time (squared region of fig. 3.2(b)) . At this time, the evolution of the angle develops a discontinuity or shock and the corresponding curve is not smooth any more. Indeed shocks in the angle domain translate into points or, even, curves where the gradient of the distance map cancels, that is, they correspond to crests and valleys of the distance map. Although this property is used in computer vision for extraction of shape skeletons [66], [69], it constitutes a main hindrance for shape modelling with snakes. Highly non-convex shapes (see fig. 3.2(a)) with the angle turning around more than π between two consecutive inflexion points produce distance maps with crests of positive slope (fig. 3.4(a)). These crests and valleys induce local minima in the snake energy functional that our deformable model, which seeks for zeros of the energy gradient, will never cross.

The best approach up to our knowledge to overcome the null gradient problem along curves is by means of the use of a regularized gradient (that only cancels at isolated points) as external force. Such regularization is obtained by means of the GVF [75] or its generalized faster version GGVF [77].

3.2.2 Gradient Vector Flow and Saddle Points

The GVF/GGVF technique [75], [77] consists in substituting the gradient of the external energy, ∇E_e, by the vector field $v(x)$ that is the steady-state of the reaction-diffusion vector equation:

$$u_t = g(|\nabla E_e|)\Delta u - h(|\nabla E_e|)(u - \nabla E_e) \quad \text{with } u(x,0) = \nabla E_e \tag{3.6}$$

The weighting functions, $g(\cdot)$ and $h(\cdot)$ are monotonically non-increasing and non-decreasing functions of the norm $|\nabla E_e|$, respectively. An important remark is that $h(0) = 0$. In this manner, the equilibrium vector field smoothly extends ∇E_e, thanks to the Laplacian, keeping close to the original gradient when the latter is significant enough. It can be used either to extend the edge map to the whole image or to regularize a gradient of a distance map. The main difference between GVF and GGVF is that the latter field keeps enough force as to drive the snake until the edge.

Notice that, in any of the two cases (GVF or GGVF), at parts of null gradient the equilibrium point is an harmonic function. Harmonic functions [61] do not admit accumulation of zeros and, thus, our vector field v will only have isolated points with $|v| = 0$. This important feature solves the problem of the distance map null gradient along curves (fig. 3.3 (b)). However, in both cases the geometry of the contours introduces saddle points in the vector field v, as the close up in fig. 3.3 (c) illustrates. These false minima of the snake energy trap, once again, the snake and prevent the deformable contour from entering into concave regions where the angle of the unit tangent, θ, turns around more than π.

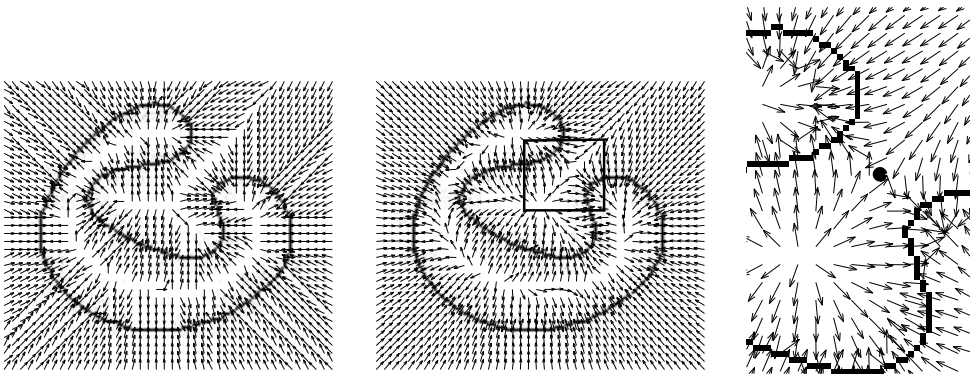

(a) (b) (c)

Figure 3.3: Gradient of Euclidean distance map to non-convex curve (a), GGVF (b) and saddle point of GGVF (c).

For regularization of gradients of Euclidean distance maps, saddle points appear because of shock formation during the propagation of the curve of level zero. In the case of extension of image gradients we find a similar problem. The Laplacian is an isotropic linear constant way of extending information. Therefore in every image region such that the contour/edge of interest is concave and the angle of the image

gradient (parallel to the unit normal of the curve) turns more than π, two opposite directions meet (fig. 3.3 (c)) and we have a saddle point.

In order to eliminate saddle points we need changing the propagation of shapes, so that the geometry of the contour to be extended is taken into account.

3.2.3 Curvature Vector Flow

Let us analyze the problem of the Euclidean distance map. From an analytic point of view, we see that equation (3.5) is a non-linear first order PDE, prone to develop shocks during the evolution. From a geometric one, it lies on the fact that we are propagating the curve at constant speed whatever its geometric features. In other words, the structural element used in the mathematical morphology is a circle of constant radius, which means that all points in the curve travel equal distance at the same time. We argue that the evolution should consider different metrics depending on the local geometry around each point so that structural circular elements of non constant radius are used. And what characterizes the local geometry of a curve better than curvature?. We propose a distance map based on the Mean Curvature Flow (MCF), that is, the evolution of the curve of level zero under the PDE given by:

$$\gamma_t = \kappa \overrightarrow{n} \ . \tag{3.7}$$

This equation makes points on the curve travel a distance that depends on the magnitude of the curvature, the higher its absolute value, the faster and further the point will move. From the mathematical morphology point of view we make the radius of the structural circle depend on the absolute value of the curvature. Now, can we assure, analytically speaking, that our evolution will stay smooth for all times?. On one hand we have that the equation (3.5) associated to θ in arc length parameter has turned into a PDE of parabolic elliptic type:

$$\theta_t = \theta_{ss} + (\int_0^s \theta_s^2 ds)\theta_s \ . \tag{3.8}$$

Hence by general theory on PDE's [23], we already know that our Curvature Distance Map (CDM) will be infinitely differentiable. Intuitively, the Laplacian that equation (3.8) contains introduces curvature into the characteristic lines, so that two characteristics do not intersect any more. Besides, the large amount of literature [32], [33], [34] on MCF, states that any initial curve evolves smoothly towards a convex shape, circular in the limit, before collapsing to a point. This is the key point to the definition of CDM.

Evolution by negative curvature	**Evolution by positive curvature**
$\gamma_t = \min((\kappa, 0))\overrightarrow{n}$	$\gamma_t = \max((\kappa, 0))\overrightarrow{n}$

(3.9)

We will define separately the outward and inward propagation in order to ensure maximal accuracy in the position of the snake. The analysis of Section 3.2.1 points out that convex shapes do not develop shocks during their propagation. An evolution of a non convex shape by negative curvature [49] stops as soon as the curve becomes

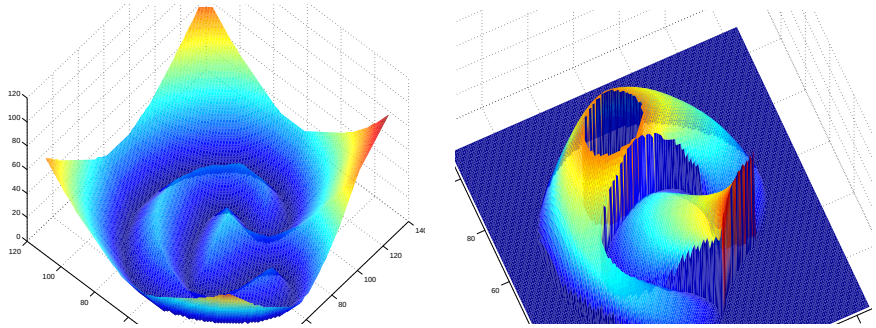

(a) (b)

Figure 3.4: Detail of Euclidean distance map, showing a crest of positive slope (a) and detail of Elliptic Distance Map (b) .

convex. Therefore, for the outward propagation, we will evolve the initial shape under the flow given by (3.9) until it stabilizes. The tracking of the curve for each time produces the level sets of the outward CDM for the non convex regions. To complete the outward CDM, we use an outward Euclidean distance map to the stable state of the flow by negative curvature. For the inward propagation we use evolution under positive curvature (3.9) until the curve becomes circular and then we use the Euclidean distance map to this circle to complete the inward propagation.

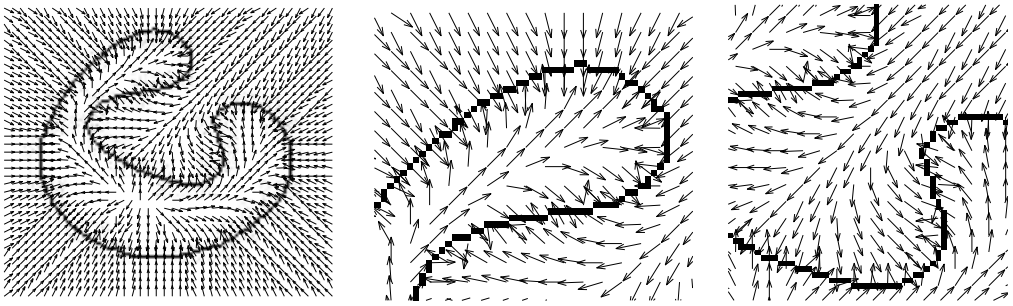

(a) (b) (c)

Figure 3.5: Gradient of the Elliptic Distance Map (a) and close-ups from the interior (b) and exterior (c).

Since there are not any self intersections between the level curves of CDM, by virtue of Theorem 3.1.1 we obtain maps (fig. 3.4 (b)) without curves of null gradient or saddle points (fig. 3.5 (a)). The gradient of this map, CVF, drives the snake to the zero level curve of CDM whatever its geometry. Details of CVF shown in figure 3.5 illustrate the absence of either saddle points or null gradients in both, the interior (fig. 3.5 (b)) and exterior (fig. 3.5 (c)) regions of a highly non-convex curve.

. . . . . .

The vector flow introduced in this chapter is an ideal tool for shape modelling, as far as shape contours are closed curves. Unfortunately, curves describing image main features, such as edges and ridges, are prone to be uncompleted, which difficulties applying CVF to object segmentation. It follows that in order to successfully use CVF in image segmentation, we need to be able to produce reliable closed models of unconnected sets of points. Once again, we will make use of the geometry of image level sets to define a new family of diffusion operators that uniformize the gray level of image characteristic curves, when applied to a gray level image, and complete unconnected curves if applied to their mask image.

Chapter 4

Restricted Diffusion

Anisotropic differential operators are widely used for image enhancement and restoration. However the capability of smoothly extending functions to the whole image domain has been hardly exploited.

As stated in chapter 1, functional extensions are governed by parabolic PDE's, which equal that of heat diffusion processes except for the boundary conditions. We saw that the process has naturally associated a metric, given by the diffusion tensor, that locally describes the way heat extends or distributes. Thus an anisotropic heat diffusion is the analytic way of handling a dilation with non-constant elliptic structural elements. In the context of level sets completion the tensor should degenerate/cancel in the gradient direction, which might not guarantee existence of solutions of the associated PDE. In the present chapter, we perform a study of diffusion tensors from the point of view of differential geometry which provides us with a criterion to decide when such degenerate tensors still produce solvable PDE's. We will define a new family of differential operators that locally restrict diffusion to the tangent spaces of image level sets. A particular instance of such operators results in an Anisotropic Contour Closing (ACC) that reduces the completion problem to the definition of a smooth vector field representing the level sets to be extended.

4.1 Restricted Anisotropic Operators

Any second order partial differential operator, namely L, defines, both, a diffusion process:

$$u_t = Lu \quad \text{with} \quad u(x,0) = u_0(x)$$

and a functional extension:

$$Lu = 0 \quad \text{with} \quad u_{|\gamma} = f$$

for γ a curve in the image domain. In both cases, existence and uniqueness (in the weak sense) of smooth solutions is guaranteed if L is strongly elliptic [23], [72], that is, when it defines a scalar product on some functional space. However, extensions focused on level sets continuation should restrict diffusion to a vector field representing

the level sets of the solution. Thus, the hypothesis of strong ellipticity is relaxed and we must tackle with operators that degenerate on some vector fields.

Let us give some geometric requirements over the non null space of L that ensure existence of solutions in the case of an operator given in divergence form. In this case, we have that:

$$Lu = \operatorname{div}(J\nabla u)$$

for J a symmetric (semi) positive defined tensor (quadratic form). Strong ellipticity means that all eigenvalues of J are strictly positive, meanwhile tensors having a null space (kernel) of positive dimension will produce degenerate operators. The fact that scalar products are given by symmetric (semi) positive defined tensors, motivates embedding elliptic operators into the framework of Riemmanian geometry to study the degenerate case. Details regarding results on differential geometry can be found in [67].

Let $(\mathbb{R}^n, g)$ be a Riemmanian manifold with the metric, g, given by a tensor J. Since the matrix J is symmetric, it diagonalizes [44] (considered as linear map) in an orthonormal basis that completely describes the metric. If Q is the coordinate change, then we have that, as bilinear form, $J = Q\Lambda Q^t$, for Λ the eigenvalue matrix. In this context, **isotropic** diffusion corresponds to equal eigenvalues, **anisotropic** to distinct and strictly positive and **restricted** [1] to the case of null eigenvalues. That is, the restricted diffusion is given by a diffusion tensor, $\tilde{J}$, defined by the following eigenvalue matrix:

$$\Lambda = \left(\begin{array}{ccc|ccc} \lambda_1 & \cdots & 0 & 0 & \cdots & 0 \\ \vdots & \ddots & \vdots & \vdots & \ddots & \vdots \\ 0 & \cdots & \lambda_m & 0 & \cdots & 0 \\ \hline 0 & \cdots & 0 & 0 & \cdots & 0 \\ \vdots & \ddots & \vdots & \vdots & \ddots & \vdots \\ 0 & \cdots & 0 & 0 & \cdots & 0 \end{array}\right)$$

Indeed we will only consider the homogeneous case $\lambda_i = 1$, for all i. Let us determine under what conditions a degenerated metric makes sense. Let $\xi_1, \ldots, \xi_k$ be the eigenvectors of positive norm and denote by $\mathcal{D} = \langle \xi_1, \ldots, \xi_k \rangle$ the vector space (distribution) they generate. If such vector space was the tangent space to a sub manifold of $\mathbb{R}^n$ (integral variety of $\mathcal{D}$), then the metric $\tilde{J}$ would be the projection onto its tangent space. Consequently a diffusion process governed by $\tilde{J}$ would not take place in the whole space $\mathbb{R}^n$ but just on the integral manifolds, namely M, of the distribution. We claim that this integrability condition and compactness are the only requirements for a unique solution to:

$$\operatorname{div}(\tilde{J}\nabla u) = 0 \quad \text{with} \quad u_{|\gamma} = f \tag{4.1}$$

which is as smooth as the boundary function f. We remit the reader to Section 4.3 for rigorous mathematical arguments concerning the above and the next statements. Let us devote the rest of the Section to intuitive reasonings on the precise meaning

[1] The word restricted applies to the the fact that diffusion restricts to the manifolds generated by the vectors of positive eigenvalues

of equation (4.1), those cases which always satisfy the integrability condition and applications to image processing.

Although (4.1) does not coincide with the heat equation for manifolds, the effect of the operator $\mathrm{div}(\tilde{J}\nabla u)$ may be regarded as diffusing on each of the integral manifolds separately. For $u_{|M} = u_M$ not only solves an elliptic second order equation in the manifold M, but also enjoys of the same properties as solutions to the heat equation in $\mathbb{R}^n$:

1. Maximum Principle: the extreme values of the solution u_M are achieved on the boundary $M \cap \partial\Omega$. In the particular case of a single generator, ξ, as M is a curve, the effect of restricting diffusion is that the final extension changes linearly along the level lines of ξ. Figure 4.1 is an example of functional extension in an image. The function to be extended is a color map defined on the ring of fig.4.1(a). The vector, ξ, guiding extension is the sinusoidal of fig.4.1(b) where the extension scope has been restricted to the area enclosed by the ring. The linear rate of change of the final extension (fig.4.1(d)) along the ξ integral curves is better visualized in fig.4.2. The mesh representation of fig.4.2(a) is a cut of the mesh surface of u in the ξ direction, the corresponding plot for u_M is in fig.4.2(b). Because we have not achieved the steady state, the function u_M does not linearly interpolate the values at the boundary as it happens in the plot of fig.4.2(d).

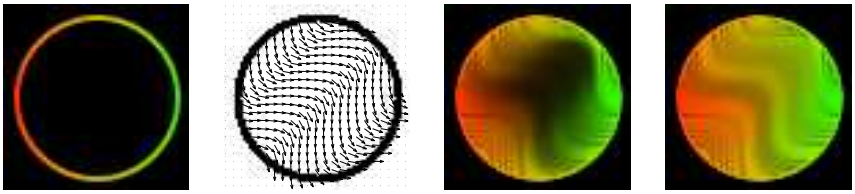

(a) (b) (c) (d)

Figure 4.1: General Extension: Function to extend (a), extension vector (b), intermediate step (c) and final extension (d)

2. Smoothness: the function u_M is smooth, provided $f_{|M}$ is also differentiable. Let us show the reader that the hypothesis that ξ can be integrated (i.e. induces a foliation) on the domain is essential in order to guarantee convergence to smooth functions. The vector shown in fig.4.3(a) has a singular point at the center of the image since all its integral curves meet there. Although the extension process still exists, it converges to the sharp image of fig.4.3(b), which has a jump discontinuity at the center of the image as it shows the angular cut of the mesh of fig.4.3(c).

The integrability condition ensuring existence of solutions is a standard result on differential manifolds known as the Frobenius Theorem [67]. The latter states that there exist integral manifolds for a distribution $\mathcal{D}$ provided that the vectors generating $\mathcal{D}$ fulfill an algebraic condition ($\mathcal{D}$ involutive). That is, a local condition

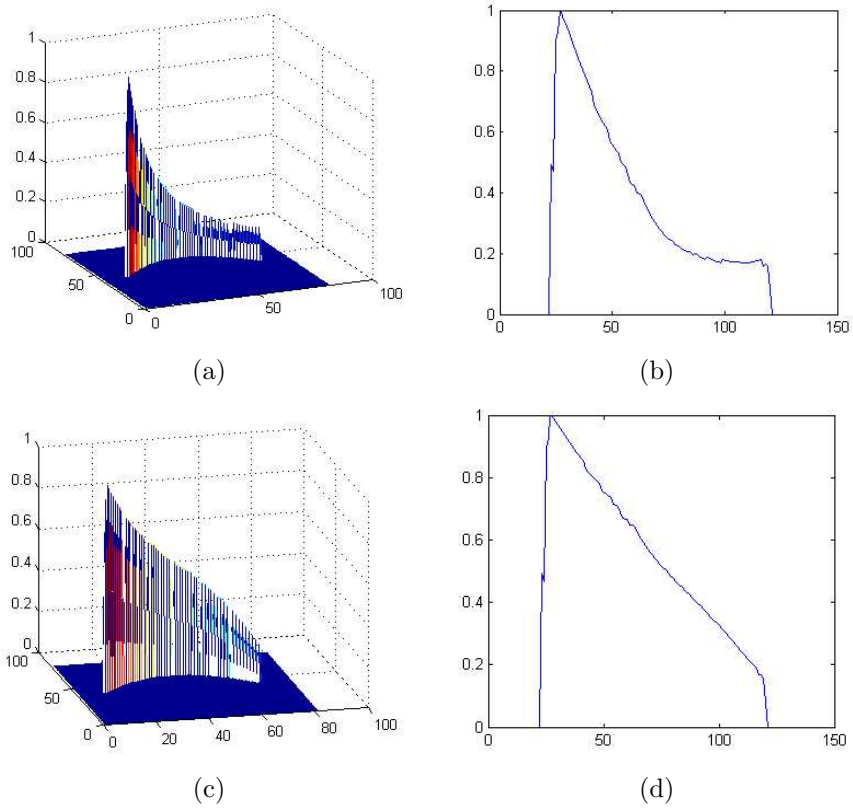

Figure 4.2: Rate of change along integral curves: intermediate step (a) with function plot (b) and final state (c) with function plot (d)

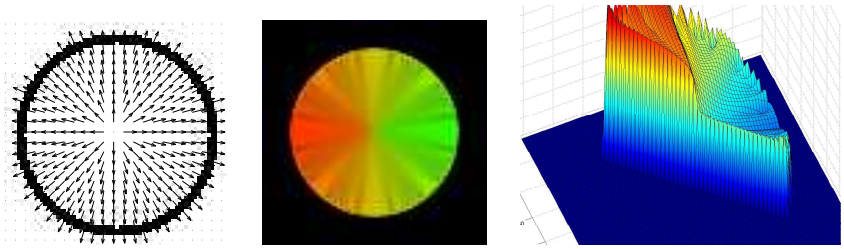

Figure 4.3: Singular Case: vector field (a), extension (b) and angular cut (c)

on the potential tangent spaces ensures that there will exist manifolds having $\mathcal{D}$ as tangent space. To be precise, the integrability condition is given in terms of the Lie bracket of $\xi_1, \ldots, \xi_k$ and, intuitively, measures whether the integral curves of the fields

generated by the distribution can form a mesh or not. We note that for $k \geq 2$ the integral curves of the vectors ξ_k will not, in general, tangle into a web. For instance, $\xi_1 = \partial_y = (0, 1, 0)$ and $\xi_2 = -y\partial_x + \partial_z = (-y, 0, 1)$ generate the curves of fig.4.4(b), which as do not knit a mesh will never produce a surface. Meanwhile, the integral curves of $\xi_1 = \partial_y$ and $\xi_2 = x\partial_x + \partial_z$ form mesh surfaces (fig.4.4(a)) which decompose the space in layers (leaves of the foliation). An important remark for the foregoing discussion is that in the case of a single vector ξ the integrability condition is always satisfied.

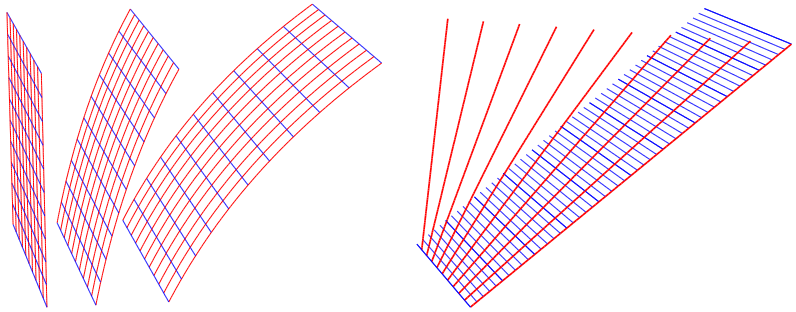

(a) (b)

Figure 4.4: Frobenius Theorem: integrable (a) and non integrable (b) distributions

The instances of the process 4.1 relevant in image processing are the following:

1. **Image Restoration**

   If M is closed and transversal to the foliation and $\nabla f \subset \mathcal{D}^{\perp}$, then the leaves of the foliation, M, describe the level sets of the extension u, coinciding in the case of an $n-1$ dimensional distribution. This follows from the fact that if $\nabla f \perp \mathcal{D}$, then we have that $\partial\Omega \cap M \subset \{f \equiv const\}$ and, thus, $u_{|M}$ is constant. Besides if $\dim \mathcal{D} = n-1$, as $\nabla f = \nabla u$, our restricted diffusion conforms to the Gestalt principle that requires that level sets continuation should be differentiable at boundary junctions. That is, the solutions suit to the idea of reliable image restoration.

   In this case, the restricted diffusion should be regarded as a simultaneous integration of all manifolds having as tangent space $\mathcal{D}$. This drives (4.1) very close to the system of PDE's used by [4] for image in-painting. The main advantage of our formulation is that it admits a simple implementation using a finite difference Euler scheme for a non-linear heat equation.

2. **Image Enhancement and Filtering**

   The time-dependent parabolic equation associated to the restricted diffusion:

   $$u_t = \mathrm{div}_{\mathbb{R}^n}(\tilde{J}\nabla u)$$

   with initial condition, $u(x, 0) = u_0(x)$ an arbitrary image, is an image filtering operator, provided that the vector ξ is a smooth approximation of the image

level sets. Because diffusion is performed along image level sets, image features are enhanced, in the sense that they are of uniform gray-level in the final image. Although this version of (4.1) resembles the diffusion of [9], there are some relevant differences. First of all, the degenerate differential operator:

$$u_t = \frac{1}{\sqrt{1+|\nabla u|^2}} u_{\xi\xi} \tag{4.2}$$

used in [9] can not be interpreted as a diffusion restricted to the integral curves of ξ. This follows because, given a function $u = u(x_1, \ldots, x_n)$ on $\mathbb{R}^n$, its divergence on a manifold embedded in $\mathbb{R}^n$ is given by:

$$\begin{aligned} \operatorname{div}_M(J\nabla u) &= \sum_m \langle \nabla u, \xi_m \rangle_M \cdot \operatorname{div}_M(\xi_m) + \sum_m \xi_m(\langle \nabla u, \xi_m \rangle_M) = \\ &= \sum_m u_{\xi_m} \cdot \operatorname{div}_M(\xi_m) + \sum_m u_{\xi_m \xi_m} + \sum_m \langle \nabla u, \xi_m(\xi_m) \rangle \end{aligned}$$

for $u_{\xi_m \xi_m}$ the second derivative in the direction ξ_m. It follows that even in the case of $\operatorname{div}(\xi_m) = 0$, the equation (4.2) can either be written in divergence form nor interpreted as diffusing the function just on the integral curves of ξ. Meanwhile the development of (4.1):

$$\operatorname{div}_{\mathbb{R}^n}(\tilde{J}\nabla u) = \sum_m \langle \nabla u, \xi_m \rangle_M \cdot \operatorname{div}_{\mathbb{R}^n}(\xi_m) + \sum_m \xi_m(\langle \nabla u, \xi_m \rangle_M)$$

is a second order operator on the integral manifolds, which coincides with a heat kernel in the case of null divergence.

Besides lacking of a geometric interpretation, it is not guaranteed that steady states of (4.2) are non trivial. This fact forces adding the usual close-to-data constraint [62] or relying on a given number of iterations to ensure preservation of the image most relevant features. Its geometric nature makes our restricted diffusion evolution equation converge to a non trivial image that preserves the original image main features as curves of uniform gray level.

3. **Contour Closing**

   If the manifold M is included in one of the leaves of the foliation associated to $\mathcal{D}$ and $f_{|M} = const$, the restricted diffusion corresponds to curve continuation and surface gap filling. This is the case we will focus on.

4.2 Anisotropic Contour Closing

We model the contour completion process as follows. Denote by γ the set of points to connect. Let us assume that ξ is a unitary vector field defined on a band around the curve in the image domain that smoothly extends the curve unit tangent. If we consider a metric $\tilde{J}$ with eigenvectors $\eta = \xi^{\perp}$ and ξ and eigenvalues $\lambda_1 = 0$ and $\lambda_2 = 1$, then equation (1.6) tells us that closed contours of the initial image are preserved during the evolution. Meanwhile for incomplete level curves, the effect of

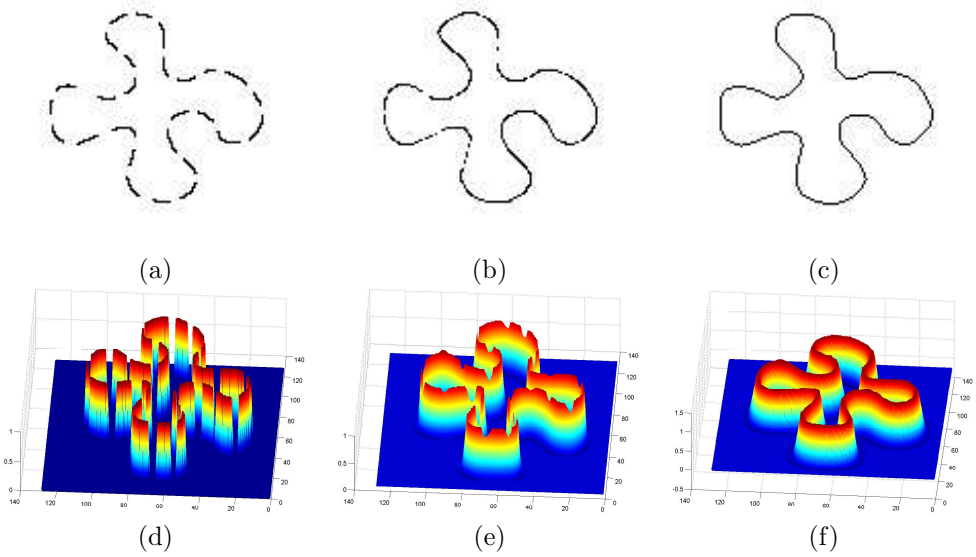

Figure 4.5: Gap filling: clover (a), ridges of its mask extension (b), (c), image graph of uncomplete clover (d), intermediate step (e) and closing (f).

distributing heat only in the tangent direction, makes these curves evolve towards a closed contour of uniform gray level.

Therefore if we use this restricted anisotropic operator to extend a binary map of a unconnected curve (i.e. its characteristic function), the final state will be a binary map of a closed model of the uncomplete initial contour. This process is the Anisotropic Completion of Contours we suggest:

$$\begin{aligned} u_t &= \mathrm{div}(\tilde{J}\nabla u) \\ u_{|\gamma} &= u_0 \end{aligned} \tag{4.3}$$

with u_0 the characteristic function of the opened contours, χ_γ, and the diffusion tensor $\tilde{J}$ as described in the previous paragraph. Figure 4.5 illustrates the different stages in the process of gap filling for an incomplete clover (fig.4.8(a)). Ridges of the final characteristic function (fig.4.8(f)) correspond to the reconstructed complete contour (fig.4.8(c)).

From the above considerations, computation of an extension conforming to the image reduces to giving a smooth vector field representing its level curves.

4.2.1 Coherence Vector Fields

This section is devoted to the computation of a extension, ξ, of the unit tangent of an unconnected curve γ_0 smooth in a band surrounding the curve. Following the ideas presented in [26], we will use the Structure Tensor, St, upon a suitable function to

compute the vector field ξ. Notice that since orientations do not play any role in the diffusion process, the eigenvectors of St serve to design diffusion tensors [72].

The Structure Tensor is usually employed to determine the direction of maximum contrast change of an image u in a robust way [72]. Given an integration scale, ρ, it is defined as the mean of the projection matrices, $P(\nabla u_\sigma)$, onto a regularized image gradient:

$$St_\rho = G_\rho * P(\nabla u_\sigma) = G_\rho * (\nabla u_\sigma \otimes \nabla u_\sigma) = G_\rho * \left(\nabla u_\sigma \nabla u_\sigma^T\right)$$

where G_ρ denotes a centered gaussian of variance ρ and $\nabla u_\sigma = G_\sigma * \nabla u$. The eigenvector of minimum eigenvalue, ξ, (coherence direction) corresponds to the level sets unit tangent direction.

Since by convolving with a gaussian we obtain solutions to the heat equation, we have that the Structure Tensor benefits from the regularizing and extension properties of diffusion processes. The matrix St_ρ is the solution to the heat equation with initial condition the projection matrix onto the image gradient vector space. This implies that the coherence direction, ξ, is a infinitely differentiable field [24] that regularizes and extends the level curves unit tangent space. This property is the key point for the definition of the different Coherence Vector Fields. We will note by γ_0 the contour to be closed and by t_0 its tangent space.

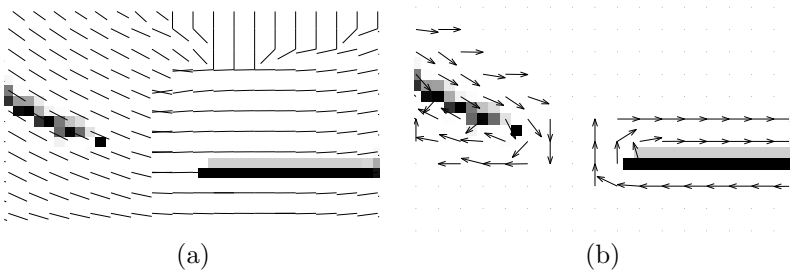

Figure 4.6: LVF extension (a) of tangent vector at a gap (b)

1. **Linear Vector Fields (LVF).**

   They are the coherence direction of the Structure Tensor compute over the characteristic function χ_{γ_0}. By the above properties, ξ is a smooth vector field defined (i.e. non zero) in a neighborhood of γ_0 that correctly matches t_0 at gap boundaries and coincides with it at other points. Figure 4.6 shows the gradient of χ_{γ_0} (fig.4.6 (b)) used to compute the vector ξ of fig.4.6 (a). Since ξ scope may not be large enough as to fill all gaps, it must be updated during the extension process. Intuitively, this dynamic process yields closed shapes that resemble the one we would get if we drew the tangent at the boundary points of the original curve and intersected the lines. This might lead to undesirable wrong models (fig.4.8 (b)) when the angle between the unit tangent of two consecutive pieces is too acute as the vector field becomes singular (fig.4.8 (a)). Besides, this pathology of the vector guiding the extension difficulties stopping the process.

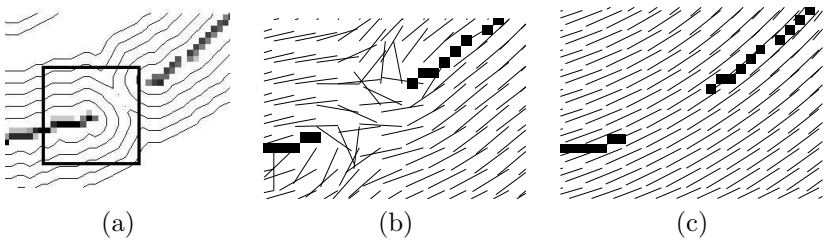

Figure 4.7: DVF extension: distance map (a), tangent spaces (b), DVF (c)

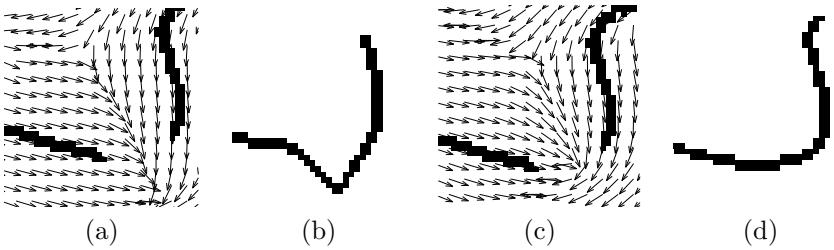

Figure 4.8: Corners Extension: LVF (a), LVF closure (b), DVF (c) and closure (d)

Note that LVF is nothing but the coherence direction of the convolution $G_\sigma * \chi_{\gamma_0}$, which level sets might be regarded as a propagation of the original curve. The fact that geometric flows are the natural way of propagating and deforming shapes leads to:

2. **Distance Vector Fields (DVF).**

   Let u be a function representing the evolution of γ_0 under a monotonous geometric flow, $\gamma_t = \beta\overrightarrow{n}$, with $\beta > 0$. That is, the level sets, $u \equiv c$, coincide with the evolution of γ_0 at time $t = c$. Notice that at a suitable time/scale, ρ, (gap dependent) the level curves of this distance map have only two connected components that model a closure of γ_0 (fig.4.7(a)). It follows that the coherence direction, ξ, models a closure of γ_0 (fig.4.7(c)) that smoothly interpolates t_0 at gaps and is not singular at corners (fig.4.8(c)). The shapes obtained are smooth models (fig.4.8(d)) of the original shape based on the principle of minimum distance for joining boundary points. Although, this is a desirable property, in the particular case of a distance between contours smaller than the gap size, LCV is preferable, as DVF closed models do not conform to the shape yielded by our visual system. For instance, DVF reconstruction of the broken lines of fig. 4.9(a) are not two straight lines, as expected, but the curves of fig.4.9 (b). We remit the reader to the experiments in chapter 5.2 for illustrative examples on the choice of the coherence vector field in practical applications

We have chosen a non convex contour in order to illustrate the dynamic process of contour completion in fig.4.10. If gaps are not too large DVF can be computed

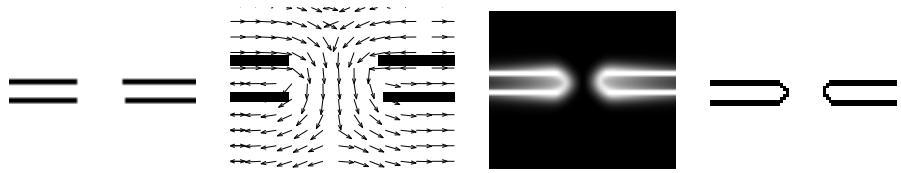

Figure 4.9: DVF pathology: lines (a), DVF (b), final extension (c), DVF closure (d)

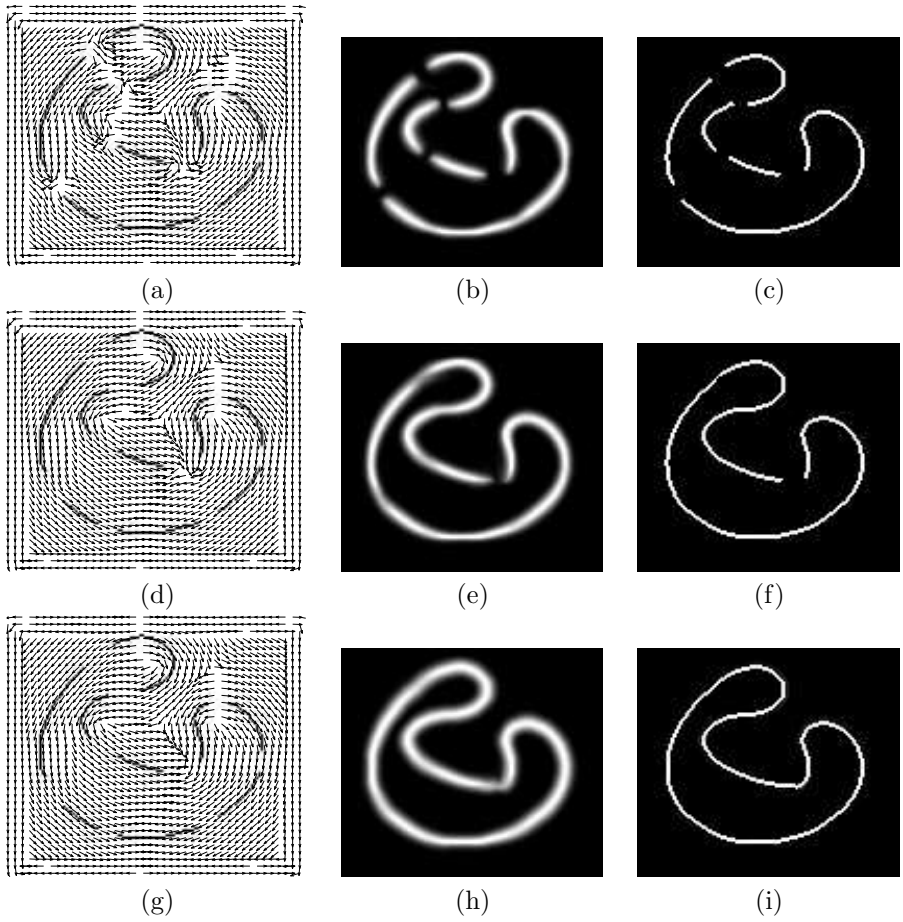

Figure 4.10: Dynamic Closing of Contours

once at the beginning of the process. However, in the general case, in order to get the maximum accuracy as possible, we recommend updating DVF over the ridges of

the current image evolution every k iterations. The initial DVF (fig.4.10(a)) closes the smallest gaps and reduces the length of the gaps in the ridges (fig.4.10(c)) of the evolved image (fig.4.10(b)). DVF over the distance map of image ridges yields a vector field (fig.4.10(d)) that closes all gaps with the exception of the largest one (fig.4.10(e), (f)), which is the most delicate since we must interpolate a piece of high curvature. The DVF that finally closed this gap is the vector field of (fig.4.10(g)). Ridges of the final extension (fig.4.10(h)) are the reconstructed shape of fig.4.10(i) and represent a smooth and accurate completion of the contour regardless of the magnitude of the curvature.

4.3 Mathematical Issues

This section deals with the mathematical arguments that yield existence of solutions to the restricted diffusion. In mathematical formal terms, the problem is stated as follows. Let Ω be a compact subset of $\mathbb{R}^n$ with a smooth boundary, $\partial\Omega$, and let $f = f(x_1, \ldots, x_n)$ be a smooth function defined on $\partial\Omega$. We seek for solutions to the following extension problem:

$$\operatorname{div}(\tilde{J}\nabla u) = 0 \quad \text{with} \quad u_{|\partial\Omega} = f \tag{4.4}$$

for $\tilde{J}$ the projection matrix onto a distribution $\mathcal{D} = \langle \xi_1, \ldots, \xi_k \rangle$ transversal to $\partial\Omega$ almost everywhere:

$$\tilde{J} = \begin{pmatrix} \xi_1 \\ \vdots \\ \xi_k \end{pmatrix} \left(\begin{array}{c|c} Id_k & 0 \\ \hline 0 & 0 \end{array} \right) (\xi_1, \ldots, \xi_k)$$

Because the diffusion tensor cancels on some curves, standard arguments on elliptic PDE do not apply. One way of proving existence and uniqueness to (4.4) could be through viscosity solutions [23], [20]. We, instead, will approach the problem from a differential geometry point of view and show that (4.4) yields a heat equation on the integral varieties of the distribution $\mathcal{D}$ (if it is involutive), which coincides with the laplacian operator [21] for manifolds provided that the divergence of the fields ξ_i is zero. Existence of solutions on a generic leave of the folliation suffices to guarantee existence and uniqueness of functions $u = u(x_1, \ldots, u_n)$ solving the restricted diffusion problem (4.4) in $\mathbb{R}^n$.

4.3.1 Solutions to the Problem on Manifolds

In order to show that (4.4) is solvable on a generic leave, M, we will first compute its expression in local coordinates and, then, construct a solution.

Relation between Restricted Diffusion and the Heat Equation for Manifolds

We start with a brief introduction to notations and definitions. For a given Riemmanian manifold, N, its scalar product will be noted by $\langle \cdot, \cdot \rangle_N$, the divergence of a

vector field by $\mathrm{div}_N(\cdot)$, Lie derivatives by L and the Lie bracket by $[\cdot,\cdot]$. We recall that if $(x_1,\ldots,x_N)$ are local coordinates, then the partial derivatives ∂_{x_i} are a basis of the tangent spaces T_pN and its dual, dx_i, are a basis of the cotangent (linear forms) T_p^*N.

It follows that, in local coordinates, a vector field ξ equals $\sum \xi^k \partial_{x_k}$, the derivative, $\xi(f)$, of any smooth function $f : N \to \mathbb{R}$ is given by:

$$\xi(f) = \sum \xi^k \partial_{x_k} f$$

and the metric by a (symmetric) matrix $(g_{ij})_{ij}$. Furthermore, if $g = \det(g_{ij})$ is its determinant, then the volume form equals $\omega = g^{1/2} dx_1 \ldots dx_N$. The divergence of a vector field ξ can be defined as the Lie derivative of ω along ξ:

$$L_\xi \omega = \mathrm{div}_N(\xi)\omega$$

The quantity measures the change of a unit of volume along the integral curves of ξ (fig. ....). The fact [67] that:

$$\xi(\omega(\partial_{x_1},\ldots,\partial_{x_1})) = (L_\xi\omega)(\partial_{x_1},\ldots,\partial_{x_1}) - \sum_i \omega(\partial_{x_1},\ldots,[\xi,\partial_{x_i}],\ldots,\partial_{x_1})$$

yields that the expression of $\mathrm{div}_N(\xi)$ in local coordinates is:

$$\mathrm{div}_N(\xi) = g^{-1/2}\xi(g^{1/2}) + \sum_i \partial_{x_i}(\xi^i) \tag{4.5}$$

Given a smooth function, f, it has an associated form, df, defined as:

$$df(\xi) = \xi(f) = \sum \xi^k \partial_{x_k}(f)$$

The gradient, ∇f, of such function it is defined [21] as $j^{-1}(df)$, for:

$$j : T_pN \to T_p^*N$$

the isomorphism given by the metric $j(\xi)(\eta) := \langle \xi, \eta \rangle_N$. It follows that:

$$\langle \nabla f, \xi \rangle_N = j(j^{-1}(df))(\xi) = \xi(f) \tag{4.6}$$

The above formulae (4.5), (4.6) are the only expressions we need to compute (4.4) in the local coordinates of a generic leave M. If M is a manifold embedded in $\mathbb{R}^n$, then given a coordinate chart:

$$\begin{array}{rccc} \phi: & U \subset \mathbb{R}^k & \longrightarrow & M \subset \mathbb{R}^n \\ & s = (s_1,\ldots,s_k) & \mapsto & (\phi_1(s),\ldots,\phi^n(s)) = x \end{array}$$

The vector fields ∂_{s_i} are given by $\partial_{s_i}(\phi) = (\phi^1_{s_i},\ldots,\phi^n_{s_i}) = \phi^1_{s_i}\partial_{x_1} + \cdots + \phi^n_{s_i}\partial_{x_n}$ and the scalar product by $(g_{ij})_{ij} = (\langle \partial_{x_i}, \partial_{x_j} \rangle_{\mathbb{R}^n})_{ij}$. In the case that M is an integral

manifold of a distribution $\mathcal{D}$, its generators $\xi_1, \ldots, \xi_k$ can be expressed in, both, s and x coordinates with the relation:

$$\xi_m = \xi_m(x_1, \ldots, x_n) = \sum_j \tilde{\xi}_m^j \partial_{x_j} = \xi_m(s_1, \ldots, s_k) = \sum_k \xi_m^k \partial_{s_k} =$$
$$= \sum_k \xi_m^k (\sum_i \phi_{s_k}^i \partial_{x_i}) = \sum_j (\sum_k \xi_m^k \phi_{s_k}^i) \partial_{x_j} \tag{4.7}$$

Equipped with the above tools and notations formula (4.4) writes:

$$\begin{aligned} \mathrm{div}_{\mathbb{R}^n}(\tilde{J}\nabla u) &= \mathrm{div}_{\mathbb{R}^n}(\langle \nabla u, \xi_m \rangle_{\mathbb{R}^n} \cdot \xi_m) = \\ &= \sum_m \langle \nabla u, \xi_m \rangle_{\mathbb{R}^n} \cdot \mathrm{div}_{\mathbb{R}^n}(\xi_m) + \sum_m \xi_m(\langle \nabla u, \xi_m \rangle_{\mathbb{R}^n}) = \\ &= \sum_m \langle \nabla u, \xi_m \rangle_M \cdot \mathrm{div}_{\mathbb{R}^n}(\xi_m) + \sum_m \xi_m(\langle \nabla u, \xi_m \rangle_M) \end{aligned} \tag{4.8}$$

where the last equality follows from the relations (4.6) and (4.7) in the case that $\mathrm{div}_{\mathbb{R}^n}(\tilde{J}\nabla u)$ is restricted to M. Before deducing from the above expression the equation in local coordinates that yields existence and uniqueness of solutions to (4.4) on M, let us show the relation between (4.8) and heat equations on manifolds.

As in the case of $\mathbb{R}^n$, heat equations on manifolds are given by divergence operators $\mathrm{div}_M(J\nabla u)$, for J a symmetric positive defined 2-form (i.e. a metric). It follows that if $\xi_1, \ldots, \xi_k$ are the unitary vector fields, then:

$$\mathrm{div}_M(J\nabla u) = \sum_m \langle \nabla u, \xi_m \rangle_M \cdot \mathrm{div}_M(\xi_m) + \sum_m \xi_m(\langle \nabla u, \xi_m \rangle_M) \tag{4.9}$$

The Laplacian corresponds to the case $J = Id$.

If the vector fields have null divergence in $\mathbb{R}^n$, then the two expressions (4.8) and (4.9) are equal to:

$$\sum_m \xi_m(\langle \nabla u, \xi_m \rangle_M) = \sum_m \xi_m(\langle \nabla u, \xi_m \rangle_{\mathbb{R}^n}) = \sum_m \xi_m(u_{\xi_m})$$

where u_{ξ_m} is the partial derivative (in $\mathbb{R}^n$) in the direction $\xi_m(x_1, \ldots, x_n)$. This coincidence of formulations leads to:

Proposition 4.3.1 *If* $\mathrm{div}_{\mathbb{R}^n}(\xi_i) = 0$*, for all* i*, then there exists a unique solution to the problem (4.4) on each integral manifold of* $\mathcal{D}$*, provided that they are complete (compact).*

Proof. The proof is straightforward by existence of heat kernels in manifolds [21]. □

Remark: We note that, in the 2 dimensional case, it suffices that $\xi = \nabla f^{\perp}$.

In the general case, we need the expression (4.8) in local coordinates for a suitable open covering (so that boundary conditions are taken into account) to construct a solution. Although this constitutes an extra theoretic effort, from the computational point of view the restricted diffusion has several advantages over the heat equation

for manifolds. Non existence of an explicit formulation for the heat kernel, makes that, in any case, both equations (4.8), (4.9) are solved numerically. The best way of handling equations over manifolds (curves) is via an implicit formulation [65]. A main advantage is that (4.4) provides with a global expression for (4.8) in $\mathbb{R}^n$ coordinates which is easily integrated using an explicit Euler scheme for non-linear heat equations. Besides because the operator (4.8) is of second order it enjoys from the same smoothing and regularizing properties as (4.9).

Existence of Solutions and Properties

Let us first give the expression in local coordinates. Using the same notations as in the previous Section, we have that, in a generic local chart $(s_1, \ldots, s_k)$, the operator is given by:

$$\begin{aligned}\operatorname{div}_{\mathbb{R}^n}(\tilde{J}\nabla u)_{|M} = \sum_m \langle \nabla u, \xi_m\rangle_M \cdot \operatorname{div}_{\mathbb{R}^n}(\xi_m) + \sum_m \xi_m(\langle \nabla u, \xi_m\rangle_M) = \sum_m f_m(s)\xi_m(u) + \\ + \sum_m \xi_m(\xi_m(u)) = \sum_m u_{\xi_m\xi_m} + \sum_m f_m(s)\xi_m(u) + \langle \nabla u, \xi_m(\xi_m)\rangle_M\end{aligned}$$

where $\xi_m(\xi_m)$ stands for the vector filed $\sum_k \xi_m(\xi_m^k)\partial_{s_k}$. The second order term $\sum_m u_{\xi_m\xi_m}$ is of elliptic type. In fact, since the vectors ξ_k are orthonormal, we have the following matrix equalities:

$$(\xi_m^k)^{-1}_{km}(u_{s_is_j})_{ij}(\xi_m^k)_{km} = (\xi_m^k)^t_{km}(u_{s_is_j})_{ij}(\xi_m^k)_{km} = (u_{\xi_i\xi_j})_{ij}$$

Invariance of traces under linear coordinate changes, yields that $\sum_m u_{s_ms_m} = \sum_m u_{\xi_m\xi_m}$. It follows that, in local coordinates (4.8) equals:

$$\underbrace{\sum_m u_{s_ms_m}}_{\text{2nd order}} + \underbrace{\sum_m f_m(s)\xi_m(u) + \langle \nabla u, \xi_m(\xi_m)\rangle_M}_{\text{1st order}} \tag{4.10}$$

which is an elliptic second order operator. General arguments on elliptic PDE yield the following result:

Theorem 4.3.1 *Let M be a compact Riemmannian manifold embedded in $\mathbb{R}^n$ with boundary ∂M. If ξ_m are orthonormal vectors fields and f is a smooth function, then the following boundary problems have a unique smooth solution:*

1. $\operatorname{div}_{\mathbb{R}^n}(\tilde{J}\nabla u)_{|M} = f$, *with* $u_{|\partial M} = 0$
2. $\operatorname{div}_{\mathbb{R}^n}(\tilde{J}\nabla u)_{|M} = 0$, *with* $u_{|\partial M} = f$
3. $u_t = \operatorname{div}_{\mathbb{R}^n}(\tilde{J}\nabla u)_{|M}$, *with* $u_{|\partial M} = f$ *and initial condition a smooth function* u_0.

for $\tilde{J}$ the projection matrix onto $\langle \xi_1, \ldots, \xi_k\rangle$.

Proof. The operator $\operatorname{div}_{\mathbb{R}^n}(\tilde{J}\nabla u)_{|M}$ will be noted by Lu for short.

1. $\mathrm{div}_{\mathbb{R}^n}(\tilde{J}\nabla u)_{|M} = f$, with $u_{|\partial M} = 0$

   Since M is compact, whatever coordinate covering, it exists a finite sub covering, U_i. Let φ_i be a partition of unity subordinated to this covering and note $f_{U_i} = \varphi_i f$. For any such coordinate set, the equation converts into the elliptic PDE given by (4.10). It follows that the local problem:

   $$Lu^i = f_{U_i} \qquad u_{|\partial U_i} = 0$$

   has a unique smooth solution defined on U_i. We claim that the function, u, defined as:

   $$u(p) = \sum_i u^i(p)$$

   is a solution. First note that it is well defined as the summation is finite. Second, by linearity of L, we have that:

   $$Lu = \sum_i Lu^i = \sum_i f_{U_i} = (\sum \varphi_i) f = f$$

   as $\sum_i \varphi_i(p) = 1$. It only remains to check that on the boundary ∂M the function cancels. If V_k is the subset of U_i intersecting the boundary, then $\partial V_k \cap \partial M$ is a covering. It follows that, for any $p \in \partial M$, $u(p) = \sum_k u^k(p) = 0$.

2. $\mathrm{div}_{\mathbb{R}^n}(\tilde{J}\nabla u)_{|M} = 0$, with $u_{|\partial M} = f$

   If $\tilde{u}$ solves:

   $$\mathrm{div}_{\mathbb{R}^n}(\tilde{J}\nabla \tilde{u})_{|M} = \tilde{f}, \qquad u_{|\partial M} = 0$$

   for $\tilde{f} = Lf$. Then $u = f - \tilde{u}$ solves 2.

3. $u_t = \mathrm{div}_{\mathbb{R}^n}(\tilde{J}\nabla u)_{|M}$, with $u_{|\partial M} = f$ and initial condition u_0

   It follows by existence of solutions to 2, by general arguments on PDE's.

□

Solutions enjoy from identical properties than solutions to the problem in Euclidean space:

Proposition 4.3.2 *The solution to the extension problems 2 and 3 of Theorem 4.3.1 is infinitely smooth and fulfills the maximum principle:*

$$\max_M u = \max_{\partial M} u = \max_{\partial M} f, \text{ for the case 2}$$

$$\max_t u(t) = \max(u_0, f), \text{ for the case 3}$$

Proof. Straightforward since both properties are local and the expressions in local coordinates given by (4.10) satisfy them. □

Remark: If the boundary function f is not smooth, the solution is $\mathcal{C}^\infty$ only on the interior of the gap.

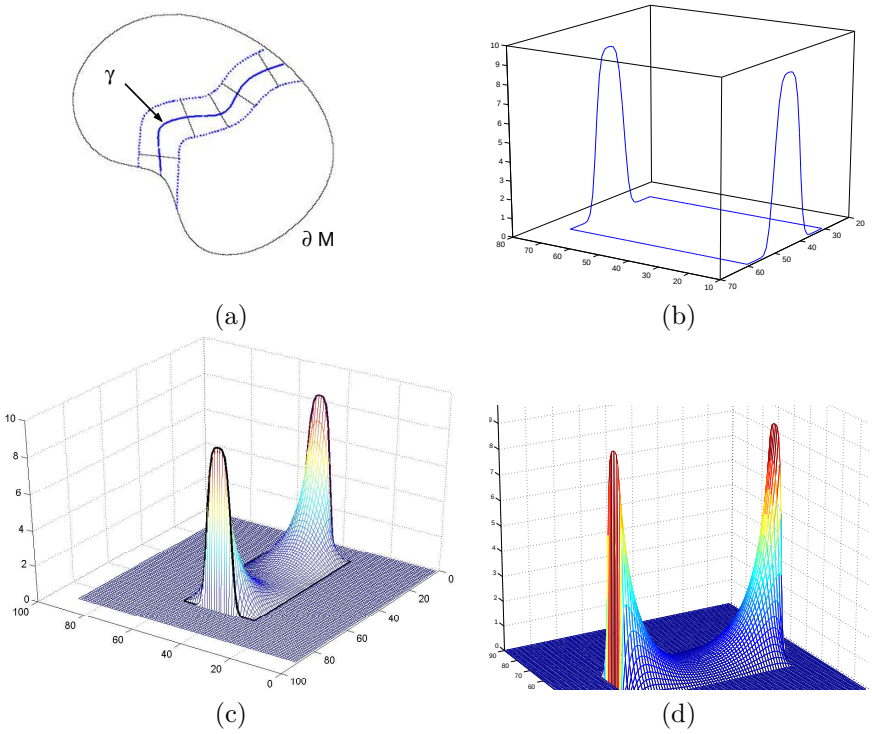

Figure 4.11: Extension on coordinate chart: tubular chart (a), function on the boundary (b), extension (c) and maximum principle (d)

Figure 4.11 illustrates the behavior of a solution to the parabolic problem 3 in a strip-like coordinate chart joining two pieces of the boundary ∂M. We note that we can always assume this kind of covering. This follows because, as M is geodesically complete (it is compact), for any two points on the boundary there exists a geodesic, γ, achieving the distance between them. Now by the embedding $M \hookrightarrow \mathbb{R}^n$, this geodesic is also a curve in $\mathbb{R}^n$, where it has a trivial normal bundle. Projecting the latter onto the distribution, we have that the geodesic normal bundle in M is also trivial. Any tubular neighborhood associated to a basis, $\eta_1, \ldots, \eta_{k-1}$, of the bundle yields a strip-shaped coordinate chart:

$$(s, r_1, \ldots, r_{k-1}) \mapsto \gamma(s) + \sum r_j \eta_j$$

joining to pieces of ∂M. The drawing in fig.1.11(a) outlines the construction of such strip coordinate chart and the plot of fig.4.11(b) represents the function φf in the case of a constant boundary function. On such a band around γ, the function interpolating the boundary values (fig.4.11(c)) satisfies the maximum principle and is of hyperbolic type (fig.4.11(d)) in the two dimensional case. The sum of contributions for all open charts would yield the constant function on M.

This Theorem is the basis for the main result of the chapter:

4.3.2 Solutions to the General Problem

The goal of this section is to prove that (4.4) has a unique solution which is as differentiable as the boundary function f, provided that $\mathcal{D}$ is involutive and that for all integral manifolds, M, the function f is smooth on $\partial\Omega \cap M$. We will first prove existence and uniqueness and, then, approach differentiability of solutions.

Theorem 4.3.2 *Let Ω be a compact subset of $\mathbb{R}^n$ with a smooth boundary, $\partial\Omega$ and $\mathcal{D} = \langle \xi_1, \ldots, \xi_k \rangle$ an involutive distribution. If f is a function defined on $\partial\Omega$ such that restricted to the integral manifolds od $\mathcal{D}$ is smooth, then there is a unique solution to the restricted diffusion problem given by:*

$$\operatorname{div}(\tilde{J}\nabla u) = 0 \quad \textit{with} \quad u_{|\partial\Omega} = f$$

where $\tilde{J}$ is the projection matrix onto $\mathcal{D}$.

Proof. As shown in the previous Sections, the differential operator restricts to a elliptic PDE on each of the integral manifolds, M, of the distribution $\mathcal{D}$, which, by Theorem 4.3.1, has a unique smooth solution, namely u_M, that extends $f_{|\partial\Omega\cap M}$ to the whole leave. Now, by Frobenius Theorem these manifolds foliate the whole space, so that $\forall p \in \mathbb{R}^n$, there exists a unique leave Mp through the point. The function in $\mathbb{R}^n$ defined as $u(p) = u_{Mp}(p)$ solves the general equation. □

Theorem 4.3.3 *Solutions given by Theorem 4.3.2 are as smooth as the boundary function f is on $\partial\Omega$.*

Proof. Because it suffices to check the statement locally, we can assume that we are in a generic coordinate chart given by the Frobenius theorem, where the leaves of the distribution $\mathcal{D}$ correspond to the hyper-planes $\{x_1 = c_1, \ldots, x_M = c_M\}$, for $M = n - k$. We will show that for any such neighborhood cutting $\partial\Omega$, the solution $u(x_1, \ldots, x_n)$ is as differentiable as f. The statement follows by, iteratively, repeating the argument to the function u restricted to the boundary of the closure of an interior neighborhood.

Let us assume that f is $\mathcal{C}^n$ and that the coordinate system is the one given by Frobenius. We recall that by compactness of Ω, the boundary function f is, indeed, uniformly smooth and that by Proposition 4.3.2, we already have that u is uniformly $\mathcal{C}^n$ with respect to the coordinates, $(x_M, \ldots, x_n)$, that define the distribution. In order to prove differentiability with respect to the other coordinates, we note that because the distribution is transversal to $\partial\Omega$ almost everywhere there are only two possibilities:

1. All leaves $\{x_1 = c_1, \ldots, x_M = c_M\}$ are transversal to the boundary.

   In this case (fig.4.12(a)), modulo a permutation of the last coordinates $(x_M, \ldots, x_n)$, the boundary is given by a graph $x_n = \phi(x_1, \ldots, x_{n-1})$. It follows that in coordinates $(Y, X) = (y_1, \ldots, y_M, \tilde{x}_{M+1}, \ldots, \tilde{x}_n) = (x_1, \ldots, x_M, x_{M+1}, \ldots, x_{n-1}, x_n -$

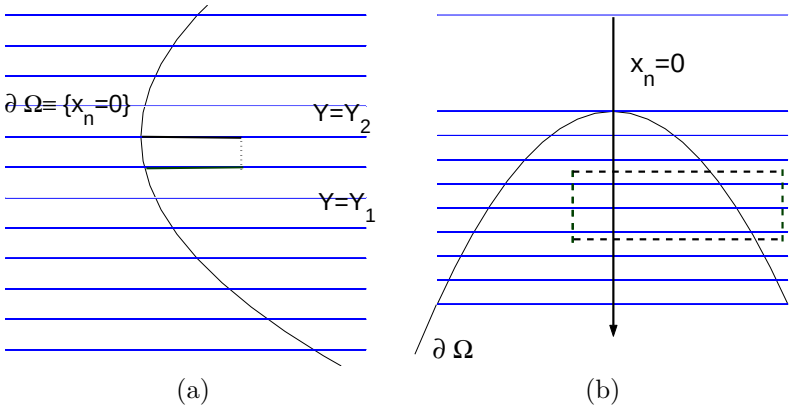

Figure 4.12: Foliation transverse (a) and tangent (b) to the boundary

$\phi(x_1, \ldots, x_{n-1})$), the integral manifolds are given by $\{Y = const\}$ and the boundary by $\partial\Omega = \{x_n = 0\} \supseteq \{X = 0\}$. Using this coordinate system, we have that:

$$|u(Y_1, X_0) - u(Y_2, X_0)| \leq |u(Y_1, 0) - u(Y_1, X_0)| + |u(Y_1, 0) - u(Y_2, 0)| +$$
$$+ |u(Y_2, 0) - u(Y_2, X_0)| \leq |u_{|M}(0) - u_{|M}(X_0)| + |f(Y_1, 0) - f(Y_2, 0)| +$$
$$+ |u_{|M}(0) - u_{|M}(X_0)| \leq C_M||X_0|| + C_M||X_1|| + C_f||Y_1 - Y_2||$$

The last inequality by uniform continuity of both $u_{|M}$ and f and, holding, for any partial derivative of u of order less or equal to n. We conclude that the function u is as smooth as f.

2. There is a (single) leave tangent to the boundary as in fig.4.12(b).

   As the boundary is not diffeomorphic to any hyper plane defined by the last $n - M$ coordinates, we can not directly apply the above argument. We claim that the solution restricted to the axis $\{x_n = 0\} \supseteq \{X = 0\}$ is as smooth as f, which reduces this case to the previous one. Intuitively, such degree of differentiability follows from the fact that the extension process may be understood as propagating the values of f along the leaves. The formal proof is a straight consequence of the argument given in the first case applied to a neighborhood not containing the tangent leave (like the dotted square of fig.4.12(b)).

□

. . . . . .

Chapter 5

Experiments

5.1 Performance of the Regularized Curvature Flow

In this section we present an extensive comparison of RCF to other PDE-based techniques based on 4 main principles: image quality, convergence to non-trivial images, automatic stabilization of the iterative process and robustness. The former novel protocol of performance assessment points that RCF and the geometric flows [49], [79] achieve a better compromise between quality of the restored image and stabilization of the iterative process than diffusion-like techniques. However, experiments on real images select RCF as the better posed for non-user gated procedures. An application to segmentation of ultrasonic medical images, [25], proves RCF usefulness in real problems.

5.1.1 Establishing a Stopping Criterion

In practical applications stopping the iterative smoothing can be as important as the quality of the restored image. Even if there are not any image-dependant parameters in the continuous formulation, the numeric algorithm may fail to stop without manual intervention. Stabilization achieved using standard numeric techniques ([18], [70]), ensures that the parameters involved in the stopping stage do not depend upon the particular image restoration. Given a generic iterative scheme:

$$u_{t+1} = u_t + \Delta t \cdot speed$$

two different **stop criteria** can be defined to detect its steady-state:

- Criterion A (critA): *Minimum Speed Value Criterion.* Maximum difference between two consecutive images, i_t, i_{t+1}, should be under a given threshold ϵ, that is:

  $$||i_t - i_{t+1}||_\infty = \max |i_t(x,y) - i_{t+1}(x,y)| < \epsilon$$

  We notice the reader that this criterion only holds when the error in the numeric implementation is negligible. By the considerations of the former Section, RCF

supports this criterion in the case of evolving the signed distance map and, to some extend, low noisy binary images. When numerical errors are difficult to estimate a priori, a more sensible criterion is:

- Criterion B (critB): *Constant Speed Value Criterion.* The iterative process should stop when the magnitude of the speed stabilizes. We consider a magnitude is stable in time when its derivative is under a given threshold, ϵ, in a time interval of a given length T. That is, we stop the evolution at the time T_0 such that $||speed_t - speed_{t+1}||_\infty < \epsilon$ for $t \in [T_0, T_0 + T]$. In the discrete version, the length T converts to a given number of iteration steps, it, via the formula:

$$T = it \cdot \Delta t$$

This criterion is frequently used in iterative schemes prone to oscillate around the equilibrium state, such as snakes [12] or minimizing processes. In the particular case of energy minimization or zero finding, the former stop criteria are also applied to the functional value on the current iteration.

For diffusion processes ([60], [72]), the value *speed* is the divergence term of the PDE we are integrating, for the geometric flows [32], [49], [79] it is the curvature term. For RCF, because the evolution seeks a zero of g, we will apply the stopping criteria to the roughness measure. Maximums will be taken over the whole image in the case of diffusion filtering and over a target curve (representative of the image features) in the case of curvature dependent methods.

Two different kinds of experiments are presented:

• Tests on synthetic images with added noise in order to compare RCF to other PDE-based techniques and determine which ones achieve a better compromise between quality of the restored image and stabilization of the iterative process.

• Performance of RCF in real image filtering and applications to shape recovery.

5.1.2 Experiment I. Comparison to other Filtering Techniques

The methods tested are the Perona-Malik Model (PMM) [60], the Anisotropic Diffusion (AD) method [72], the Mean Curvature Flow (MCF) [32], the Min-Max Flow (MMF) [49] and the Stochastic Geometric Flow (STF) [79]. The time step in the Euler scheme chosen is $\Delta t = 0.1$ for diffusion processes and $\Delta t = 0.4$ for curvature flows.

Methodology of Comparison

We consider that assessment of performance should take into account quality of the restored image as well as the criterion used to decide when the method has reached its best restoration. Quality of the restorations will be measured with the standard quantities:

1. Signal to Noise Ratio (SNR):

$$SNR(I_0, I_{ev}) := 10 log_{10} \left(\frac{\sigma^2(I_{ev})}{\sigma^2(I_0 - I_{ev})} \right)$$

where I_0 denotes the original image and I_{ev} the evolution of the noisy image. The higher it is, the more quality the restored image has.

2. Contrast to Noise Ratio (CTN). This quantity measures the edge preserving rate of the method. It is defined as the

   ratio between the difference of means in the interior (μ_{int}) and exterior (μ_{ext}) of the object of interest and the variance in the exterior (σ_{ext}) of the object of interest:

$$CTN(I) := \frac{|\mu_{ext}(I_{ev}) - \mu_{int}(I_{ev}))|}{\sigma_{ext}(I_{ev})}$$

The issues followed to select the best performer are:
- *Contrast preserving capabilities and overall quality in image restorations.*
- *Convergence to non-trivial steady states*
- *Smooth convergence and stabilization of the iterative process*
- *Robustness to high noise and the embedding Image.*

We have chosen a non-convex M-shape and a circle corrupted with a 50% of uniform noise and a gaussian noise of $\sigma = 0.5$. Any shape reconstructions are obtained applying a threshold of value 0.5 to the filtered images.

Step 1: Best Restorations

Figure 5.1 displays results for the M-shape and figure 5.2 for the circle. Best performances (second columns for uniform noise and third for gaussian one) correspond to the images achieving the best SNR. The number of iterations necessary to reach these images is displayed underneath. Shapes recovered (first columns), correspond to uniform noise, for the M-shape, and gaussian noise, for the circle.

The visual quality of the restored images (fig.5.1 and fig.5.2) is similar for all methods. Background artifacts in some images filtered with RCF are common to all geometric flows. Geometric flows are designed to smooth curves rather than images, therefore they are always prone to produce funny patterns in noisy backgrounds. This is not a main inconvenience if the aim of the filtering procedure is to restore a shape, which is the natural application of geometric flows. In fact, all reconstructed shapes have similar quality, matching the original templates. In the case of STF the circle hexagonal-like appearance could be improved by increasing the number of vertices of the final STF state.

We note that the number of iterations needed to achieve optimal restorations varies with noise.

Step 2: Asymptotic Behavior

Evolution of quality measurements in time (fig.5.3-5.5) reflects convergence to non trivial steady states as well as resemblance between original and evolved images. Final states after 3000 time units are overimpressed on the graphics of fig.5.5.

Plots corresponding to techniques that converge to non-trivial steady states (RCF, MMF and, to some extend, STF) asymptotically tend to a positive number (the final image SNR/CTN value). Meanwhile graphics of methods yielding trivial images (AD,

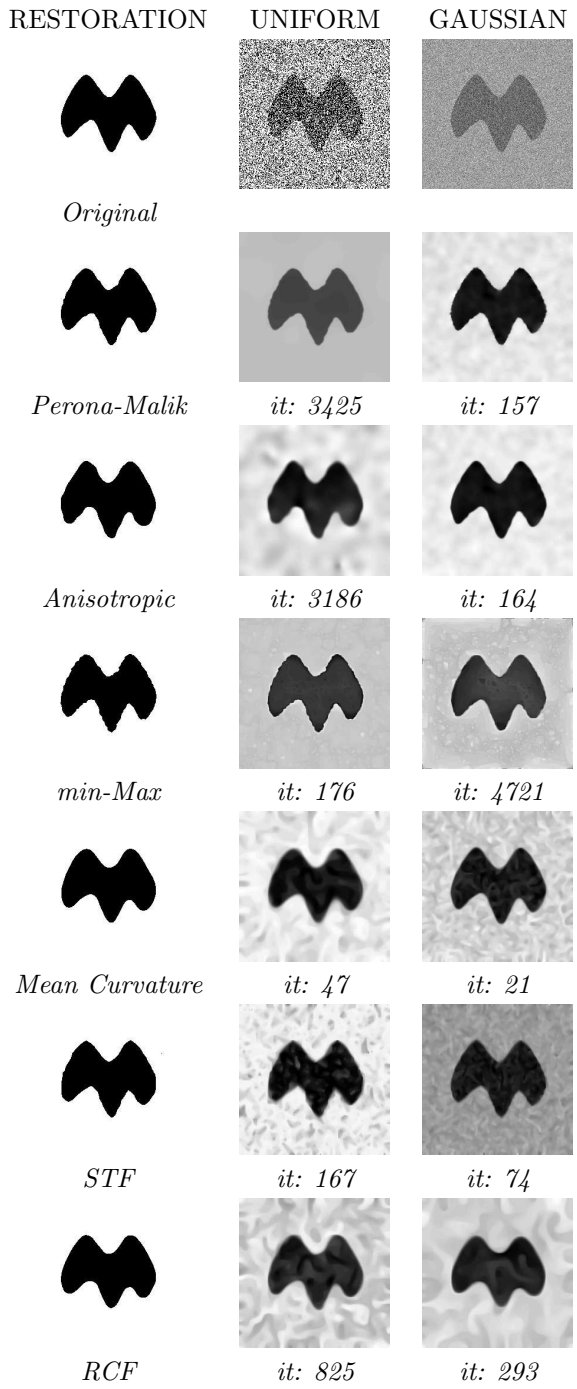

Figure 5.1: M-shape Best Reconstructions.

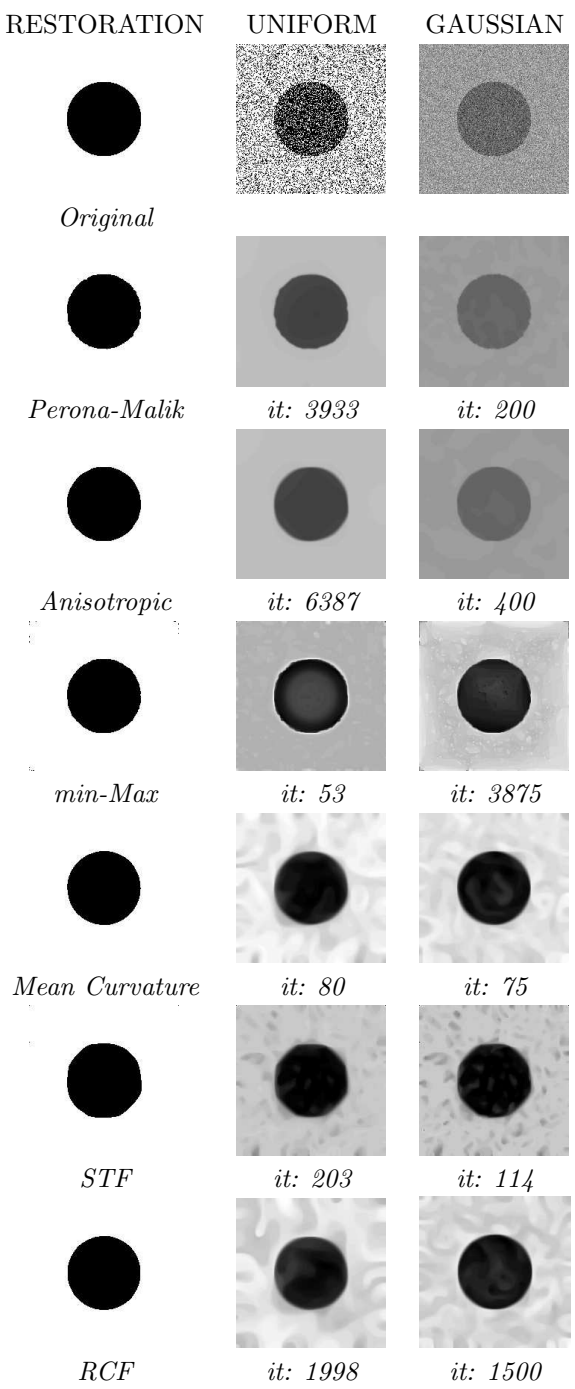

Figure 5.2: Circle Best Reconstructions

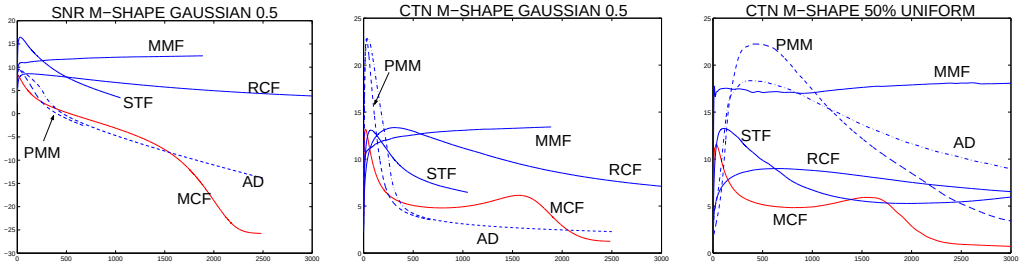

(a) (b) (c)

Figure 5.3: M-Shape Quality Numbers Graphics

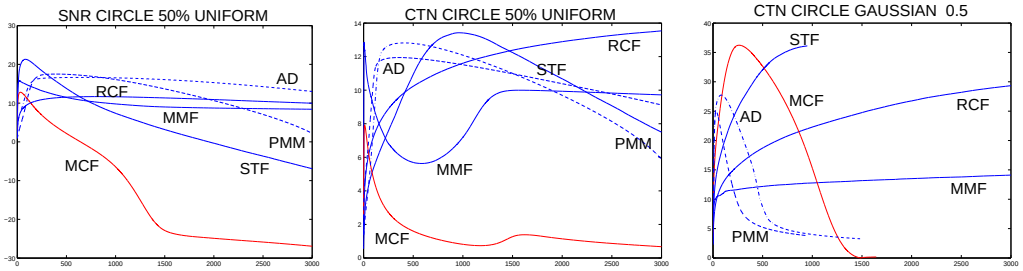

(a) (b) (c)

Figure 5.4: Circle Quality Numbers Graphics

PMM, MCF) present a maximum and then tend to zero at a rate related to the speed of convergence.

Diffusion processes (AD, PMM) fail to maintain quality numbers, especially for CTN values (fig.5.3, 5.4 (b), (c)). The decay is more significant in the measure noise increases and is more prominent in the case of gaussian noise. Geometric flows are more robust against the nature of noise and are more sensitive to the geometry of the underlying shape (see CTN graphics in fig.5.3 (b), (c) and fig.5.4). As expected, MCF is, by no means, the worst performer, especially when non-convex shapes are evolved (fig.5.3, fig.5.5 (a)). Among all techniques, RCF and MMF graphics are the only ones that match, for all cases, the model of a non-trivial steady state. Final images in fig.5.5 reflect quality numbers stability.

Because *Step 2* discards MCF and PMM, *Step 3* will only be applied to AD, MMF, STF and RCF.

Step 3: Evolution Stabilization

The stopping parameters are $\epsilon = 10^{-3}$ for critA and $\{\epsilon = 10^{-4}\ T = 100\}$ for critB. We will keep the former stopping values for the remains of the paper. In order to produce an experiment as balanced as possible, we have tried the criteria on the gaussian noisy M-shape and the uniform noisy circle.

Figures 5.6 and 5.9 plot evolution speeds and RCF roughness measure versus time

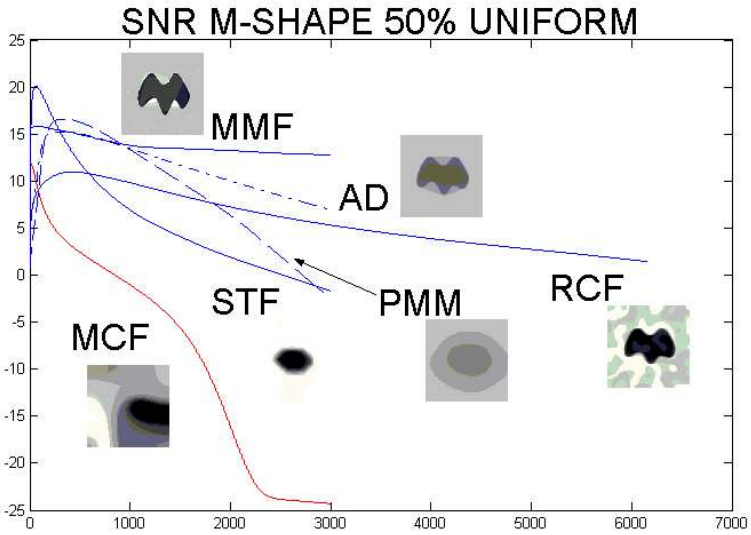

(a)

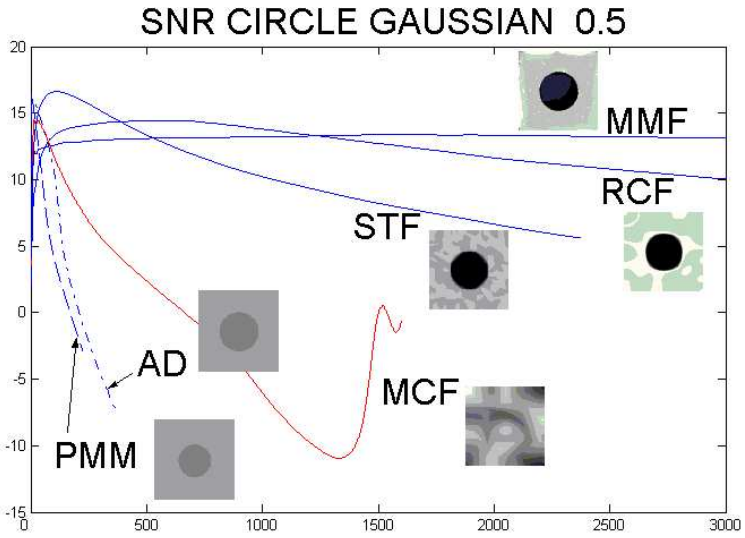

(b)

Figure 5.5: Asymptotic behavior in terms of SNR: (a) uniform noisy M-shape and (b) gaussian noisy circle

in the case of gaussian and uniform noise, respectively. Images stabilized using critA are shown in fig.5.7, 5.10 and those achieved with critB in fig.5.8 and fig.5.11.

Standard numeric stabilization techniques ([18], [70]) need either an accurate implementation (CritA) or a smooth process (CritB). Speed graphics assess their appli-

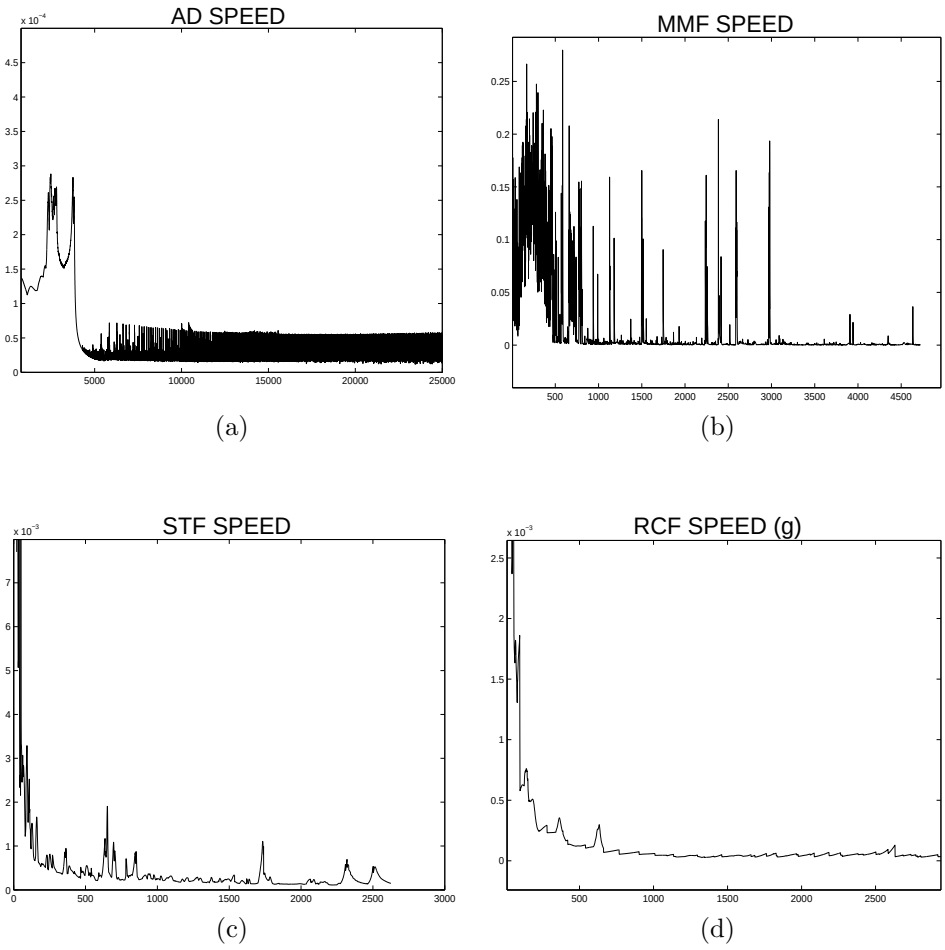

Figure 5.6: Speed Graphics for gaussian noise on the M-shape

cability. If they asymptotically converge to zero, both criteria are valid, CritA is still applicable if plots just tend to zero, while CritB is satisfied for speeds asymptotically converging to a (positive) value. It follows that oscillating or irregular speeds difficult stopping the iterative process.

Both AD and MMF speeds (fig.5.6, fig. 5.9 (a) and (b), respectively) are of an oscillating nature and present a significant lack of smoothness (especially in the case of MMF). This makes critB fail to stabilize the evolution in most cases. Images in fig.5.8 and fig.5.11 (a) correspond to AD final state and fig.5.8 (b) to MMF final state for the gaussian case. Only in the case of uniform noise MMF stabilized using critB (fig.5.9(b)). Regularity of STF speed (fig.5.6 and fig.5.9 (c)) is just on the edge of critB applicability, so that a large time interval T fails to stabilize the evolution. This is a main inconvenience because STF slow noise removal rate makes critB yield images that may not be completely clean (fig.5.8 (c)). On the other side, RCF roughness

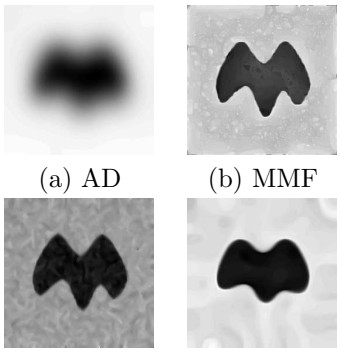

(a) AD (b) MMF

(c) STF (d) RCF

Figure 5.7: Criterion A

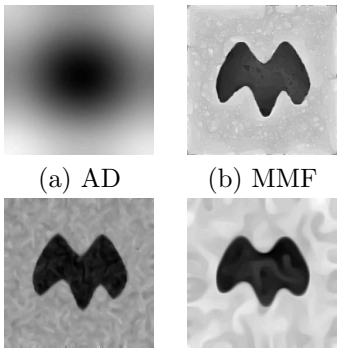

(a) AD (b) MMF

(c) STF (d) RCF

Figure 5.8: Criterion B

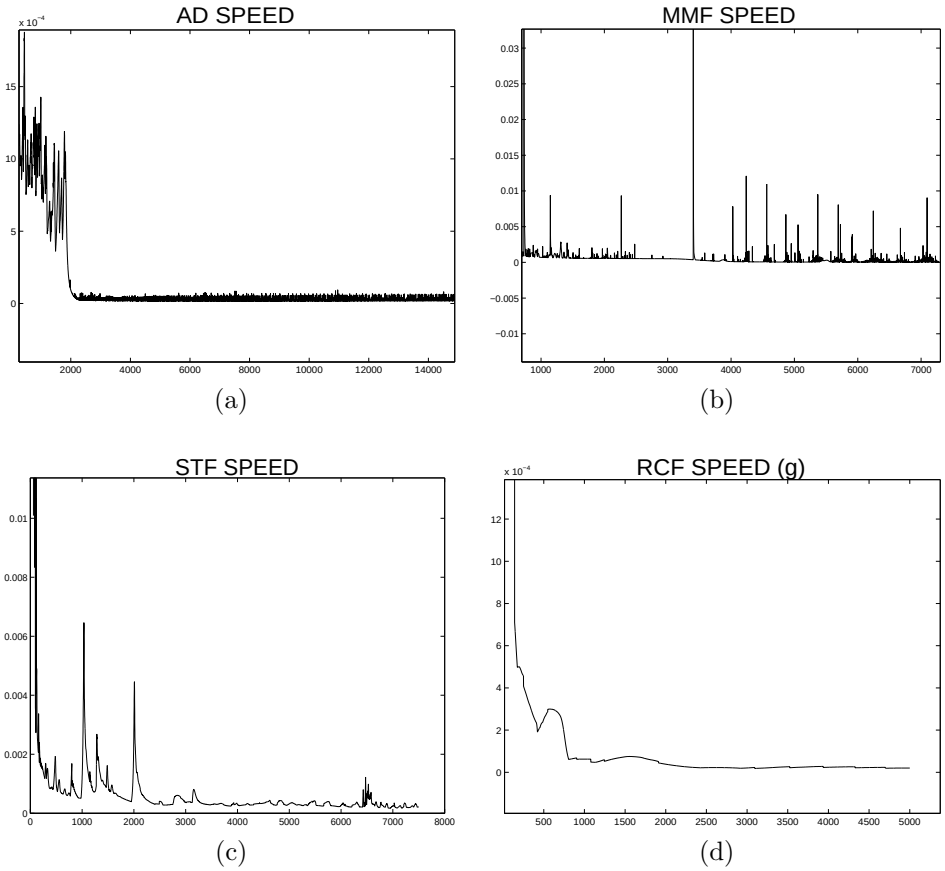

(a) (b)

(c) (d)

Figure 5.9: Speed Graphics for uniform noise on the circle

measure (fig.5.6 and fig.5.9 (d)) presents a smooth enough asymptotic behavior as to apply critB without strict restrictions. Besides, since RCF is a good noise remover, images in fig.5.8 and fig.5.11 (d) are close to the ones getting best quality numbers in fig.5.1 and fig.5.2.

For all methods, round-off errors in combination with the method behavior difficult success of critA. In the case of AD, rapid convergence to a constant image makes critA stop the evolution at too blurred images (fig.5.7(a)). For MMF, critA reveals to be efficient to stabilize images (fig.5.7, 5.10 (b)), although they may be far from final states because of evolution irregularity. Images obtained with STF present similar anomalies than those achieved with critB. The compromise between noise removal and shape preservation may not be achieved with a fixed ϵ. It follows that the M-shape image (fig.5.7 (c)) still presents background noise, while the circle of the clear image in fig.5.10 (c) starts differing from the theoretical final hexagon that, according to [79], should be the one of maximum size inside the circle. Finally, numeric errors induced by the embedding image may over-erode shapes smoothed with RCF (fig.5.7, 5.10 (d)).

For assessment of quality of the restored shapes in the case of highly noisy images, we will use critA for MMF, STF and critB for RCF.

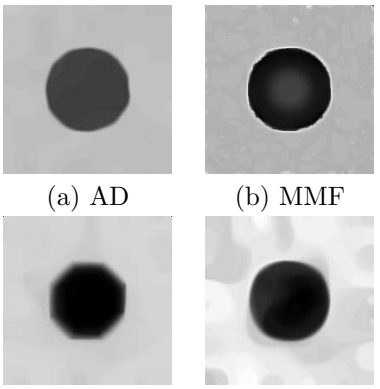

(a) AD (b) MMF

(c) STF (d) RCF

Figure 5.10: Criterion A

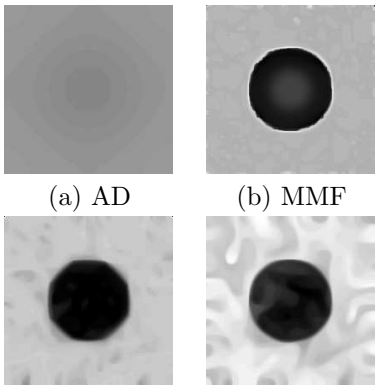

(a) AD (b) MMF

(c) STF (d) RCF

Figure 5.11: Criterion B

Step 4: Robustness

In order to assess robustness, we have corrupted the M-shape with a gaussian noise of parameters $\mu = 0.5$, $\sigma = 1$ (fig.5.12 (a)) and a 70% of uniform noise (fig.5.12 (e)). We have chosen a gaussian noise of positive mean in order to determine the dependence of each of the methods on the gray-level, α_0, defining the curve of interest. We recall that this value is inherent to MMF formulation, as it switches between evolution by negative and positive curvature, while RCF only uses the parameter in its numeric implementation.

Images filtered are in fig.5.12 and the model of shapes restored in fig.5.13. Images filtered with RCF (fig.5.12(d), (h)) are prone to present more background arti-

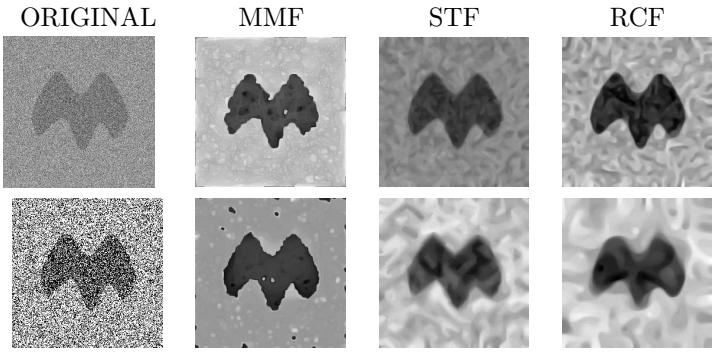

Figure 5.12: Highly noisy M-shape, 1st row gaussian and 2nd uniform

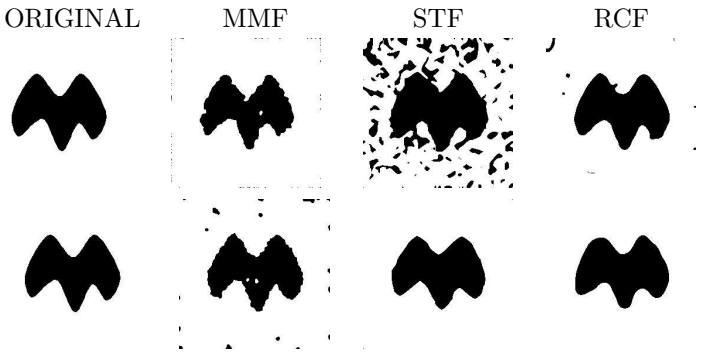

Figure 5.13: Shapes for high noise, 1st row gaussian and 2nd uniform

facts than those that MMF yielded (fig.5.12(b), (f)). However, reconstructed shapes (fig.5.13(d), (h)) are more accurate and smoother for RCF filtered images. Shapes obtained with MMF (fig.5.12(b), (f)) still present irregularities and those obtained with STF may hardly resemble the original ones because of an insufficient noise removed.

The higher irregularity in MMF reconstructions for gaussian noise, reflects its undesirable dependency on the gray-level α_0. In the case of RCF, dependency reduces, in the worst case, into an over erosion of the target shape.

We conclude that not only is our method the one achieving the best compromise between quality of restored image and evolution stabilization, but also the best suited for a non-user intervention application.

5.1.3 Experiment III. Application to Image Filtering and Shape Recovery

This part is devoted to results on real images obtained with RCF and the geometric flows MMF and STF. On one hand, experiments should serve to clarify some of RCF numerical aspects (stopping parameters and speed over target curves). On the other hand they should show those cases where RCF has advantages over MMF and STF.

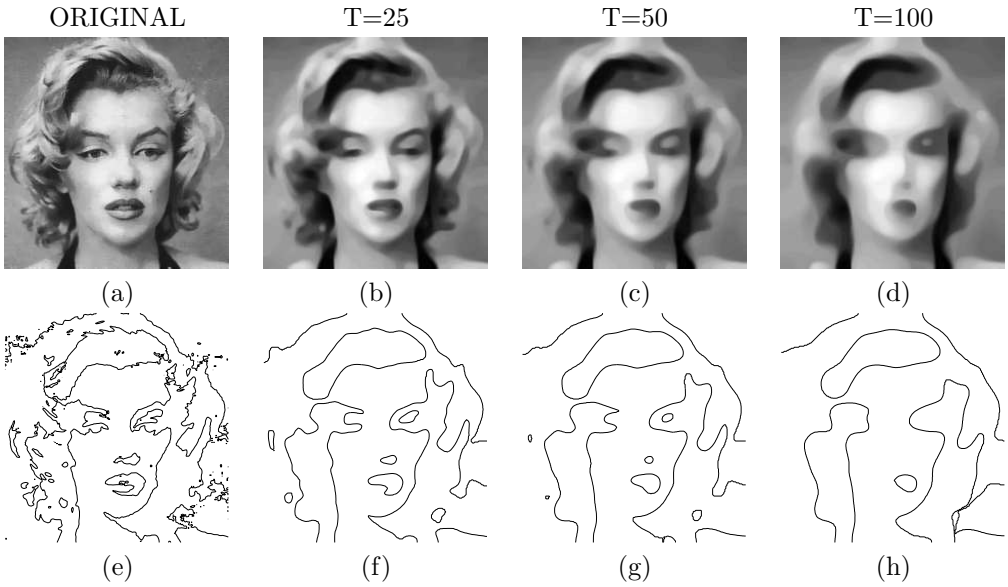

Figure 5.14: Stop parameters impact on RCF filtering of Marilyn, gray-level images are in 1st row and descriptive level set in 2nd one

The following set of real images has been tested:

Faces and Real Objects

The portrait of Marilyn (fig.5.14 (a)) will serve to illustrate the role of T in RCF numeric scheme. We run RCF with $\epsilon = 10^{-3}$ and $T = 25, 50, 100$. Figure 5.14 displays the Marilyn's gray-level images (first row) and the target level curve (second row). Images stabilized with the shortest time intervals (fig.5.14 (b), (c)) keep the most descriptive facial features (eyes, mouth and nose), while spurious details in the hair have been removed (see curves in fig. 5.14 (f), (g)). Besides, although the smoothest Marilyn image (fig.5.14 (d)) may seem rather eroded, the essential facial features are still identified in the target curve (fig.5.14 (h)).

We have chosen the buildings of fig.5.15 (a), (e) for our first comparison between RCF, MMF and STF. Because of their different geometric designs, they will illustrate capability of each of the methods to retain shape models in practical applications. The squared shaped arch of fig.5.15 (a) is perfectly kept by MMF (fig.5.15 (d)) and, though a bit rounder, by RCF (fig.5.15 (b)). Although we used the same parameters than in [79], rectangles have almost disappear in the STF image (fig.5.15 (c)). In the case of fig.5.15 (e), oval arch nicely appears in all filtered images fig.5.15 (f), (g) and (h). Although the ones in RCF image (fig.5.15 (e)) are sharper than in MMF smoothed building (fig.5.15 (g)) and smoother than in STF image (fig.5.15 (f).

Speed plots in fig.5.16 correspond to the building in fig.5.15 (e). Quantities have been computed on the whole image (1st row) and on the level set that best describes the geometry of the building (2nd row). In all three geometric flows, graphics for the

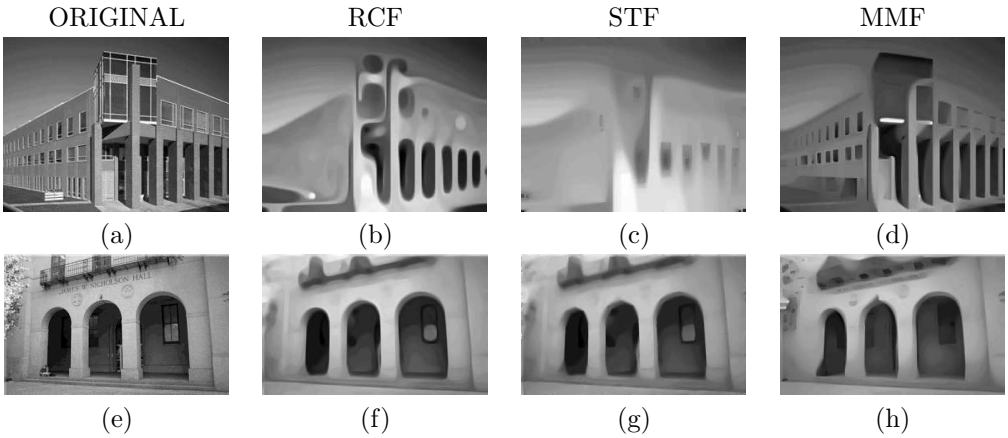

Figure 5.15: Buildings filtering

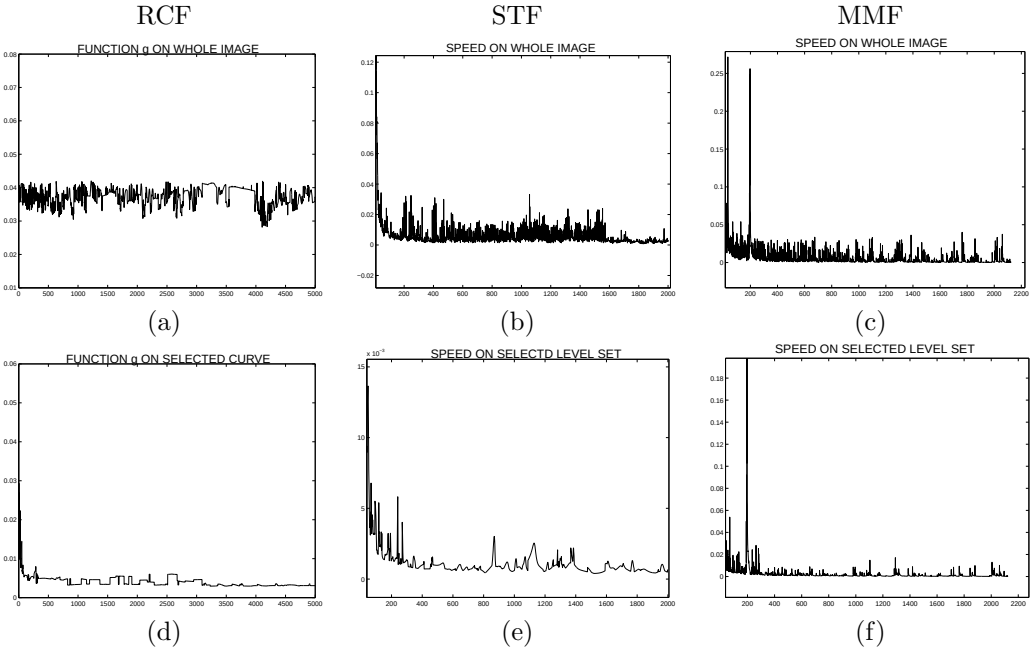

Figure 5.16: Speeds on whole image (1st row) and on selected curve (2nd row) for (a), (d) RCF, (b), (e), STF and (c), (f) MMF

selected curve are smoother in time, which motivates using the latter for evolution stabilization. We note that graphics reflect the error in RCF implementation (Section 2.5): peaks in fig.5.16(d) correspond to the error introduced by the collapsing of a small level curve.

The second comparison on the car plate of fig.5.17(a) shows the contrast preser-

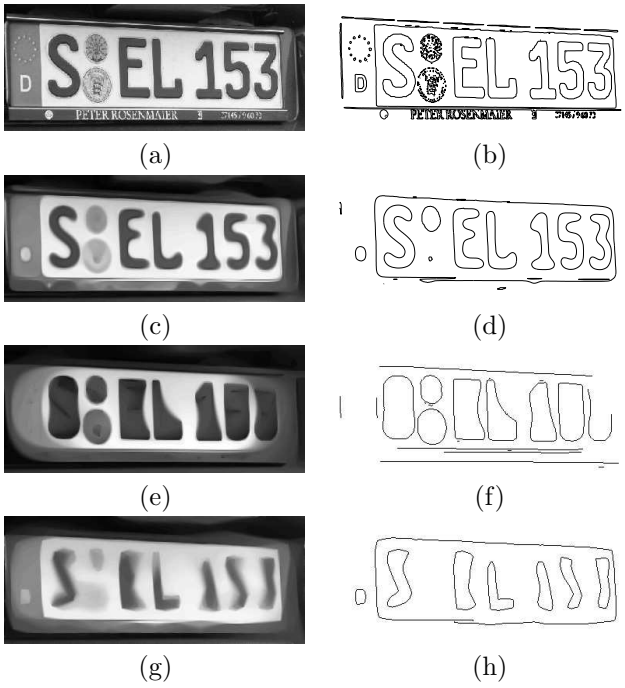

Figure 5.17: Filtering of plate:(a), (b) original, (c), (d), RCF (e), (f) MMF and (g), (h) STF

vation of geometric flows and RCF higher efficiency for shape restoration. Curves in the 2nd column correspond to image canny edges. We argue that the filtering should preserve image sharpness and regularity of the numbers and letters borders (fig.5.17 (b)), while superfluous details (small letters at the plate bottom and stamps) and noise that may mislead a latter segmentation process should be removed. First notice that all three geometric flows stabilize images (fig.5.17 (c), (e) and (f)) with contrast changes equal to the original. Edges (fig.5.17 (d)) of RCF final image yield plate numbers that, though a bit smoother, perfectly match the original ones. Meanwhile, edges extracted from images stabilized with MMF and STF (fig.5.17 (f), (h)) are over-smoothed and the geometry (and even topology) of the resulting numbers is significantly different.

Application to Medical Images

We have applied our technique to segment the luminal area in intravascular ultrasound sequences (IVUS) [25]. Since the grey level of ultrasound images expresses the material impedance, black pixels correspond to blood and white ones to tissue. The aim was to obtain a model of the artery reflecting its geometry by means of a procedure requiring the minimal manual intervention as possible. Artifacts caused by blood flow and the speckled nature of ultrasound images force some kind of smoothing of the level surfaces. RCF has been applied to cross sections and longitudinal cuts using

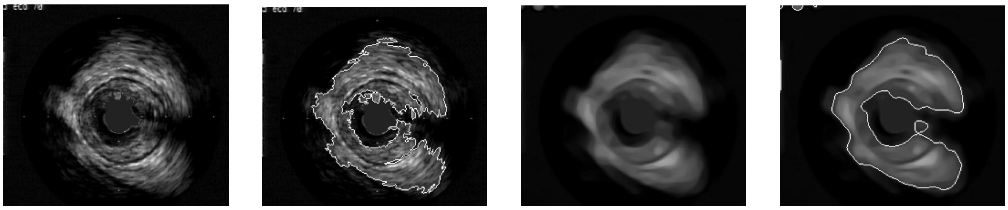

(a) (b) (c) (d)

Figure 5.18: Cross Sections of IVUS sequences. Original IVUS images (a) and segmenting curve (b), steady state attained with RCF (c) and the resulting segmenting curve(d).

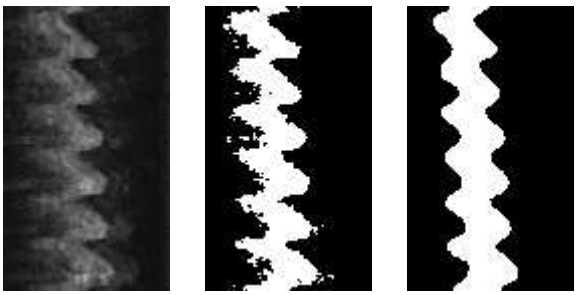

(a) (b) (c)

Figure 5.19: Longitudinal cut of IVUS (a), shape segmenting blood and tissue in (b) the original cut and the smoothed shape with RCF (d).

the speed stabilization criterion over the level curve that best segments blood and tissue.

Figure 5.18(a) shows a cross section of an IVUS sequence and fig.5.18 (b) the level curve that separates blood from tissue. The inner border corresponds to the curve segmenting blood and tissue. The image achieved by RCF is displayed in fig.5.18 (c) and the corresponding segmenting curve in fig.5.18 (d). Notice the way RCF-smoothed curve captures the characteristic features of the curve in fig.5.18 (b), such as the small oval in its inner border. Figure 5.19 shows a longitudinal section (fig. 5.19(a)) and the binary image (fig.5.19 (b)) that represents the segmenting curve. The wavy shape, characteristic of IVUS longitudinal cuts, reflects cardiac motion and is of clinical interest, meanwhile small irregularities are caused by blood turbulence. The model recovered by RCF is a smooth shape (fig.5.19(c)) that keeps the same number of undulations than the original cut.

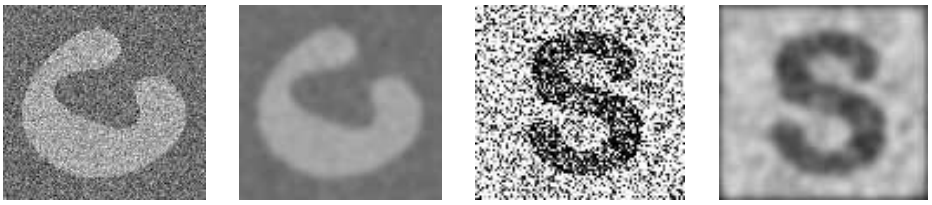

(a) (b) (c) (d)

Figure 5.20: Test Set 1. Noisy images: non convex shape (a), smoothed image (b), character 'S' (c) and smoothed image (d).

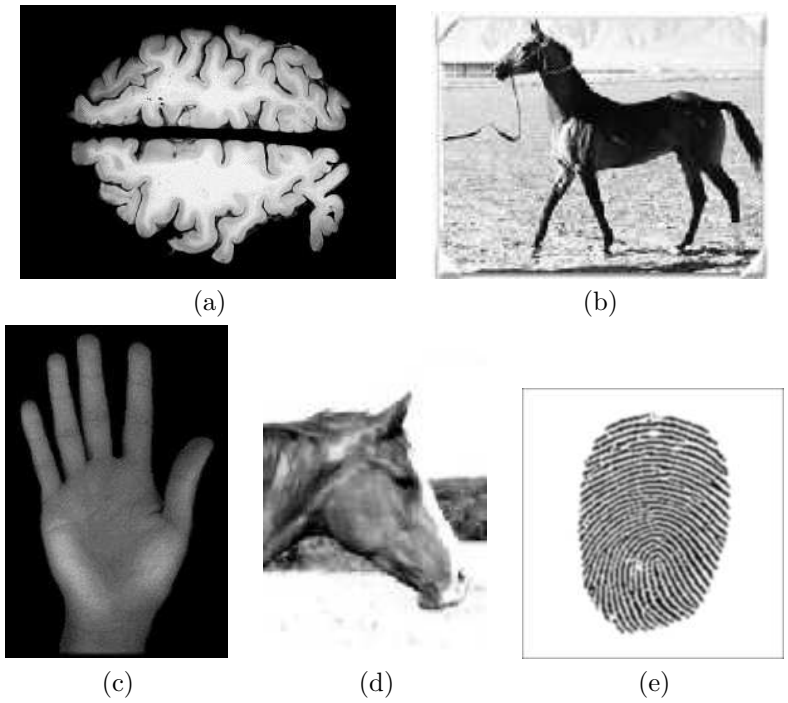

(a) (b)

(c) (d) (e)

Figure 5.21: Test Set 2. Real images: human brain (a), horse (b), hand (c), horse head (d) and fingerprint (e).

5.2 Anisotropic Contour Closing

In this experimental section, we will show the accuracy of the shapes recovered by ACC using dynamic Coherence Vector Fields to guide the restricted extension process. Because we have embedded contour closing in the context of shape restoration oriented to object segmentation, ACC will be applied to contours extracted from real images and synthetic noisy images. Figure 5.20 shows the noisy shapes, a croissant-like curve

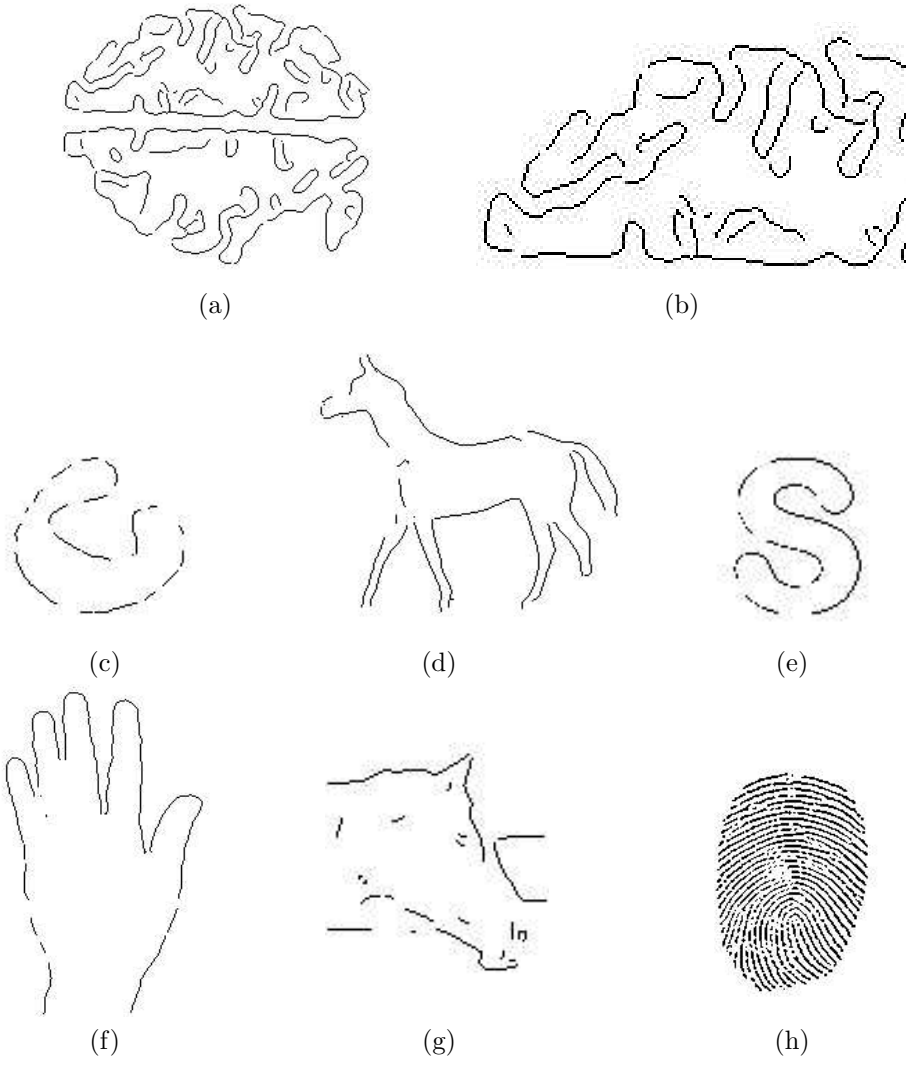

Figure 5.22: Uncompleted contours.

corrupted with gaussian noise (fig.5.20(a)) and a character 'S' with uniform noise added (fig.5.20(c)). Meanwhile the set of real images is displayed in fig.5.21.

The different image features used to select points (contours in fig.5.22) lying on the objects of interest are edges, ridges and gray level. We have chosen the following standard algorithms to compute them: Canny for edges, curvature for ridges and gray-level thresholding. To reduce the impact of noise and textured backgrounds, all images have been previously smoothed with a gaussian filter of $\sigma = 2$. For noisy images, contours correspond to edges of the smoothed images of fig.5.20(b), (d); for the

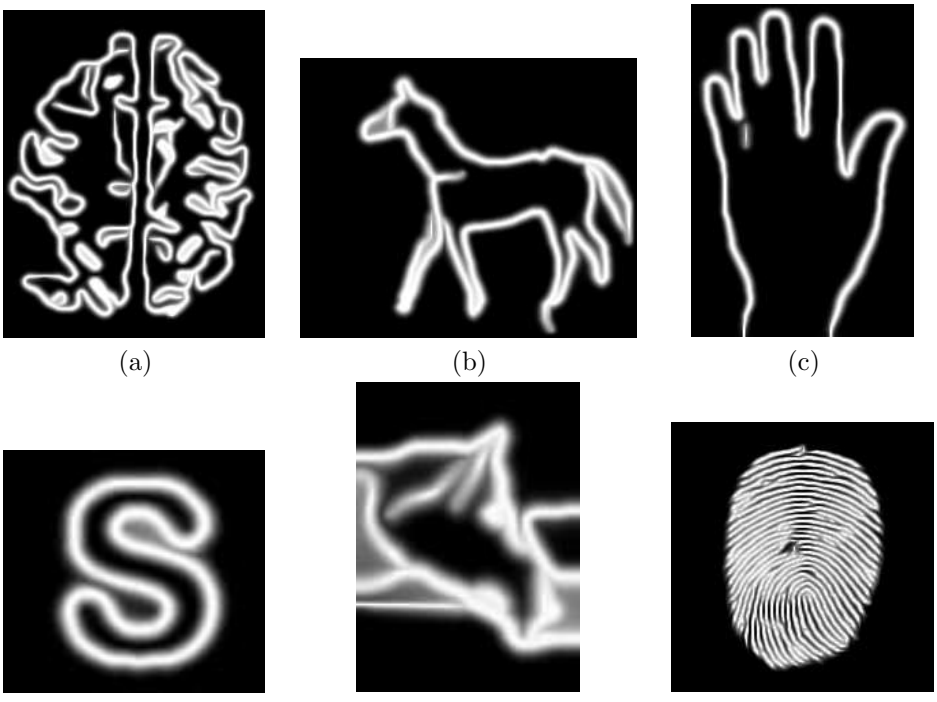

Figure 5.23: Extensions of brain (a), horse (b), hand (c), 'S' (d), head (e) and fingerprint (f).

real images of fig.5.21(a)-(e), we used edges in combination with pixel gray level in the brain image and for the fingerprint in fig.5.21(f), image ridges. The contours obtained, shown in fig.5.22, include cases deserving special care, such as corner restoration (horse ears in fig.5.22(d), (g) and finger joints in fig.5.22(f)) and dense lines prone to merge (fingerprint in fig.5.22(h)).

The numeric scheme used to compute solutions to (4.3) is an explicit Euler scheme for non-linear heat equations stabilize by means of the stop criterion critB given in Section 5.1.1. The parameters used in the computation of the coherence vector fields are an integration scale $\rho = 2$ and a regularization scale $\sigma = 0.5$. In the case of large gaps (fig.5.22 (e), (g)) vector fields are dynamically updated every 300 iterations. We have used the ridgeness measure described in [45] to compute the ridges of the extension that yield the curve closure and serve to update vector fields. According to the theoretic analysis given in Section 4.2.1, distance based vector fields properly recover a model of corners and linear fields avoid merging in the contours to complete. Therefore, for the sake of a maximum accuracy and reliability in the closed models, we have chosen the distance based DVF for restoration of contours in fig.5.22(a)-(h) and a linear LVF closing in the case of the fingerprint (fig.5.22(i)).

The final states achieved are the characteristic functions representing the recon-

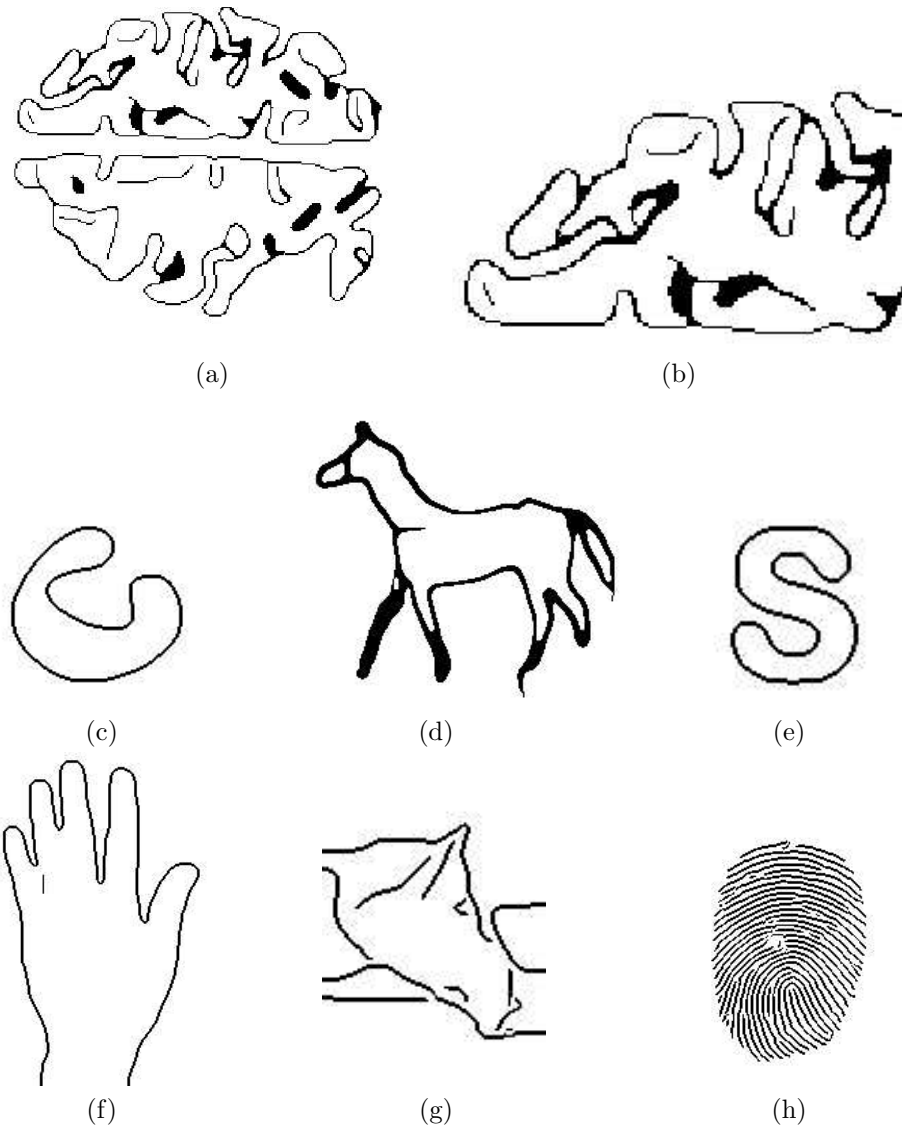

Figure 5.24: Reconstructed contours using DVF (a)-(g) and LVF (h).

structed shapes shown in fig.5.23 and their ridges yielding contour closures are displayed in fig.5.24. In the case of smooth contours, such as the noisy images (fig.5.20) and the hand (fig.5.21 (c)), ridges of the extensions are continuous lines that constitute accurate curve models (fig.5.24(c), (d), (f)). However, T-junctions produce discontinuous ridges so that reconstructions of the brain and horse (fig.5.24(a), (e))

were extracted via a morphological thinning of a thresholded version of the extensions.

Because it is based on the distance map to the open contours, closings achieved using DVF recover shape curvatures, such as the concave part of the non-convex contour in fig.5.24(c) and the character 'S' in fig.5.24(e). Besides it properly closes the acute angles of the horses ears (fig.5.24(d), (g)) and the hand finger joints (fig.5.24(f)). We may draw the reader attention towards the closures of the brain ridges, better appreciated in the detail of fig.5.24(b), for an example of DVF accuracy. Merging in the case of the horse ear and tail is a result of the way (thinning) contours are extracted. On the other hand, thanks to its linearity, LVF fingerprint closure does not merge line ends at the boundary and yields an accurate closure because of a small gap size without acute angulation.

5.3 Modelling Shapes with the Curvature Vector Flow

In this section we apply CVF to smooth shape representation with its application to object segmentation in combination with ACC. In order to assess the proposed segmenting strategy, two different experimental issues should be addressed. First, we will check accuracy of shape models attained with CVF, that is, its capability of adapting a snake to non-convex shapes. Second, quality in the segmentation of real images will be compared to results using geodesic snakes.

5.3.1 Shape Representation

Given a closed curve in the plane, a compact way of representing it is through an approach by means of a parametric B-spline snake. We recall the reader that a parametric snake [38] is a curve $\gamma(u) = (x(u), y(u))$ that minimizes the energy functional:

$$E(\gamma) = \int_{\gamma} (E_{int} + E_{ext})du = \int_{\gamma} (\alpha||\dot{\gamma}||^2 + \beta||\ddot{\gamma}||^2 + E_{ext})du \ ,$$

where the external energy depends on the image object to model and can be either a distance map or a function of the original image gradient. The parameters α and β determine the stiffness of the deformable model and are in the range $[0, 1]$. In any case the optimal curve is obtained by means of the Euler-Lagrange equations associated to E, which are equivalent to solving a linear system:

$$Ax = -\nabla E_{ext} \ .$$

The numeric iterative scheme is given by:

$$x_{t+1} = (A + \lambda I)^{-1} (\lambda x_t - \nabla E_{ext})$$

where I denotes the identity matrix, A the stiffness matrix [38] and λ is a viscosity parameter. An important remark is that stability of the finite difference scheme depends upon the viscosity parameter, which must be increased if α, β decrease. This viscosity parameter determines the speed of convergence, the higher it is, the

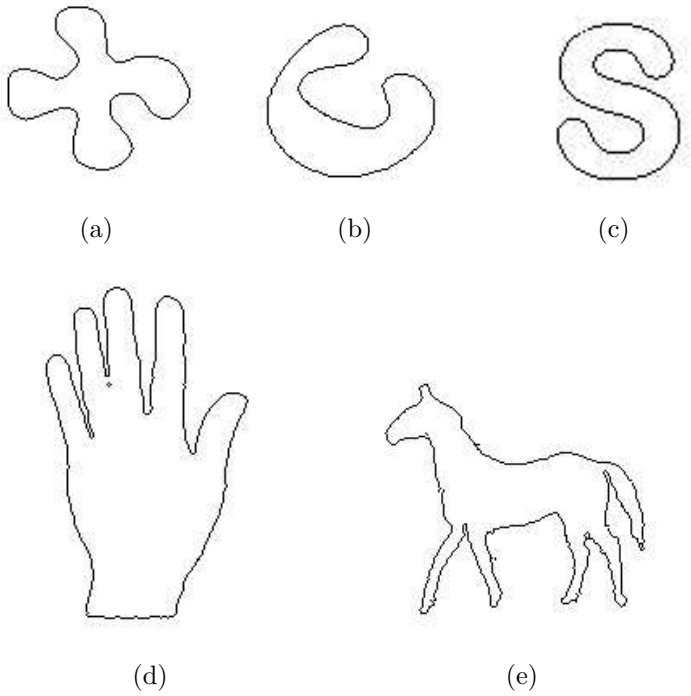

Figure 5.25: Set of test shapes: clover (a), highly non-convex curve (b), character 'S' (c), hand (d) and horse (e).

slower the snake converges. We consider the snake has reached its final state when its total energy stabilizes.

Experiments focus on the efficiency and accuracy of CVF when non-convex contours are modelled. Accuracy has been computed in terms of snake convergence, given by the snake maximum Euclidean distance to the original closed contours. Efficiency is given by the CPU-time the initial snake takes to reach its final state. Since the stop criterion is in terms of the stabilization of the external energy, the asymptotic behavior of the functional E is also a measure of the method efficiency. An oscillating graph for E hinders stopping the deformable model with the former stop criterion and the final snake must be obtained after a fixed number of iterations.

We have tested the external potentials for different values of the snake parameters, α and β, in order to check if the energies could support large values and still guarantee convergence of the snake to the curve of interest. As noticed before, supporting large values for α, β is also a signal of efficiency, since the larger these parameters are, the faster the snake converges. The snake has been initialized inside and outside the object of interest. We have compared CVF to the results obtained using a GVF-regularized gradient of the Euclidean distance map (DM) and GVF applied to the edge map.

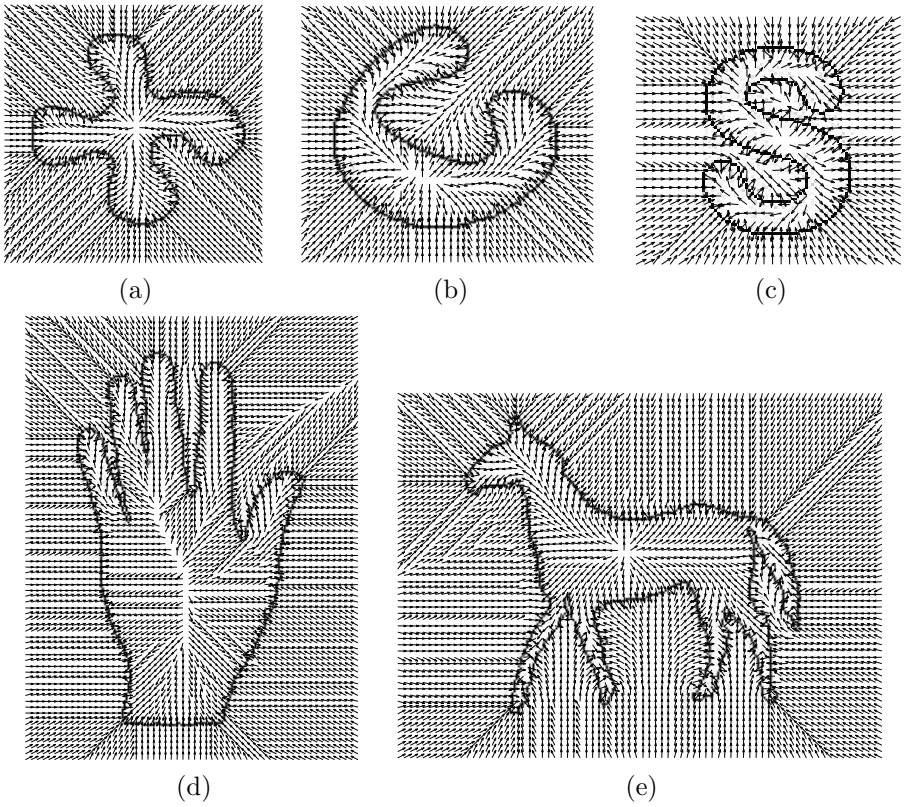

Figure 5.26: CVF on clover (a), highly non-convex curve (b), character 'S' (c), hand (d) and horse (e).

The shapes chosen are depicted in figure 5.25. The external force given by CVF is shown in figure 5.26. Convergence of snakes for the different external forces is shown in figure 5.29 and the final model obtained is depicted in figure 5.30.

In terms of an accurate model of the shape, CVF is the only external energy that adapts the deformable model to all curves, whatever position (inside or outside the object of interest) of the initial snake. The other two external energies fail to obtain an accurate model when the initial snake lies inside the object of interest. Convergence to the character 'S' and horse in fig. 5.29 and the final shapes of fig. 5.30 illustrate this bad-pose of the snake inner convergence with GVF and DM. In the case of the character 'S', saddle points of both GVF and DM, make the snake oscillate at closed shapes which fail to reach the extremal boundary of the 'S'. Irregularities in the gradient of the horse external energy, produces open final snakes (fig. 5.30(b),(c)) approaching only a part of the animal's contour. Notice the accuracy and smoothness of the final model of the horse achieved with CVF (last row of fig. 5.30(a)). In the case of an outer initial snake, GVF succeeds in adapting to non convex shapes such that the angle θ does not turn more that π between two consecutive inflexion points

(like the clover of fig. 5.30(b)). However the snake gets trapped at the saddle points that highly non convex shapes (second row of fig. 5.30(b)) produce in the vector field. The external force field obtained by a regularization of the gradient of DM using GVF is the worst performer. Even for small values of α and β, the external force is not strong enough to attract the snake to non-convex shapes, even in the case of shapes (like the clover of fig. 5.30(c)) with the angle θ turning less than π between two consecutive inflexion points. Figure 5.27 summarizes these results in the form of maximum Euclidean distance to the contour of interest versus number of iterations. Notice significant differences of the maximum distance between CVF and DM/GVF in the case of convergence to highly non-convex shapes (fig. 5.27 (a),(c)).

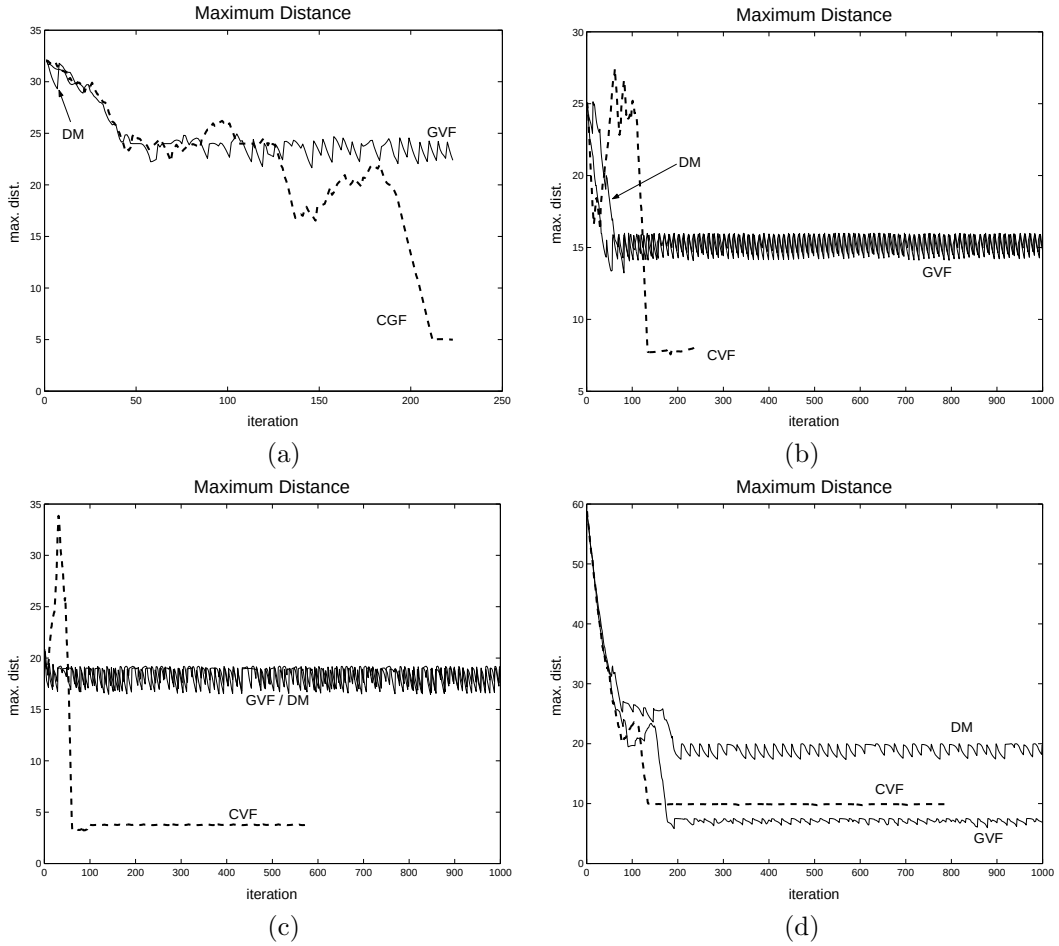

Figure 5.27: Snake accuracy, interior convergence for highly non convex shape (a) and the clover (b) and the corresponding exterior convergence (c) and (d)

Concerning efficiency, CVF is, again the best performer, since attains accurate

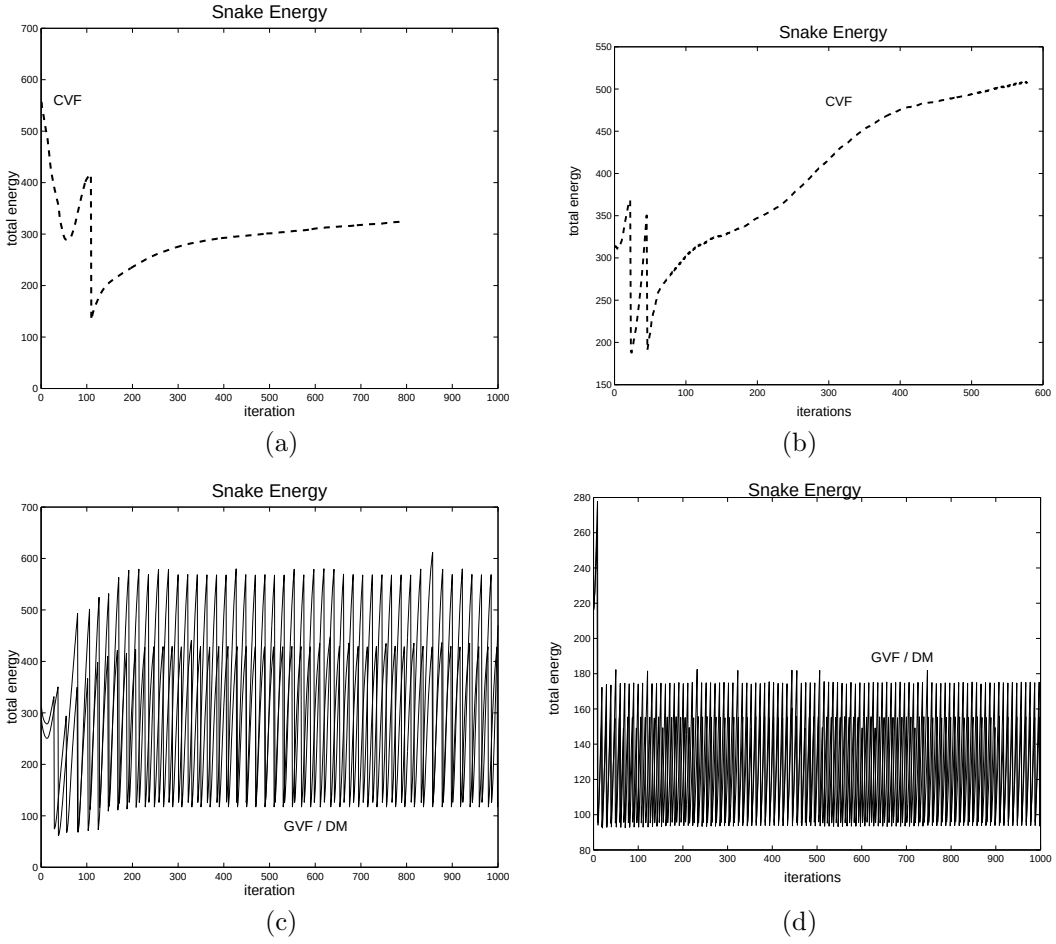

Figure 5.28: Evolution of snake energy, CVF exterior convergence for highly non-convex shape (a), the clover (b) and the corresponding GVF/DM convergence (c) and (d)

models in optimal time, meanwhile GVF is the worst of the methods. Times for DM have not been taken into account since the method does not produce good enough segmentations as to be taken into account. The main reason for this difference in times lies on the fact that, due to the smoothness of the map, deformable models guided by CVF do not need, in general to be re sampled during evolution. On the other side, since GVF does not take into account the geometry of shapes, the snake sampling must be refined at points where two opposite directions compete (that is when entering into concave regions) in order to guarantee convergence to a closed contour. This increases the computational time of GVF up to four times CVF time in the case of the hand or the horse. Also in terms of the stiffness parameters, α

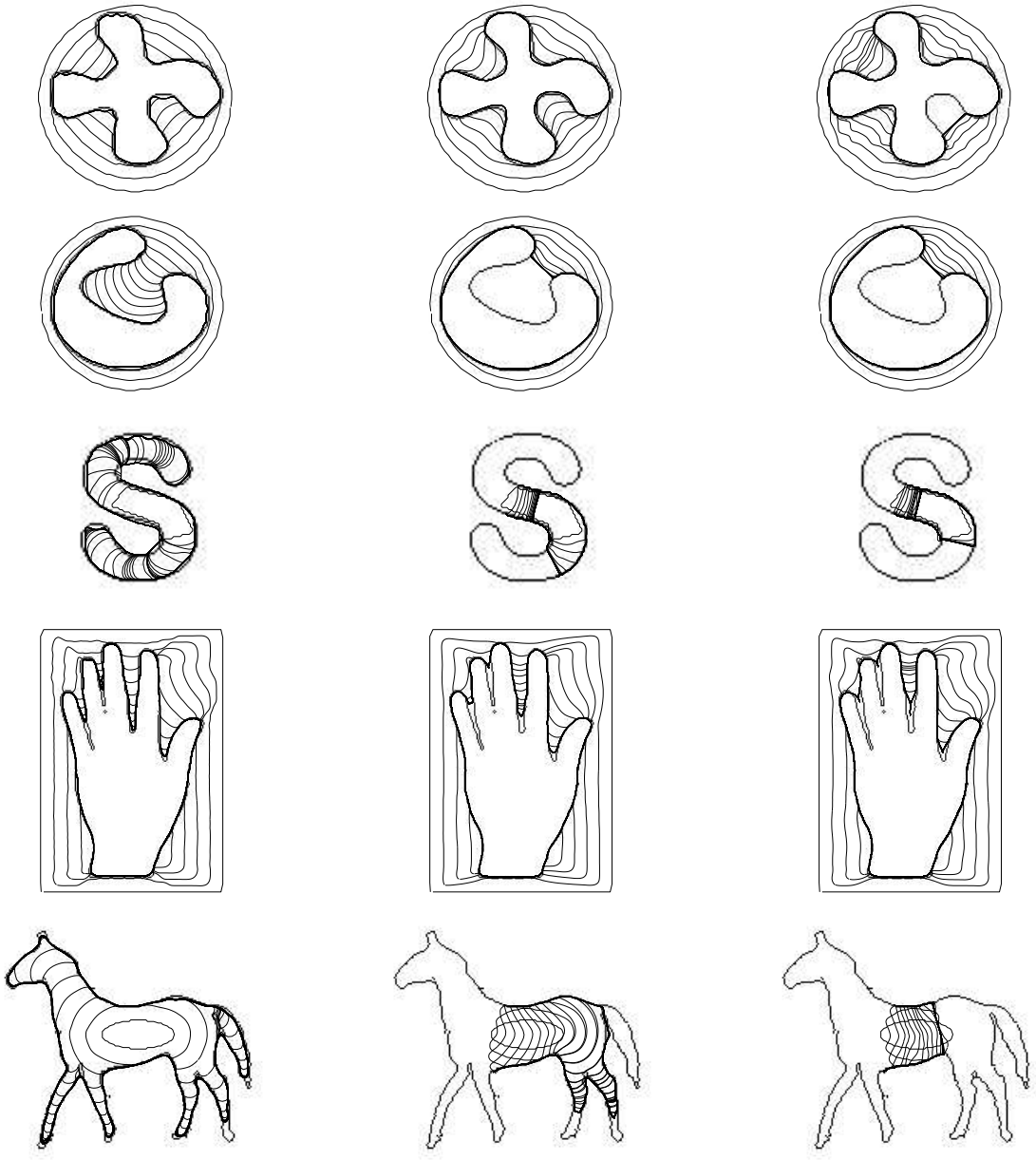

(a) (b) (c)

Figure 5.29: Snake convergence, CVF (a), GVF (b) and regularized DM (c).

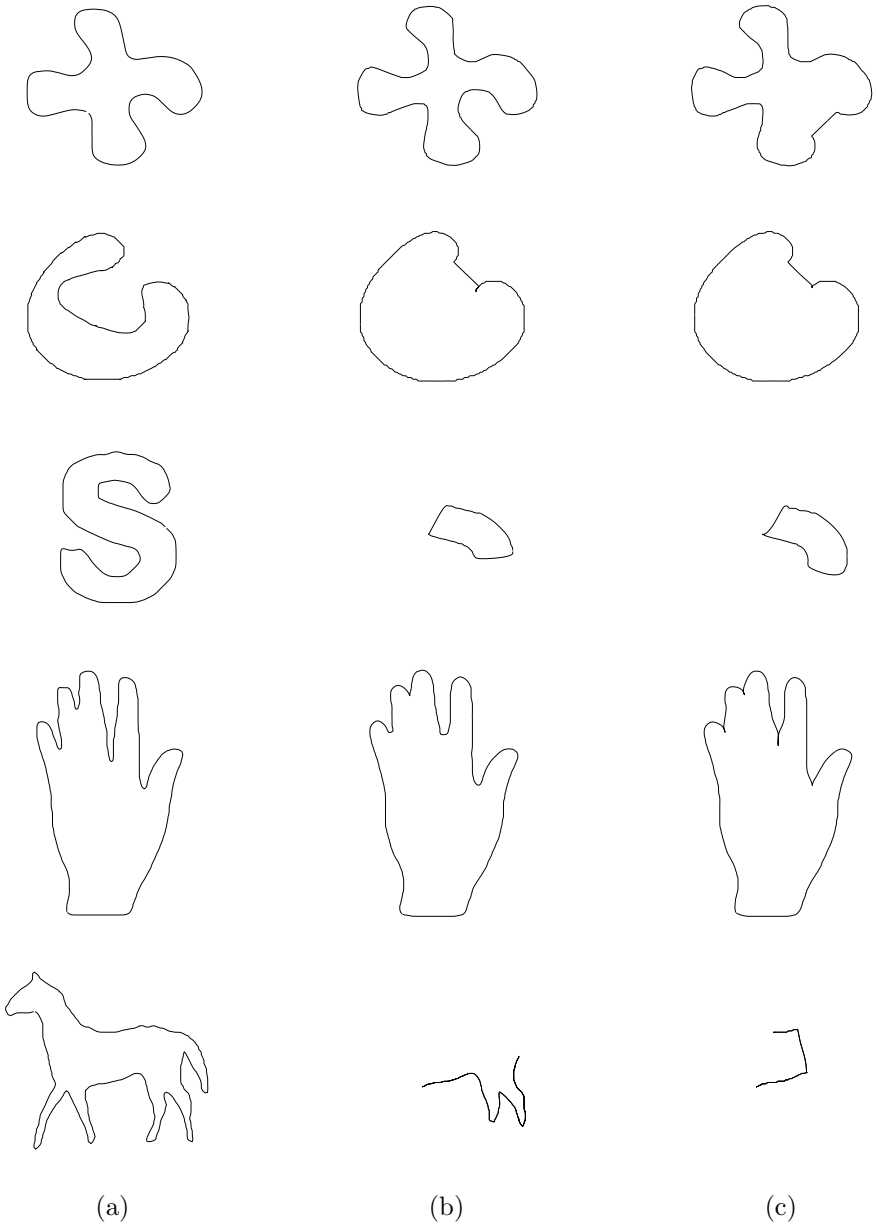

Figure 5.30: Shapes obtained with CVF (a), GVF (b) and regularized DM (c).

and β, CVF is the most efficient. Our tests done for different values of the stiffness parameters show that CVF supports, in general, values in the whole range of $[0, 1]$. Only in extreme cases like inner convergence to the horse and outer convergence to

the hand, α and β must be smaller than 0.3 if we want a reliable final model.

Another issue worth to be considered is the asymptotic behavior of the snake convergence. Figure 5.28 shows the evolution of the snake energy in time for convergence to the clover and the highly non-convex shape of fig. 5.29, in the case of a CVF guided snake (fig. 5.28(a),(b)) and a DM/GVF one (fig. 5.28(c),(d)). Notice that deformations under CVF present a smoother asymptotic behavior, compared to the highly oscillating graphics of DM and GVF. This oscillating behavior strengths when the snake gets trapped at saddle points. A smooth energy implies a strong advantage since a stop criterion in terms of the snake total energy is a robust way of determining the final state for CVF guided snakes.

5.3.2 Application to Object Segmentation

Smooth shape representation plays an important role in image segmentation. Connecting a set of points that lie on the object of interest, whatever its geometry, is still an open question. Parametric snakes [38] and geodesic snakes [11], [12] are the two techniques most commonly used by the image processing community. On one hand, in spite of yielding smooth models, poor convergence to concave shapes limits classic snakes applicability. On the other hand, geodesic snakes convergence to multiple objects, does not compensate for their slow convergence to piece wise linear curves that may have penetrated into large gaps of contours. We argue that the framework of classic snakes provides with an efficient way of shape modelling, both in terms of computational time and compact representation of a reliable model of the shape. The segmenting strategy we propose is the following.

We base image object segmentation on the approximation of a set of (possibly unconnected) points that conform to given characteristics exclusive to the contour of the object we want to model. We consider that the object is successfully segmented once we have a closed contour approaching this set of points. We propose the following strategy to model uncompleted contours. First, we will apply functional extension using ACC to the selected set of points in order to produce a closed contour. Ridges of the final extension are the curve of level zero of the Curvature Distance Map (CDM) that serves to compute the Curvature Vector Flow that will guide a parametric B-spline snake to a model of this contour.

We devote the last experiment to efficiency and accuracy of the former segmenting strategy compared to geodesic snakes. The set of images are the noisy images of fig.5.20 and the real images of fig.5.21 (a)-(c) in Section 5.2. Completions of the extracted contours (see fig.5.22) given by ACC (see fig.5.31) are the input zero level set for the computation of CVF. For geodesic snakes, we have used their original formulation [12] for image edge-based segmentation:

$$\gamma_t = (g(|\nabla I|)(c + \kappa) - \langle \nabla g(|\nabla I|), \overrightarrow{n} \rangle) \overrightarrow{n}$$

where $g(|\nabla I|) = 1/(1 + |\nabla I_\sigma|^2)$ and c is the area constrain constant. The function g has been computed over original images (fig.5.21 (a), (c)) in the case of the brain and the hand, and the filtered image of fig.5.20(b) for the noisy non convex shape. For a better comparison to our strategy and to reduce noise impact, the edge measure g

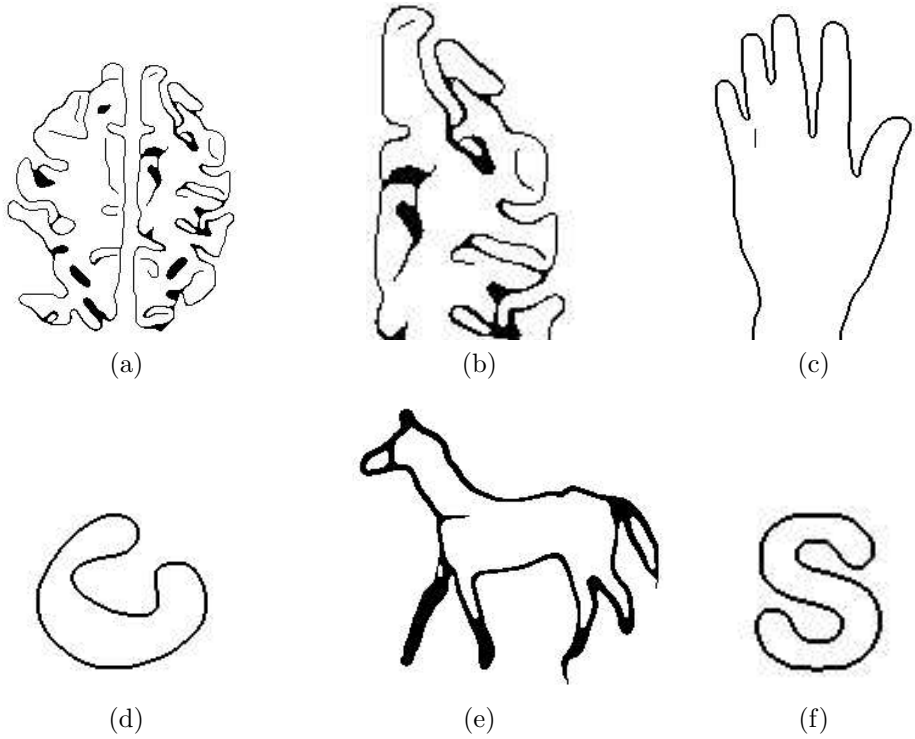

Figure 5.31: Reconstructed contours using DCV.

is computed over the image contours of 5.22 in the case of the character 's' and the horse.

Both in the case of geodesic and parametric snakes, we consider the snake has reached its final state when its total energy stabilizes. Snake convergence is illustrated in fig.5.32 and fig.5.33 (with yellow curves representing final geodesic snake segmentation). Segmentation using geodesic snakes strongly depends on the quality of image edges which makes their convergence to concave regions significantly decrease in the presence of noise (fig.5.32(b)) or highly non convex uncompleted contours. In noisy images, the regularization scale used to compute $|\nabla u_\sigma|$ must be increased to ensure a stable snake evolution. In the case of large gaps, the regularization scale must ensure that the gradient of g will close them, otherwise the snake could converge to an unconnected curve. However, the bigger the gaussian kernel is, the more prone to develop saddle points and ridges the image gradient is. Just to mention it, this phenomena still produces even if a regularization with GVF [**?**] is used. Since the constant c must keep within the range of $|\nabla g|$ if we want the snake to stop at image contours, we have that the area constraint term does not compensate ∇g bad behavior. Only in the case of noise free, non textured backgrounds (fig.5.33(d), (f)) geodesic snakes successfully adapt to contours.

On the other hand, segmentation using CVF only relies on the accuracy of the

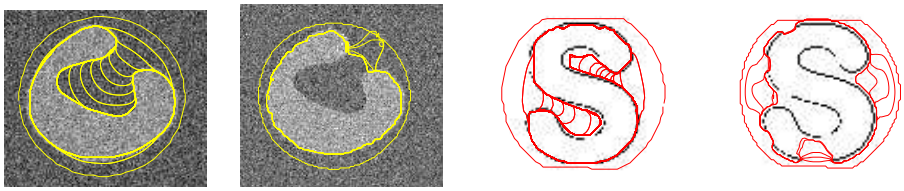

(a) (b) (c) (d)

Figure 5.32: Convergence to non convex shape using CVF snakes (a) and geodesic snakes (b). Convergence to character 'S' using CVF snakes (c) and geodesic snakes (d).

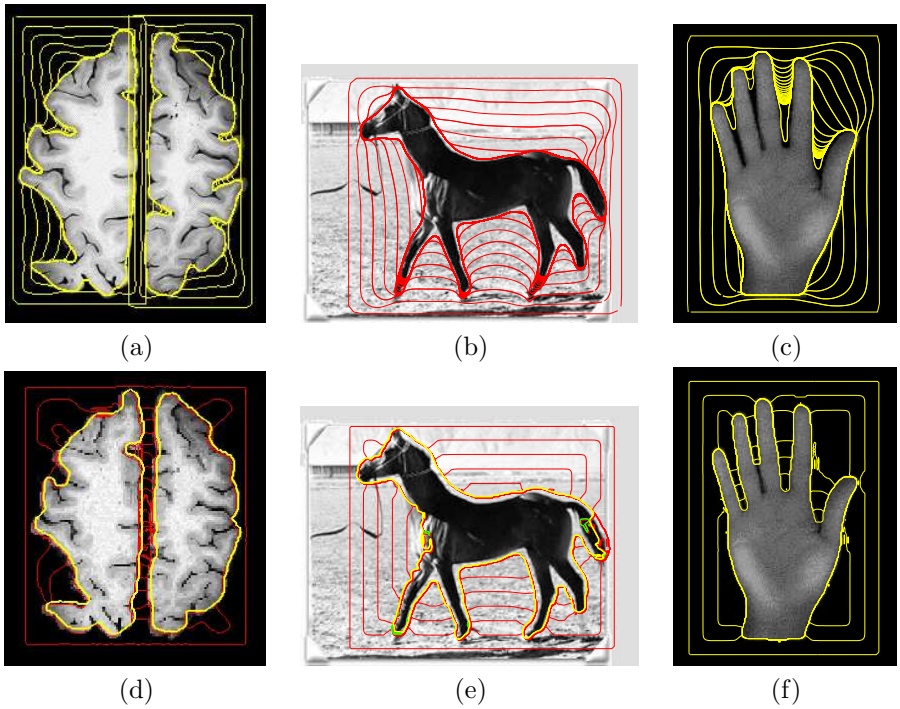

(a) (b) (c)

(d) (e) (f)

Figure 5.33: Snake Convergence to brain, horse and hand of CVF snakes (first row) and geodesic snakes (second row).

closed models yield by DVF, as CVF guarantees snake convergence to the zero level curve. Since the impact of noise was suppressed from the uncompleted contours of fig.5.22(d), (f), performance of our CVF parametric snake in noisy images (fig.5.32(a), (c)) clearly surpasses that of geodesic snakes. Also in the case of the horse, we obtain a more accurate representation, since the curve that geodesic snakes yield (fig.5.33(e)) has several connected components. Concerning unpolluted backgrounds (fig.5.33(a),

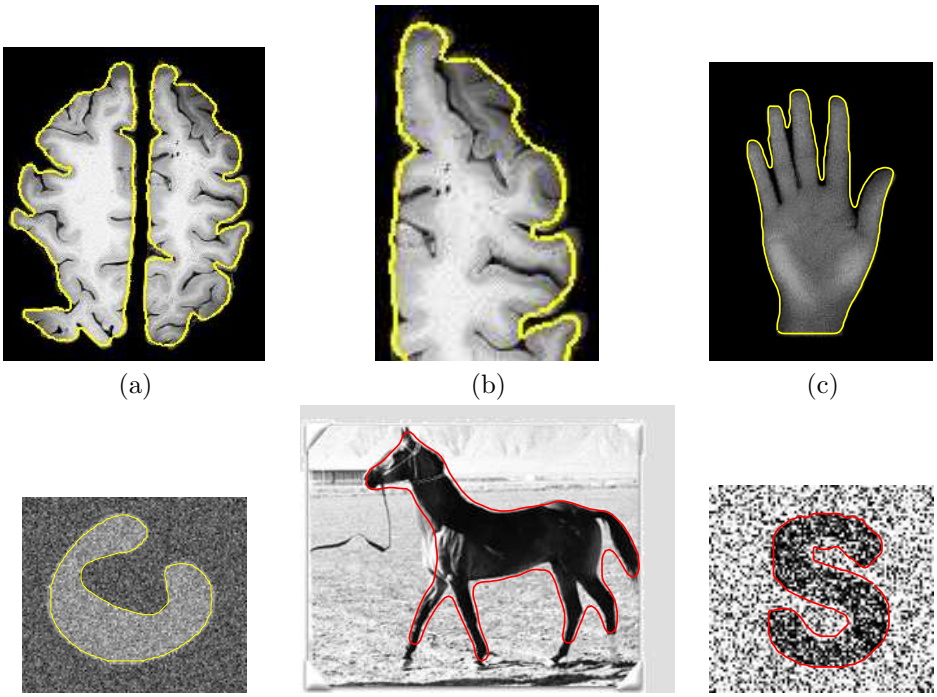

Figure 5.34: Segmentation using DVF/CVF.

(c)), the model of the brain (fig.5.34(a)) yielded by CVF is more precise than segmentation using geodesic snakes (fig.5.33(d)). Thanks to the accuracy of the brain closure (fig.5.24(a), (b)), the CVF contour captures more creases (fig.5.34(b)) than the geodesic model. Only in the case of sharp concave corners (hand of fig.5.33(d)) geodesic snakes perform better than CVF snakes. However, convergence to the hand (fig.5.33(c)) still compares to results obtain by geodesic snakes. Besides, final segmentations using CVF (fig.5.34), are, in all cases, smooth close models that conform to the original objects and keep their essential geometry. In order to increase accuracy, the final state achieved with CVF can be used as initial snake for a classic parametric snake.

Conclusions and Future Research

This work has shown that a geometric approach to PDE's enables designing image operators satisfying automatic stabilization at meaningful states smoothly approximating original objects. In particular, we have focused on shape modelling with segmenting purposes and a novel filtering technique(RCF), a contour closing algorithm (ACC) and an external snake potential (CVF) have been introduced.

The regularized curvature flow adds a measure of shape regularity to the mean curvature flow that prevents its degeneracy to a round point. Because the measure of regularity decreases over RCF orbits, the flow converges to a smooth model of the original shape. The image filtering defined by RCF level sets implicit formulation performs better than current filtering techniques as it achieves the best compromise between image quality and stabilization of the iterative numeric scheme.

Based on the grounds that a distance map represents the evolution of an initial curve in time under a geometric flow, CVF tracks evolution by mean curvature flow to avoid shocks. The gradient of this map is a smooth external force that guides in a natural manner the snake to the shape of interest. The fact that the force field takes into account the geometry of the final curve, makes convergence robust whatever the concavity of this curve is. Smoothness of snake evolution under CVF guarantees a robust convergence to smooth compact models of closed objects by means of a B-spline parametric snake.

Because the only requirement for computation of CVF is having closed contours, a novel approach to contour closing has been introduced. We have developed an implicit level sets formulation of a heat-like equation on manifolds in terms of a restricted diffusion operator. Such operators are an ideal tool for completion of contours regarded as a particular case of functional extension. Because ACC restricts diffusion to some curves of the image domain, the algorithm converges to closed models of shapes, as far as it a vector field representing the tangent of the contours to be closed. We propose a fat way of computing vector extensions (Coherence Vector Fields) conforming with tangents of unconnected contours at gap boundaries by applying Structure Tensor over either the contours masks or distance maps.

Finally, we have shown that a combination of ACC and CVF yields a segmenting strategy that compares and even surpasses performance of balloon-like geodesic snakes.

The theoretical setting developed suggests the following further research issues:

Future Lines of Research

1. **Applying restricted diffusion to a corner-preserving image filtering**

   By its own definition, a coherent vector field computed on the image yields smooth completions of the image significant curves, such as edges or ridges, that preserve curvature maxima. It follows that the associated restricted diffusion would uniformize their gray level while preserving their corners and smoothing noisy areas.

2. **Spline approximation of shapes with a given error**

   An efficient multiresolution approximation of curves with splines is still an open question. The first step is determine the minimum number of control points needed to obtain an approximate model of a curve with a given error. The CVF external force is the ideal starting point as it ensures snake convergence to closed shapes.

3. **Topological equivalence of analytic convexity conditions**

   The natural further research of the geometric equivalent of functional convexity is to give topological criteria in terms of the number of connected components (Morse theory [51]) of the functional level sets. Such simple criterion is the natural way of detecting inflexion points in GVF-like flows and provides a way of redefining the vector fields to ensure snake convergence for image segmentation.

4. **First order approximation of non-linear operators**

   Poor efficiency of numeric iterative processes mars performance of non-linear diffusion and hinders their design. Successive convolution with the kernel associated to their linear approximation would yield a first order fast accurate approach in the case of convergent operators.

5. **Apply all techniques (the developed and the forthcoming) to every single image available to find out their true applicability to the real world**

   An exhaustive validation of the techniques developed is a compulsory step for their reliable application to real problems.

Bibliography

[1] L.Alvarez, F.Guichart, P.L.Lions,J.M.Morel, *Axioms and Fundamental Equations of Image Processing.* Arch.Ration. Mech. and Anal.,123,199-257, 1993.

[2] G. Aubert, M. Barlaud,L. Blanc-Feraud, P. Chatbonnier. Deterministic edge-preserving regularization in computer imaging. *IEE Trans. Imag. Process.*, vol 6(2), Feb. 1997.

[3] Idan Bar-Sade and Avi Itzhaki. *Image Contour Extraction.* Tech. Report. TECHNION - The Vision Research and Image Science Laboratory.

[4] C.Ballester, M.Bertalmo, V.Caselles, G.Sapiro and J.Verdera. *Filling-In by Joint Interpolation of Vector Fields and Gray Levels* IEEE Trans. Image Processing, August 2001.

[5] J.Bigun, G.Granlund, J.Wiklund. *Multidiemnsional orientation estimation with applications to texture analyis and optical flow.* PAMI, vol. 13, 1991.

[6] J.Canny. *A Computational Approach to Edge Detection*, PAMI, vol. 8, 1986.

[7] F.Catté, P-L.Lions, J.-M.Morel, T.Coll. *Image selective smoothing and edge detection by nonlinear image diffusion*, SIAM J. Num. Ana., vvol. 29, 182-193, 1992.

[8] C.Cañero, P.Radeva. *Vesselness Enhancement Diffusion*, Patt. Recog. Letters 24 (2003), 3141-3151.

[9] R. Carmona, S. Zhong. *Adaptative Smoothing respecting Feature Directions* , IEEE Trans. Image Proc., vol. 7(3), March 1998.

[10] V.Caselles, F.Catté, T. Coll, F. Dibos, *A geometric model for active contours.* Numerische Mathematik, 66, pg.1-31, 1993.

[11] V. Caselles, B. Coll, J. Morel. *Topographic Maps and Local Contrast changes in Natural Images*, Int. J. Comp. Vision, vol 33, 1999.

[12] V.Caselles, R.Kimmel, G. Sapiro *Geodesic Active Contours.* Int. J. Comp. Vision.

[13] T. Chan, J. Shen. *Non-texture inpaitings by Curvature Driven Diffusions.* J. Visual Communication and Image Representation, 12(4), pp. 436-449, 2001.

[14] T. Chan, SH. Kang, and J. Shen. *Euler's elastica and curvature based inpaintings*, SIAM J. Appl. Math., 63(2), 2002.

[15] Y.G. Chen, Y. Giga, S. Goto, *Uniqueness and existence of viscosity solutions of generalized mean curvature flow equations*. J. Differential Geometry 33, pg. 749-786, 1991.

[16] L. D. Cohen. *On active contour models and ballons*. CVGIP:Image understanding, 53(2):211-218, 1991.

[17] L.D. Cohen, R. Kimmel, *Global minimum for active contour models: A minimal path approach*. Int. Journal Comp. Vision, 24 (1), pp. 57-78, Aug. 1997.

[18] S.D. Conte, C. de Coor. *Elementary numerical analysis, an algorithmic approach*. McGraw-Hill, NY, 1972.

[19] M.G. Crandall, H. Ishii, P.L. Lions *User's guide to viscosity solutions of second order partial differential equations*. Bulletin of the American Math. Society, 27, pg. 1-67, 1992.

[20] M.G. Crandall, H. Ishii, P.L. Lions *User's guide to viscosity solutions of second order partial differential equations*. Bulletin of the American Math. society, 27, pg. 1-67, 1992.

[21] E.B. Davies. *Heat Kernels and Spectral Theory*. Cambridge Tracts. in Math. 92, Cambridge University Press, 1989.

[22] Yu.V.Egorov, M.A.Shubin. *Partial Differential Equations I*. Enciclopaedia of Math. Sciences, vol.30, Springer-Verlag.

[23] L.C. Evans. *Partial Differential Equations*. Berkeley Math. Lect. Notes, vol.3B, 1993.

[24] D.Gil, P.Radeva. *Regularized Curvature Flow*. Computer Vision Center Tech. Report n 63, 2002.

[25] D.Gil, P.Radeva, F. Mauri. *IVUS Segmenation via a Regularized Curvature Flow*. Proceedings of CASEIB'02.

[26] D.Gil, P.Radeva, F.Vilario. *Anisotropic Contour Completion*, ICIP'03.

[27] D.Gil, P.Radeva. *Curvature Vector Flow to Assure Convergent Deformable Models*. EMMCVP'03.

[28] R.C.Gonzalez, P.Wintz. *Digital Image Processing*, Addison Wesley, Reading, MA.

[29] C.L.Epstein, M.Gage, *The Curve Shortening Flow in Wave Motion: Theory, Modeling and Computation*, A.Chorin and A.Majda, eds., springer-Verlag, New York, 1987.

[30] William H. Press, Brian P. Flannery, Saul A. Teukolsky, William T. Vetterling. *Numerical Recipes in C : The Art of Scientific Computing*. Cambridge University Press, 1993.

[31] D.R. Forsey, R.H. Bartels. *Surface Fitting with Hierarchical Splines*, Computer Graphics, April 1995.

[32] M.A.Grayson. *The heat equation shrinks embedded plane curves to round points*. J. Differential Geometry, Vol. 26, pp. 285-314, 1986.

[33] M.Gage, R.S.Hamilton. *The heat equation shrinking convex plane curves*. J. Differential Geometry, Vol. 23, pp. 69-96, 1986.

[34] M. Gage. *Curve shortening makes convex curves circular*. Invent. Math, vol 76, pp. 357-364, 1984.

[35] H. Hoppe, T. DeRose, T. Duchamp, M. Halstead, H. Jin, J. McDonald, J. Scheweitzer, and W. Stuetzle, *Piecewise smooth surface reconstruction*, Proc. ACM SIGGRAPH, pp. 295-302, July 1994.

[36] B. Jähne, *Spatio-temporal image processing*. Lecture Notes in Comp. Science, vol. 751, Springer, Berlin, 1993.

[37] G. Kanizsa, *Organization in Vision: Essays in Gestalt Continuation*. New York: Praeger, 1979.

[38] M.Kass, A.Witkin and D.Terzopoulos, *Snakes: Active Contour Models*, Int. Journal of Computer Vision, vol. 1, pp. 321-331, 1987.

[39] B. Kimia, K. Siddiqi, *Geometric Heat Equation and non linear Diffusion of Shapes and Images*. IEEE Proc. of Comp. Vision and Pattern Recognition, June 1994.

[40] B.Kimmia, A.Tanenbaum, S.W. Zucker. *On the Evolution of Curves via a Function of Curvature I:the Classical Case*. J. Math. Analysis and Aplications, vol 163, pp 438-458, 1992.

[41] B. Kimia, A. Tanenbaum, S.W. Zucker. *Toward a computational theory of shape: an overwiew*, Lecture Notes in Comp. Sci., vol 427, pp 402-407, Springer-Verlag, New York-Berlin.

[42] Ch. Knoll, M. Alcaiz, V. Grau, C. Montserrat, M.C. Juan, *Outlining of the prostate using snakes with shapes restrictions based on the wavelet transform*. Pattern Recognition, 32, pp. 1767-1781, 1999.

[43] P. Kornprobst, R. Deriche G. Aubert, *Nonlinear Operators in Image Restoration*, C.V.P.R, Porto Rico, june 1997.

[44] S.Lang *Linear Algebra*. Addison Wesley.

[45] Antonio M. López, David Lloret, Joan Serrat and JuanJ. Villanueva. *Multilocal Creaseness Based on the Level-Set Extrinsic Curvature* Comp. Vision Ima. Understanding vol. 77, pp. 111-144, 2000.

[46] Lysaker, Osher, Thai. *Noise Removal Using Smoothed Normals and surface Fitting*. UCLA, Applied Math. CAM-report-03-03.

[47] T. McInerney and D. Terzopoulos. *Deformable models in medical images analysis: a survey*. Medical Image Analysis, 1(2):91-108, 1996.

[48] R.Malladi, J.A.Sethian and B.C.Vemuri. *Shape Modeling with Front Propagation:A Level Set Approach PAMI*, vol. 17 (2), pp. 158-175, Feb.1995

[49] R.Malladi, J.A.Sethian. *Image Processing: Flows under min-max curvature and mean curvature*. Graphical Models and Image Processing, vol. 58 (2), pp. 127-141, Mar. 1996.

[50] S. Masnou, J.M. Morel, *Level Lines Based Discclusion*, Proc. IEEE Int. Conf. on Image Processing, Chicago IL, pp. 259-263, 1998.

[51] J.Milnor, *Morse Theory*, Annals of Math. Studies n 51, Princetown Univ. Press.

[52] P. Monasse, F. Guichard. *Fast computation of contrast invariant image representation*, IEEE Trans. Image Proc., vol. 9, 2000.

[53] J. Monteil, Azeddine Beghdadi, *A new interpretation an improvement of the Nonlinear anisotropic Diffusion for Image Enhancement*. IEEE Trans. IP, vol 21, n 9, Sep. 1999.

[54] D. Mumford, *Algebraic Geometry and its Applications*, Springer-Verlag, New York, 1994.

[55] M. Nitzberg, D. Mumford, T. Shiota, *Filtering, Segmentation and Depth*. Springer-Verlag, Berlin, 1993.

[56] M.Nitzberg, T.Shiota, *Non-linear image filtering with edge and corner enhancement*, IEE Trans. Imag. Process, vol. 14, pp. 826-833, Aug. 1992.

[57] S.J.Osher, J.A.Sethian *Front propagation with curvature dependent speed: Algorithms based on Hamilton-Jacobi formulations*. Journal of Computational Physics 79, pg. 12-49, 1988.

[58] N. Paragios, R. Deriche. *Geodesic Active Contours for Supervised Texture Segmentation*. Proc. of Computer Vision and Pattern Recognition 2,422-427, 1999.

[59] N.Paragios, O.Mellina-Gottardo and V.Ramesh. *Gradient Vector Flow Fast Geodesic Active Contours*, IEEE Int. Con. Comp. Vision, vol I, Jul. 01, Vancouver, Canada.

[60] P. Perona, J. Malik, *Scale space and edge detection using anisotropic diffusion*, Proc. IEEE Comp. Soc. Workshop on Comp. Vision, IEEE Computer Society Press, pp. 16-22, 1987.

[61] W. Rudin. *Complex and Real Analysis*. McGraw-Hill, Inc.

[62] L.Rudin, S.Osher, E.Fatemi. *Nonlinear total variation based noise removal algorithms*, Physica D. vol. 60, 1992.

[63] *Geometric Partial Differential Equations and image analysis* Cambridge University Press, Cambridge, U.K.,2001.

[64] G. Sapiro, B.B. Kimia, R. Kimmel, D. Shaked, A. Bruckstein. *Implementing continuous-scale morphology*. Pattern Recognition, vol. 26(9), 1992.

[65] J.A. Sethian, *Level Set Methods: Evolving Interfaces in Geometry, Fluid Mechanics, Computer Vision and Material Sciences*. Cambridge Universirty Press, Cambridge, U.K,1996

[66] K. Siddiqi, A. Tannenbaum, S.W. Zucker. *A Hanmiltonian Aaproach to the Eikonal Equation*, EMMCVPR'99, Lecture Notes in comp. Science, 1654.

[67] M. Spivak. *A Comprehensive Introduction to Differential Geometry*. Houston: Publish or Perish, cop. 1979.

[68] Ch.Sun, S. Pallotino, *Circular shortest path on regular grids*, Asian Conference on Computer Vision, pp. 852-857, Melbourne, Australia, Jan. 2002.

[69] Z.S.G. Tari, J. Shah, H. Pien. *Extraction of shape skeletons from grayscale images*. Comp. Vision and Image Understanding, vol. 66, pp. 133-146, May 1997.

[70] J.F. Traub. *Iterative methods for the solution of equations*, Prentice-Hall, Englewoods Cliffs,NJ, 1964.

[71] A.Tveito, R.Winther. *Introduction to Partial Differential Equations*, Texts in Appl. Math.

[72] J.Weickert, *Anisotropic Diffusion in image Processing*, PhD Thesis, Jan. 1996.

[73] J.Weickert, B.M. ter Haar Romeny, M.A. Viergever, *Efficient and reliable schemes for nonlinear diffusion filtering*, IEEE Trans. Im. Proc., 1998.

[74] J. Weickert, *A Review of Nonlinear Diffusion Filtering*. B. Haar Romery, l. Florack, J. Koenderink, M. Viergever (Eds.), Scale-Space Theory in Computer Vision, Lecture Notes in Computer Science, vol. 1252, Springer-Verlag, Berlin, pp. 3-28, 1997.

[75] C.Xu and J.L. Prince *Snakes, shapes and gradient vector flow*. IEEE Trans. on Image Proc., vol. 7(3), pp. 359-369, March 1998.

[76] C.Xu and J.L. Prince *Gradient Vector Flow Deformable Models*. Handbook of Medical Imaging, Isaac Bankman, Academic Press, September 2000.

[77] C.Xu and J.L. Prince *Generalized gradient vector flow external forces for active contours*. Signal Process., An Int. Journal, 71(2), pp. 132-139, 1998.

[78] C. Xu, A. Yezzi, and J. Prince, *On the Relationship between Parametric and Geometric Active Contours*. Proc. of 34th Asilomar Conference on Signals, Systems and Computers, pp. 483-489, October, 2000.

[79] G. Unal, H. Krim, A. Yezzi. *Stochastic Differential Equations and Geometric Flows*, IEEE Trans. Image Proc., vol. 11 (12), Dec. 2002.

[80] Y.-L.You, M.Ka veh, *Formation of step images during anisotropic diffusion*,Proc. ICIP '97.

[81] Y.-L.You, W.Xu, A.Tannenbaum, M.Ka veh, *Behavioral analysis of anisotropic diffusion in image processing*, IEEE Trans. Im. Proc., Nov. 1996.

[82] D. Zhang, M. Herbert, *Harmonic shape images: a representation for 3-d free-form surfaces based on energy minimization*, EMMCVPR'99, Lect. Notes in Comp. Science, 1654.

Publications

2004

- Debora Gil, Petia Radeva, "Extending Anisotropic Operators to Recover Smooth Shapes", under second revision in Computer Vision and Image Understanding.
- Debora Gil, Petia Radeva, "Inhibition of False LandMarks", submitted to ICPR'04.
- Debora Gil, Petia Radeva, "A Regularized curvature flow designed for a Selective Shape Restoration', to be published in IEEE Trans. Image Processing.

2003

- Debora Gil, Petia Radeva, "Shape Restoration via a Regularized Curvature Flow", to be published in Journal of Mathematical Imaging and Vision.
- Oriol Pujol, Debora Gil, JJ. Villanueva, Petia Radeva, "Fundamentals of Stop and Go Active Models", submitted to Imaging and Computing Vision in August 03.
- O.Rodriguez Leor, J. Mauri, E. Fernandez-Nofrerias, C. Garcia Garcia, R. Villuendas, V. Valle Tudela, D. Gil, P. Radeva, 'Reconstruction of a spatio-temporal model of the intima layer from intravascular ultrasound sequences', European Heart Journal, ESC Congress 2003, Vienna, Austria, 2003.
- Debora Gil, Petia Radeva, "Curvature vector flow to assure convergent deformable models", EMMCVPR '03, Lect. Notes in Comp. Science, vol. 2683.
- Debora Gil, Petia Radeva, Fernando Vilario, "Anisotropic Contour Completion", ICIP'03 Proceedings.
- Debora Gil, "Curvature based Distance Maps", CVC Tech. Report, n 70. Computer Science Dep., April 03.

2002

- Debora Gil, Petia Radeva, "IVUS segmentation via a regularized curvature flow". CASEIB'02 Proceedings.

- Debora Gil, Petia Radeva, Oriol Rodriguez et al. "Reconstruccin de un modelo espacio-temporal de la luz del vaso a partir de secuencias de ecografia intracoronaria.", Revista de la Sociedad Espaola de Cardiologa, vol 55 (supl2), pag 12.

- Debora Gil, "Regularized Curvature Flow". CVC Tech. Report, n 63. Computer Science Dep., Nov. 02.

- Debora Gil, Petia Radeva, Fina Mauri et al. : "Ecografia intracoronria: segmentaci automtica de l'rea de la llum", revista de la Societat Catalana de Cardiologia, Vol 4, n 4, March 02

2000

- Debora Gil, Petia Radeva, Jordi Saludes, "Segmentation of artery wall in coronary IVUS images: a probabilistic approach". IEEE Proceedings of Computers in Cardiology, 00.

- Debora Gil, Petia Radeva, Jordi Saludes, "Segmentation of artery wall in coronary IVUS images: a probabilistic approach". IEEE Proceedings of ICPR' 00.

- Debora Gil, Petia Radeva, Fina Mauri et al, "Moviment del vas en l'analisi d'imatges de ecografia intracoronria: un model matemtic", revista de la Societat Catalana de Cardiologia, Vol 3, n8, June 00.

- Fina Mauri, E.F. Nofreras, J.Comin, B.Garcia, E.Irculis, J.A.Gmez, P.Valdovinos, F.Jara, A.Cequier, E.Esplugas, O.Pujol, C.Caero, Debora Gil, P.Radeva, R.Toledo, JJ.Villanueva, "Avaluaci del Conjunt Stent/Artria mitjanant ecografia intracoronria: l'entorn informtic ", revista de la Societat Catalana de Cardiologia, Vol 3, n8, June 00.

- Debora Gil, "Complex Nilmanifolds without non-constant holomorphic functions". Prepublications of the Univ. Autnoma de Barcelona, vol. 03/2000. Mathematics Dep, Febr. 2000.

- Debora Gil, "Complex Nilmanifolds without non-constant holomorphic functions". Prepublicacions of the European Net TMR (ERB FMRX-CT96 0040). Febr. 00.